FACULTY OF ENGINEERING AND ARCHITECTURE

InP-on-Si DFB Laser Diodes with High Wall-Plug Efficiency, Large Modulation Bandwidth and Low Noise

Javad Rahimi Vaskasi

Doctoral dissertation submitted to obtain the academic degree of
Doctor of Photonics Engineering

Supervisors
Prof. Geert Morthier, PhD - Prof. Günther Roelkens, PhD
Department of Information Technology
Faculty of Engineering and Architecture, Ghent University

December 2022

GHENT UNIVERSITY

ISBN 978-94-6355-664-4
NUR 950
Wettelijk depot: D/2022/10.500/105

Members of the Examination Board

Chair

Prof. Em. Daniël De Zutter, PhD, Ghent University

Other members entitled to vote

Andreas De Groote, PhD, Brolis Sensor Technology
Prof. Martijn Heck, PhD, Technische Universiteit Eindhoven, the Netherlands
Prof. Bart Kuyken, PhD, Ghent University
Prof. Dries Van Thourhout, PhD, Ghent University

Supervisors

Prof. Geert Morthier, PhD, Ghent University
Prof. Günther Roelkens, PhD, Ghent University

Acknowledgements

It is a great pleasure for me to express my gratitude to the many people who have helped me or have been an important part of my life during my PhD study.
First, I would like to express my special appreciation and thanks to my first promoter Prof. Geert Morthier for giving me the opportunity to start my PhD. I would like to thank you for your guidance and support during my PhD study. Moreover, I would like to thank my second promoter Prof. Gunther Roelkens, you have been a tremendous mentor for me and your advices on my research have been invaluable. I would also like to thank my committee members for spending time to read my thesis and providing valuable comments to improve the manuscript. I would appreciate the technical cleanroom support provided by Steven, Muneeb, and Liesbet. In addition, a special thanks to the colleagues at IDLab design group led by Prof. Johan Bauwelinck for the collaboration in the high speed characterization of the fabricated lasers.
I spent more than four years in PRG and had the opportunity to work with tremendous colleagues. I consider myself to be very fortunate to be able to work with you all for the last four years and I want to thank everyone for making it memorable and something that I will cherish for the years to come.
If it was not for the help and support of my great friends during these years, it would have been intolerable ending the graduate school. Thank you all for making it an enjoyable experience to live in Belgium. I am so happy that I had the privilege to meet talented individuals like you which I could make many life-time friends.
Finally, I especially would like to express my deepest gratitude and love for my family. I would like to dedicate this work to my wonderful deeply missed mother, who learned me the true meaning of sacrifice and kindness.

Ghent, November 2022
Javad Rahimi

Contents

Acknowledgements **i**

Contents **iii**

Samenvatting **ix**

English summary **xvii**

1 DFB lasers with symmetric output waveguides xx

2 DFB lasers with a single output waveguide xxi

3 Conclusion xxiii

1 Introduction **1-1**

1.1 Optical Communication Links 1-2

1.2 Silicon Photonics 1-3

1.3 III-V/Si Integration Techniques 1-5

1.3.1 Hybrid integration 1-5

1.3.1.1 Photonic wire bonding 1-5

1.3.1.2 Butt-coupling 1-7

1.3.1.3 Flip-chip bonding 1-8

1.3.2 Heterogeneous integration 1-9

1.3.2.1 Die or wafer bonding 1-9

1.3.2.2 Micro-transfer-printing 1-10

1.3.3 Direct epitaxial growth 1-13

1.3.4 Regrowth on a bonded template 1-14
1.4 State-of-the-art heterogeneously integrated InP-on-Si single mode lasers 1-15
1.4.1 Distributed Feedback lasers 1-16
1.4.2 Distributed Bragg Reflector lasers 1-18
1.4.3 Widely tunable lasers 1-19
1.5 Research objectives 1-19
1.6 Outline of the thesis 1-20
1.7 Publications 1-22
1.7.1 Publications in international journals 1-22
1.7.2 Publications at international conferences 1-22

Bibliography **1-25**

2 Theory of distributed feedback laser diodes **2-1**
2.1 Introduction 2-2
2.2 Coupled mode theory 2-3
2.3 Rate equations model 2-10
2.3.1 Threshold analysis 2-11
2.3.2 Above threshold characteristics 2-11
2.3.3 Small signal characteristics 2-13
2.3.4 Large signal characteristics 2-15
2.3.5 Noise characteristics of laser diodes 2-17
2.3.5.1 Relative Intensity Noise 2-18
2.3.5.2 Laser linewidth 2-20
2.4 Wall-plug and differential efficiencies 2-22
2.5 Linewidth of laser diodes with distant reflections 2-23
2.6 Conclusion 2-26

Bibliography **2-29**

3 Design and fabrication of III-V-on-Si C-band distributed feedback laser diodes 3-1

3.1 Overview of earlier III-V-on-Si DFB lasers 3-2

3.1.1 Optical loss characterization 3-3

3.1.2 Carrier lifetime characterization 3-5

3.2 Optical design of a compact cavity 3-8

3.3 Integrated lasers realized by bonding 3-13

3.3.1 SOI Fabrication 3-13

3.3.1.1 Electron-beam lithography 3-13

3.3.1.2 Development and dry etching 3-15

3.3.2 Bonding Process 3-16

3.3.3 III-V Process flow 3-18

3.3.3.1 Substrate and sacrificial layers removal 3-18

3.3.3.2 Mesa definition 3-19

3.3.3.3 Mesa etching 3-21

3.3.3.4 Active region patterning 3-23

3.3.3.5 N-contact metallization 3-25

3.3.3.6 Island definition and passivation 3-26

3.3.3.7 P-contact metallization 3-26

3.3.3.8 Final metallization 3-28

3.4 Conclusion 3-29

Bibliography 3-31

4 Static and dynamic characterization of integrated distributed feedback lasers 4-1

4.1 Introduction 4-1

4.2 DFB lasers with symmetric output waveguide 4-2

4.2.1 III-V-on-Si DFB lasers with a narrow InGaAlAs MQW active region 4-3

4.2.2 III-V-on-Si DFB lasers with a wide InGaAsP MQW active region 4-6

4.2.2.1 Static characteristics 4-9

4.2.2.2 Dynamic characteristics 4-12

4.3 III-V-on-Si DFB lasers with a wide InGaAsP MQW active region and a single output waveguide 4-14

4.3.1 Static characteristics 4-16

4.3.2 Noise characteristics 4-20

4.3.3 Dynamic characteristics 4-22

4.4 Conclusion 4-23

5 Conclusions and outlook **5-1**

5.1 Conclusions 5-1

5.2 Outlook 5-3

5.2.1 Design and fabrication improvements 5-3

5.2.2 Reliability test 5-4

5.2.3 O-band epitaxial structure for high temperature performance 5-4

5.2.4 Small foot-print transfer printed DFB lasers 5-5

Nederlandse samenvatting

Dit doctoraatsproefschrift beschrijft het onderzoek dat gedaan werd op DFB laser diodes, bekomen door heterogene integratie van Indiumfosfide lagen op een silicium-op-isolator (SOI) passief optisch golfgeleidercircuit. Het doel was om compacte DFB lasers te fabriceren met hoge efficiëntie en lage lijnbreedte. De vermogenomzettingsefficiëntie drukt uit hoeveel optisch vermogen door een laser geleverd wordt per eenheid toegevoerd elektrisch vermogen. Een lage lijnbreedte, de spectrale breedte van de emissielijn, is belangrijk voor veel toepassingen zoals sensing, coherente communicatie, enz.. DFB laser diodes zijn laser diodes waarin de reflectie aan de spiegels vervangen is door verdeelde reflecties (Bragg reflecties) in een diffractierooster, en die daardoor gewoonlijk een emissiespectrum vertonen bestaande uit een enkele lijn. Het gebruik van verdeelde reflecties heeft geleid tot de naam distributed feedback laser of DFB laser.

In het proefschrft wordt begonnen met een inleiding waarin o.a. kort de stand van zaken besproken wordt van optische communicatie. Nadien wordt het belang van silicium fotonica uitgelegd, alsook waarom in silicium omwille van zijn bandenstructuur geen goede lichtbronnen te realiseren zijn. Dit laatste betekent dat lichtbronnen (laser diodes) voor siliciumfotonica noodzakelijk moeten geimplementeerd worden via hybriede of heterogene integratie van III-V material (GaN, GaAs, InP en hun ternaire en quaternaire legeringen). Een kort overzicht van de verschillende methodes voor hybriede en heterogene integratie wordt daarom ook in het inleidend hoofdstuk gegeven. Het inleidende hoofdstuk sluit af met een kort overzicht van de belangrijkste heterogeen geïntegreerde DFB en de gerelateerde DBR (distributed Bragg reflector) lasers die in het verleden gerealiseerd warden. DBR lasers worden vooral gebruikt wanneer golflengte-afstemming gewenst is. Een bovenaaanzicht van een DFB laser heterogeen geïntegreerd op een SOI golfgeleider wordt getoond in Figuur 1, samen met de dwarsdoorsnede op verschillende plaatsen.

Alvorens gedetailleerd in te gaan op het ontwerp en de fabricatie van de laserdiodes die het onderwerp uitmaken van dit doctoraat, wordt in het tweede hoofdstuk aandacht besteed aan de theorie van DFB laserdiodes. De gekoppelde-golftheorie, die de propagatie van de voorwaarts en achterwaarts propagerende golven beschrijft, alsmede hun koppeling via het Bragg rooster, komt eerst aan bod. Uitgaande hiervan worden de karakteristieken bepaald van de lasermodi, voor een DFB laser met uniform Bragg rooster en voor een DFB laser met een Bragg rooster met een fazesprong in het midden. Benaderingen voor de drempelwinst (winst vanaf dewelke

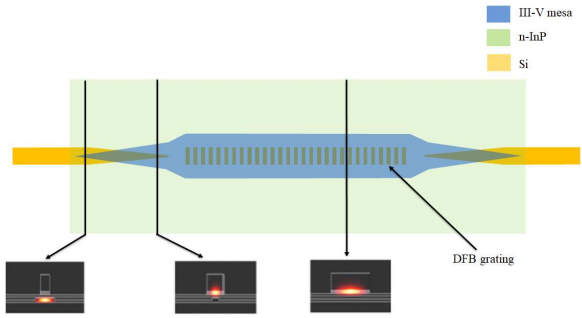

Figuur 1: Bovenaanzicht met verschillende dwarsdoorsnedes van een DFB laserdiode heterogeen geïntegreerd op een SOI golfgeleider.

laserwerking optreedt) worden afgeleid als functie van de koppelingscoëfficient κ, welke een maat is voor de sterkte van de Bragg reflecties. Een tweede deel van dit hoofdstuk is gewijd aan de beschrijving van laserdiodes met behulp van evolutievergelijkingen. Dergelijke vergelijkingen voor de gemiddelde ladingsdragersdichtheid in de actieve laag en voor het aantal fotonen per mode laten toe om zowel de dynamische eigenschappen (bv. modulatiebandbreedte) als de ruiskarakteristieken (bv. lijnbreedte) af te leiden. Op het einde van het tweede hoofdstuk wordt tenslotte nog dieper ingegaan op het effect van externe reflecties (buiten de eigenlijke laserdiode) op de lijnbreedte van de laserdiode. Een dergelijke reflectie van een paar procent treedt typisch op aan het diffractierooster dat gebruikt wordt om het licht van de siliciumgolfgeleider naar een glasvezel te koppelen. Er wordt getoond hoe zo'n externe reflectie de lijnbreedte zowel kan doen toenemen als doen afnemen, afhankelijk van de faze van die reflectie. Dit is van belang omdat de laserdiodes die in het vervolg van het doctoraat besproken worden steeds een dergelijke externe reflectie ondergaan en hiervan kan gebruik gemaakt worden om een heel kleine lijnbreedte te bekomen.
Het derde hoofdstuk beschrijft in meer detail het ontwerp en de fabricatie van de nieuwe generatie heterogeen geïntegreerde DFB lasers die in het kader van dit doctoraat bestudeerd werden. Teneinde een duidelijk idee te hebben in welke richting het ontwerp geoptimiseerd dient te worden, werden eerst enkele eigenschappen van de vorige generaties DFB lasers gemeten en/of uit metingen ge-extraheerd, bv. de interne verliezen, de koppelingsconstante van het Bragg rooster en de coëfficienten die de ladingsdragersrecombinatie bepalen. Metingen van de recombinatietijden voor verschillende samenstellingen van de actieve laag geven aan dat er heel veel oppervlakterecombinatie is in het geval Al-bevattende actieve lagen (actieve lagen met InGaAlAs). De hoge oppervlakterecombinatie leidt tot heel hoge drempelstromen en veel interne opwarming van de actieve laag en beiden komen

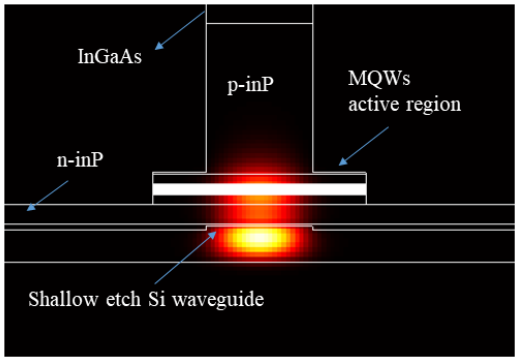

Figuur 2: Modeprofiel in de III-V/Si dwarsdoorsnede.

de vermogensefficiëntie niet ten goede. Oppervlakterecombinatie is veel minder bij InGaAsP quantumputlagen en deze warden dan ook gebruikt voor de realisatie van laser diodes met hoge efficiëntie. De metingen van de interne verliezen geven aan dat deze veel groter zijn dan de spiegelverliezen, terwijl voor een hoge efficiëntie de spiegelverliezen en interne verliezen best ongeveer gelijk zijn. Die interne verliezen zijn vooral hoog door de grote overlap van de golfgeleidermode met de sterk absorberende p-gedopeerde mantellagen. Dit is op zijn beurt te wijten aan de grote etsdiepte, gebruikt bij zowel de siliciumgolfgeleider als bij het Bragg rooster. Er wordt in het proefschrift aan de hand van simulaties getoond hoe een kleinere etsdiepte van bv. 20 tot 40nm in plaats van de gebruikelijke 180nm leidt tot een golfgeleidermode die meer geconcentreerd is in het silicium en veel minder overlapt met de p-gedopeerde InP lagen. Op die manier verminderen de interne verliezen aanzienlijk. Bovendien zijn daardoor ook niet langer de lange overgangsstructuren nodig om het licht van het InP naar het silicium te koppelen en kan de laserdiode veel korter gemaakt worden. Waar de oorspronkelijke DFB lasers op silicium een totale lengte hadden van ongeveer 700 micrometer (inclusief twee 200 micrometer lange koppelingsstructuren), kan dit door de lage etsdiepte gereduceerd worden tot een totale lengte van 200 micrometer. Het modeprofiel in een dwarsdoorsnede van de laser wordt getoond in Figuur 2. Het is duidelijk dat de mode meer in het silicium geconcentreerd is en minder in het p-type InP.

Het tweede deel van het derde hoofdstuk beschrijft de verschillende fabricatiestappen die nodig zijn voor de realisatie. De golfgeleiderstructuren in het SOI worden gedefinieerd met elektronenbundellithografie, waarna ze met behulp van een droge etsstap gerealiseerd worden. Nadien wordt een stukje III-V op het SOI gebonden met behulp van een polymer die transparent is voor het infrarood licht (licht bij de golflengte 1550nm waar de lasers dienen te werken). Dit stukje III-V bevat

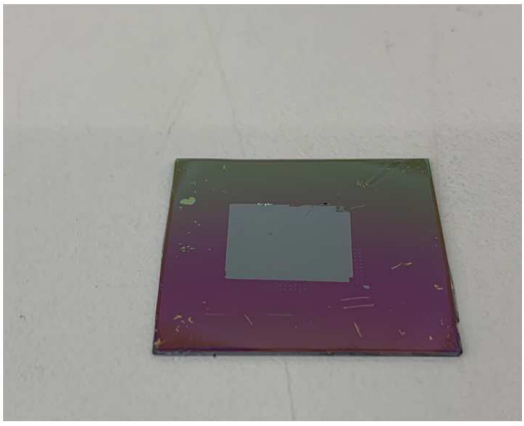

Figuur 3: SEM foto van de laserdoorsnede bekomen na verschillende lithografie- en etsprocessen.

verschillende lagen op elkaar bestaande uit een n-gedopeerde InP laag, daarbovenop een opeenvolging van InGaAsP lagen met licht verschillende samenstelling die de actieve laag definieren, en daarbovenop een p-gedopeerde InP laag en een heel sterk p-gedopeerde, maar dunne InGaAs laag. Deze laatste laag is nodig om goede contacten te kunnen realiseren. Hierbovenop is er ook nog een dik InP substraat, maar dit wordt na bonding volledig weggeëtst. Na het bonden dient ook een structuur aangebracht te worden in de III-V lagen. De diverse lithografie en etsstappen hiervoor nodig worden ook beschreven in het hoofdstuk, evenals de verschillende processtappen nodig voor het deponeren van de metaalcontacten. In Figuur 3 wordt een foto getoond van een SOI chip met daarop een InP blok gebonden. Figuur 4 toont hoe de dwarsdoorsnede van het InP op siliicum eruitziet na de verschillende lithografie- en Verstappen.

Een gedetailleerd overzicht van de karakterisatie van de in hoofdstuk drie beschreven laserdiodes wordt in het vierde hoofdstuk gegeven. Dit omvat o.a. de LIV karakteristieken die het optische uitgangsvermogen (L) en de spanning tussen de contacten (V) geven als functie van de ge ï ïnjecteerde stroom . Uit deze karakateristieken valt te besluiten dat de lasers naast een hoge differentiele efficiëntie er ook een heel lage serieweerstand is. Dit is opmerkelijk omdat de serieweerstand omgekeerd evenredig is met de laserlengte. De hoge differentiele efficiëntie en de lage serieweerstand leiden ook tot een heel hoge vermogensconversie-efficiëntie. Alle gefabriceerde laserdiodes vertonen ook een optisch spectrum bestaande uit 1 lijn; maw de laserdiodes zijn monomodaal en hebben een sterke zijmode-onderrukking.

Bij de eerste generatie laserdiodes werd bovendien ook een hoge modulatieband-

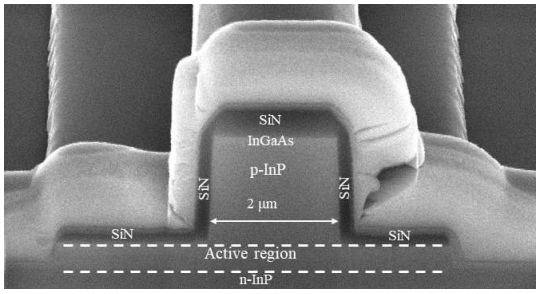

Figuur 4: Foto van een SOI chip met daarop een InP blok gebonden.

breedte van GHz gemeten. De laserdiodes konden dan ook gebruikt worden voor de generatie van 20Gb/s signalen en voor hun transmissie over 2 km glasvezel.
Aan het ontwerp van deze eerste generatie zijn nog verbeteringen aangebracht (zoals een iets kleinere etsdiepte, het beperken van het Braggrooster tot het centrale deel van de golfgeleider en het voorzien van een nagenoeg 100% reflecterend breedbandig Bragg rooster aan 1 zijde van de laser. Deze veranderingen leiden tot een nog betere efficientie, terwijl het nauwere Braggrooster de golfgeleider echt monomodaal maakt.

Bij de tweede generatie laserdiodes is ook de relatieve intensiteitsruis en de frequentieruis onderzocht. Bij voldoende hoge stroom blijft de relatieve intensiteitsruis (RIN) onder de -140dB/Hz tot aan frequenties van 20 GHz. Bij lage frequenties, beneden de 4 GHz blijft de RIN zelfs onder de -150dB/Hz. Het spectrum van de

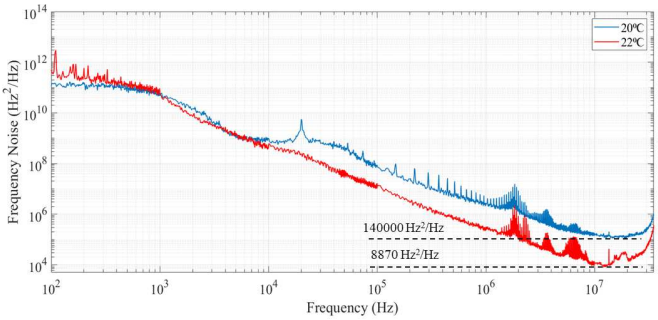

Figuur 5: Spectrale dichtheid van de frequentieruis van een heterogeen geïntegreerde DFB laser bij 20 en 22 °C .

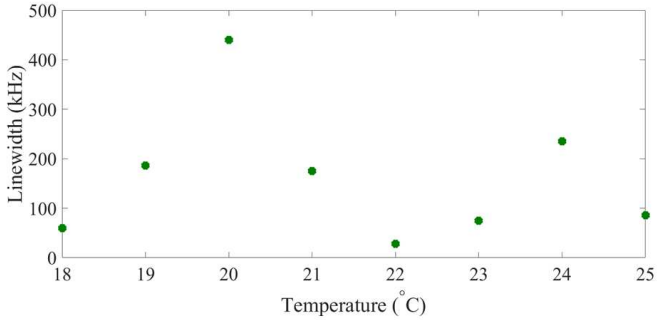

Figuur 6: Lorentziaanse lijnbreedte vs. temperatuur.

frequentieruis werd vooral gebruikt om er de Lorentziaanse lijnbreedte uit af te leiden. Er wordt aangetoond dat de lijnbreedte sterk varieert met de temperatuur. Dit komt door de invloed van de externe reflectie afkomstig van de roosterkoppelaar waarmee het licht naar vezel gekoppeld wordt. Deze roosterkoppelaar bevindt zich op een afstand van 1350 micrometer van de laser en temperatuursvariaties leiden tot een fazevariatie van deze externe reflectie. Door te meten bij een optimale temperatuur kon een minimale Lorentziaanse lijnbreedte gemeten worden van 440 kHz. Figuur 5 toont het spectrum van de frequentieruis bij 2 temperaturen. De variatie van de Lorentziaanse lijnbreedte met temperatuur is te zien in Figuur 6. Het laatste hoofdstuk tenslotte omvat een korte samenvatting van het werk en de belangrijkste resultaten, maar kijkt ook naar wat er verder nog zou kunnen verbeterd worden aan de laserdiodes.

Verbeteringen van de efficiëntie zijn o.a. nog mogelijk door het verhogen van de spiegelverliezen. Tot nog toe bleek uit metingen dat de spiegelverliezen een stuk lager waren dan de interne verliezen, maar de beste efficiëntie wordt bekomen wanneer spiegelverliezen en interne verliezen ongeveer gelijk zijn. De spiegelverliezen van een DFB laserdiode kunnen verhoogd worden door de Bragg reflecties minder sterk te maken. Dit kan ofwel door het rooster minder diep te etsen (maar wel de etsdiepte van de golfgeleider te behouden), ofwel door het Braggrooster slecths over een deel van de golfgeleider te etsen.

Evenwel kunnen ook de interne verliezen, en dan vooral de verstrooiing aan de golfgeleiderwanden, nog verder geminimaliseerd worden, bijv. door een vermindering van de ruwheid van de golfgeleiderwanden. Dit zou mogelijk moeten zijn door de processtappen verder te optimaliseren. De lijnbreedte zou nog verder kunnen verlaagd worden door de externe reflectie (en dus de koppeling naar glasvezel) verder van de laser te kiezen. Het effect van externe reflecties op lijnbreedte hangt namelijk sterk af van deze afstand. Tenslotte zou in de toekomst dit werk gemakkelijk kunnen uitgebreid worden naar lasers die in de O-band (rond 1300nm

golflengte) werken in plaats van de C-band (rond 1550nm golflengte) zoals het geval is voor de lasers bestudeerd in dit doctoraat. O-band lasers worden veel gebruikt in datacoomunicatie. De lasers kunnen in principe ook gefabriceerd worden met zgn. Micro-transferprinting techniek.

English summary

As data rates between processors in modern information processing systems increase, the unprecedented required bandwidth and low power consumption go beyond the capability of the conventional copper interconnects. To address these needs, silicon photonics can be a viable alternative by offering optical interconnects in those advanced electronic systems using mature complementary metal–oxide semiconductor (CMOS) fabrication processes. It provides advantages in producing integrated circuits (ICs) with higher capacity, lower cost optical interconnects as well as solving electrical interconnect limits in datacenters and supercomputers. It also improves the scaling of photonics to high levels of integration with improved performance and better process control at low cost.

There has been lots of progress in developing integrated optical platforms in silicon photonics including passive elements as well as high speed and large bandwidth modulators and photodetectors. However, an efficient and reliable integrated laser source has still remained a technology challenge. Due to the indirect bandgap of the silicon, making an efficient light emitter is one of the most challenging issues in silicon photonics. Since the final package size and cost of the optical transceivers play an important role for employing silicon photonics chips in commercial applications such as datacom, high-efficiency and small footprint integrated light sources are highly desirable. Among the possible integrated light sources, edge emitting laser diodes such as distributed feedback (DFB) lasers or distributed Bragg reflector (DBR) lasers are desirable when fabricating low-cost integrated transmitters for O-band and C-band wavelength division multiplexing (WDM) systems. In addition, they exhibit high modulation bandwidth and output power.

Different integration methods have been used to combine III-V lasers with silicon photonics, which are discussed in detail in chapter one. The hybrid integration has been demonstrated as a viable approach in providing the required optical sources. However, challenges such as scaling limitations and alignment precision limit the applications of this approach. Another promising approach is the direct epitaxial growth of III-V materials on the silicon substrate. High performance light sources based on quantum dot active regions have been fabricated using this technique. However, for integration of QD layers on silicon, thick buffer layers on top of the silicon are required and that makes coupling to a silicon waveguide (and thus also using gratings in silicon) difficult. On the other hand, due to the high density of the threading dislocations (TDs) caused by the mismatch of lattice constants

and thermal expansion coefficients, it is difficult to achieve high quality layers for efficient lasing in multiple quantum well (MQW) lasers. Heterogeneous integration proved to be another viable alternative for the realization of high-performance compact lasers onto the SOI platform. This technique is mainly based on bonding or micro-transfer printing. In molecular or adhesive bonding, the III-V material is first bonded to silicon and then processed into active components such as lasers or amplifiers. In the micro-transfer printing technique, the III-V material is first processed on its own substrate to make components as coupons, and then these coupons can be micro-transferred to SOI photonic integrated circuits to fabricate lasers or in general photonic integrated circuits.

In this thesis we focus on the heterogeneously integrated InP-on-Si DFB lasers. In the second chapter, the theory of the DFB lasers is discussed and useful relations are described using coupled mode and rate equations models. The concept of wall-plug efficiency as well as the effect of the external feedback on the intrinsic linewidth of the solitary laser diode are discussed. To design an integrated III-V-on-Si short

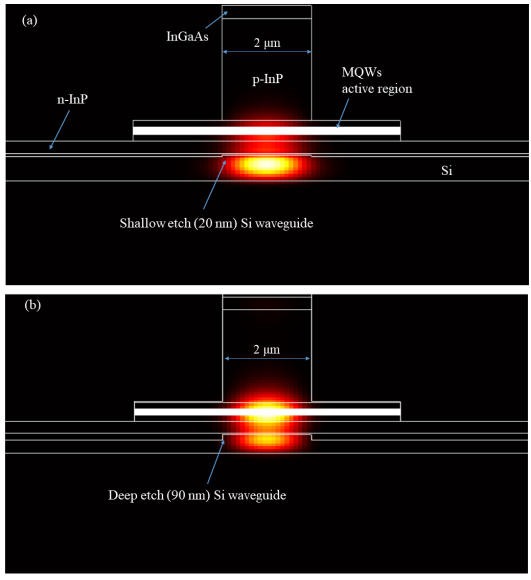

Figure 7: Profile of the fundamental optical mode in the III-V/Si cross-section. a) Mode profile in the laser cross-section with a shallow etch silicon waveguide and a narrow mesa. b) Mode profile in the laser cross-section with a deep etch silicon waveguide and a wide mesa.

cavity laser, it is necessary to accurately analyze the optical mode profile in the III-V/Si cross-section. While in earlier demonstrations of heterogeneously integrated III-V-on-Si DFB lasers in the Photonics Research Group (PRG) at Ghent university-IMEC, the optical mode is predominantly confined to the active III-V waveguide layer (typically using a 400 nm thick silicon waveguide layer incorporating a 180 nm etched DFB grating), in our design the optical mode is strongly confined to the silicon waveguide layer. Figure 7 shows the vertical cross-section of the III-V/Si waveguide where the fundamental optical mode profile is simulated for a specific epitaxial structure used in this work. As shown in Figure 7(a), by using a shallow etch (40 nm) silicon waveguide, the fundamental optical mode is strongly confined to the silicon. The confinement factor of the fundamental mode in the active region as well as the internal loss are calculated as 3.5% and 5.58 cm^{-1}, respectively. On the other hand, for a deeply etched (180 nm) silicon waveguide configuration shown in Figure 7(b), the fundamental optical mode is strongly confined to the III-V active waveguide layer with a confinement factor and internal loss of around 6.8% and 19.5 cm^{-1}, respectively. In order to make a short cavity III-V-on-Si DFB laser, the mode has to be sufficiently confined to the active region to provide sufficient gain for lasing. On the other hand, according to the simulation results, as the optical mode is more confined to the silicon waveguide, it will experience lower optical absorption loss since there are no doped layers in the silicon waveguide and the mode has less overlap with the highly absorbing III-V material. In addition, in order to fully couple the hybrid mode to the silicon waveguide, very short taper structures can be used and the requirement for long adiabatic taper configurations used in the earlier designs relaxes.

The fabrication processes flow is explained in the third chapter. The process starts with the fabrication of the silicon-on-insulator (SOI) circuit in the UGent-IMEC cleanroom, using an electron beam lithography and dry etching. After the preparation of the SOI sample, a very thin layer of DVS-BCB polymer is spin coated on the SOI sample and the InP epitaxial structure is bonded to this SOI using a Suss MicroTec ELAN CB6L wafer bonding machine. After that, the InP substrate as well as the sacrificial layers are removed using wet etch processes. Subsequently, the III-V processing steps such as lithography, etching, deposition and metallization are carried out to fabricate III-V-on-Si DFB lasers.

The final chapter of this thesis covers the measurement results obtained from the characterization of the fabricated III-V-on-Si lasers. Several devices with InGaAsP or InAlGaAs multiple quantum well (MQW) active region have been characterized and the results are discussed. In the following sections a brief explanation of the experimental results is given.

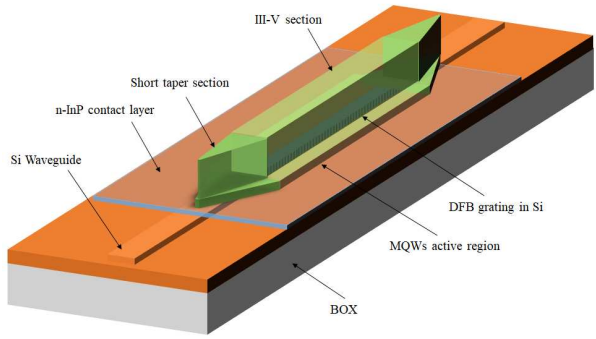

Figure 8: Schematic structure of the III-V-on-Si DFB laser with symmetric output waveguides.

1 DFB lasers with symmetric output waveguides

Figure 8 shows the schematic of a heterogeneously integrated DFB laser realized by adhesive bonding. This 200 µm long DFB laser is fabricated on a SOI platform consisting of a 400 nm thick silicon device layer on a 2 µm buried oxide (BOX) layer. The cavity is determined by a 1 µm wide, first order, quarter-wave shifted grating in the silicon with a 60 nm etch depth. The 60 nm etched silicon waveguide is then connected to a 180 nm etched silicon waveguide in which the 180 nm etched grating couplers are incorporated. In the III-V section, the epitaxial layer stack consists of

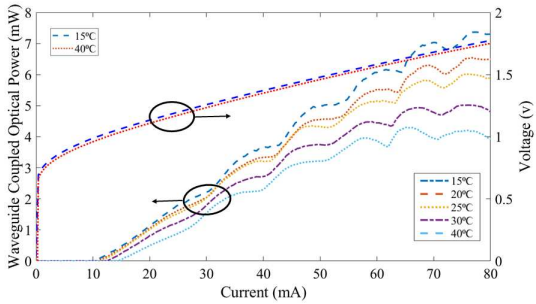

Figure 9: Waveguide-coupled optical output power (single-sided) versus DC bias current (left), and I-V curves (right) at various operating temperatures.

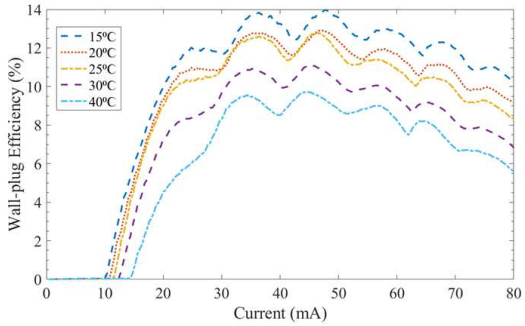

Figure 10: Wall- plug efficiency versus bias current at various operating temperatures for the 200 μm long cavity DFB laser.

a 200 nm thick highly-doped p-InGaAs contact layer, a 1.5 μm thick p-InP cladding layer, an InGaAsP MQW active region with 6 quantum wells surrounded by 100 nm thick separate confinement heterostructure (SCH) layers, and a n-InP contact layer with a thickness of 190 nm. The laser mesa is 2 μm wide and consists of two short spot-size converters at the ends. The DFB laser's L-I curve is measured at different stage temperatures and the results are depicted in Figure 9. The measured threshold current at 20 °C is 10.5 mA and it increases up to 14.5 mA by increasing the operating temperature to 40 °C. A waveguide-coupled optical power up to 6.5 mW is obtained from a single facet. Due to the symmetrical configuration, the same results are obtained from the other output of the laser. The wall-plug efficiency of the laser as a function of the bias current at different operating temperatures is shown in Figure 10. As can be seen, more than 12% wall-plug efficiency is achievable at room temperature.
We also reported the dynamic characteristics of the laser diode by measuring the small-signal and large-signal modulation responses. Up to 15 GHz modulation bandwidth is obtained at the bias current of 60 mA. The data transmission experiment with NRZ modulation depicts open eye diagrams up to 20 Gb/s without using any equalization.

2 DFB lasers with a single output waveguide

Figure 11 depicts the schematic of an InGaAsP DFB laser integrated on the SOI platform as described in the previous section. The laser cavity is 180 μm long and is defined by a 40 nm surface etched, first order Bragg grating. In order to increase the single facet output power, a broadband reflector is incorporated in the silicon

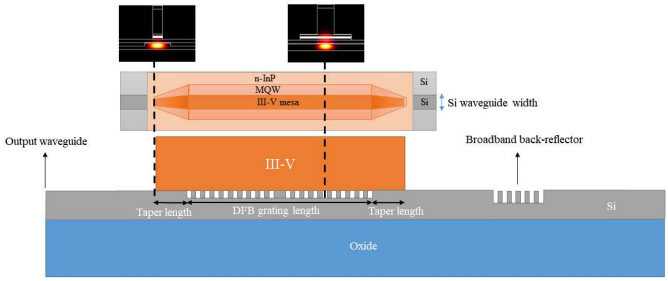

Figure 11: Schematic structure of the III-V-on-Si DFB laser with a single output waveguide.

waveguide at one side of the cavity. The static characteristics of the fabricated devices exhibit more than 11 mW output power coupled to the silicon waveguide at a bias current of 60 mA. The measured series resistance of these devices is around 9 Ω and the side mode suppression ratio (SMSR) larger than 55 dB is achieved. Figure 12 depicts the wall-plug efficiency versus the bias current at 20 °C and 40 °C. More than 16% wall-plug efficiency is achieved at 20 °C for bias currents below 40 mA which shows an improvement of 4% compared to the work described in the previous section. It also shows the laser performance in a semi-cooled operation regime with a wall-plug efficiency up to 10%.

After that, the spectral densities of the frequency and relative intensity noise of the lasers are measured. Figure 13 shows the spectrum of the frequency noise of

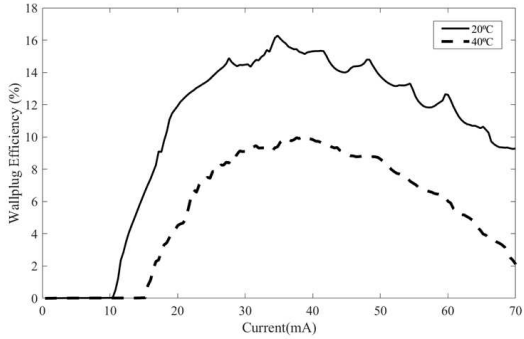

Figure 12: Wall-plug efficiency versus bias current for the 180 μm long cavity III-V-on-Si DFB laser.

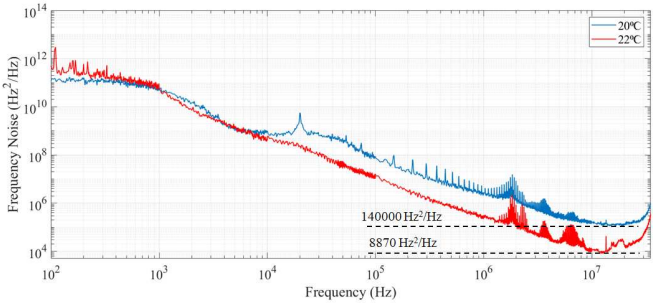

Figure 13: The spectral density of the frequency noise versus frequency at two operating temperatures. The Lorenzian linewidth is calculated by multiplying the white noise level (the flat part of the spectra) by π.

the laser measured by a OE4000 phase and frequency noise test system without using an optical isolator. The power spectral density (PSD) of the Gaussian white noise is found to be 140 × 103 Hz^2/Hz at 20 °C. An intrinsic (Lorentzian) linewidth of 440 kHz has been calculated by multiplying the white noise PSD value by π. Besides the low loss silicon platform, this reduction in the solitary laser linewidth can also be attributed to the weak feedback effect of the external cavity formed by the grating coupler. We observed that the laser linewidth can be decreased by an order of magnitude by changing the operating temperature, which results in a phase variation of the external reflection. As shown in Figure 13, the measured frequency noise spectrum at 22 °C corresponds to an intrinsic linewidth of 28 kHz. Subsequently, the RIN was measured with an electrical spectrum analyzer. Measurement results show a low relative intensity noise below -150 dB/Hz at 60 mA up to 6 GHz. Finally, dynamic characterization of these short cavity lasers has been carried out and 20 and 10 Gbps directly modulated data transmission have been reported at a bias current of 50 mA at 20 °C and 40 °C, respectively.

3 Conclusion

This PhD thesis focused on the development of the heterogeneously integrated C-band DFB lasers realized by the adhesive bonding. We demonstrated small footprint and high wall-plug efficiency III-V-on-si DFB lasers by optimizing the design and fabrication process flow. The potential low noise performance of a solitary III-V-on-Si DFB laser is discussed by characterizing the intrinsic laser linewidth and RIN. Although, the performance of these devices can still be improved as discussed in this thesis, the design concept described in this work can be applied to O-band

lasers to serve the datacom market. In addition, the potential of the micro-transfer printing technique to apply the same design concept will be the next goal.

1

Introduction

1.1 Optical Communication Links 1-2
1.2 Silicon Photonics 1-3
1.3 III-V/Si Integration Techniques 1-5
1.3.1 Hybrid integration 1-5
1.3.2 Heterogeneous integration 1-9
1.3.3 Direct epitaxial growth 1-13
1.3.4 Regrowth on a bonded template 1-14
1.4 State-of-the-art heterogeneously integrated InP-on-Si single mode lasers 1-15
1.4.1 Distributed Feedback lasers 1-16
1.4.2 Distributed Bragg Reflector lasers 1-18
1.4.3 Widely tunable lasers 1-19
1.5 Research objectives 1-19
1.6 Outline of the thesis 1-20
1.7 Publications 1-22
1.7.1 Publications in international journals 1-22
1.7.2 Publications at international conferences 1-22

This dissertation discusses research carried out in the field of silicon photonics, with a focus on laser integration. In this introductory chapter, first we give an overview on optical communication links and the motivation to move towards

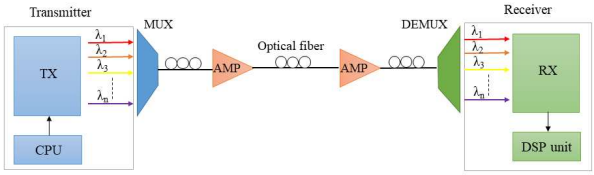

Figure 1.1: A simplified schematic of an optical communication link.

integrated photonics. Then the state-of-the-art on integration techniques as well as the corresponding fabricated edge-emitting lasers followed by the outline of the thesis are given.

1.1 Optical Communication Links

The era of fiber-optic communications was started by the fabrication of the first low loss optical fibers. In 1976, the first experimental data transmission at a bit rate of 44.736 Mbps was carried out in Bell laboratories [1]. Later, by developments in technologies such as wavelength-division multiplexing (WDM) or time-division multiplexing (TDM) as well as significant progress in the optical fibers' capacity, over 2 Pbps data transmission has been achieved using a single fiber [2]. A simplified schematic of an optical communication link is displayed in Figure 1.1. Semiconductor lasers, which are coherent light sources, are extensively used as the light sources in an optical communication link [3].
Among the demonstrated laser light sources, vertical cavity surface emitting lasers (VCSELs) as well as edge-emitting laser diodes operating at a particular wavelength, such as distributed feedback (DFB) or distributed Bragg reflector (DBR) lasers are preferred. VCSELs, where the lasing cavity is perpendicular to the chip surface, are usually used for short-range transmission in datacenter networks. On the other hand, for the long-haul communications edge emitting lasers such as DFB lasers are the appropriate candidate due to their higher output power. Unlike VCSELs, DFB and DBR lasers can be used for O-band and C-band wavelength division multiplexing (WDM) systems in an optical communication link.

The input data generated as an electrical signal by the central processing unit (CPU) are converted to an optical signal using an external or a direct modulation technique. In the external modulation, the data stream is imposed on the laser light after generation while in the direct modulation technique the laser output is modulated by the input drive current. In order to increase the data transmission capacity of an optical link, a wavelength division multiplexing (WDM) technique is used

by adding a multiplexer component in the link. The multiplexer receives different wavelengths carrying data signals from different transmitters and combines them into one beam of light containing multiple optical wavelengths to be transmitted simultaneously over a single fiber for short or long distances. Depending on the network, the operating wavelength and the distance over which the optical signal has to propagate, optical amplifiers are needed to compensate for the attenuation. At the receiver side, the beam of light is separated back into the individual data channels by means of demultiplexers. The receiver, consisting of an array of photodiodes converts the optical signals to electrical signals and depending on the distortion or the attenuation, an amplifier and equalizer might be needed to restore the main signal.

1.2 Silicon Photonics

As the size of the electronic components is approaching the atomic scale, the electronics industry embraces the "more than Moore" concept to increase the integration level of data center infrastructures. To this end, the future generation of complementary metal-oxide-semiconductor (CMOS) technology must not only scale down the transistor dimensions, but also needs to apply various integration technologies for novel processing architectures. Silicon photonics technology, which enables the integration of photonic components on a silicon substrate using CMOS fabrication technology, is a key technology in this respect.

It provides advantages in producing integrated circuits (ICs) with higher capacity, lower cost optical interconnects as well as solving electrical interconnect limits in datacenters and supercomputers. It also facilitates the scaling of photonics to high levels of integration with improved performance and better process control at low cost. The significant performance of silicon photonics in WDM, scaling to > 1 Tb/s transceivers is of great importance [5].

During the past decade, there have been rapid advances both in research and commercialization of silicon photonics components. High-performance passive components such as optical waveguides and couplers can be realized on SOI using mature CMOS fabrication processes [7]. Additionally, high-performance silicon optical modulators based on the plasma dispersion effect have been demonstrated successfully [8]. Germanium, which is a CMOS compatible material enables the fabrication of ultra-fast photodiodes on silicon [9]. However, due to their indirect bandgap structure as shown in Figure 1.2, it is impossible to realize efficient light sources in silicon or germanium. This issue leads to the need for integrating III-V materials onto SOI to realize efficient light sources at 1.3 or 1.55 μm.

By utilizing the mature processes and tools from the CMOS industry, high-resolution patterning and dense integration of optical circuits on a chip are possible [10]. As

depicted in Figure 1.3, silicon photonics is now growing at a compound annual growth rate of 44.5% in the optical transceivers market [6].

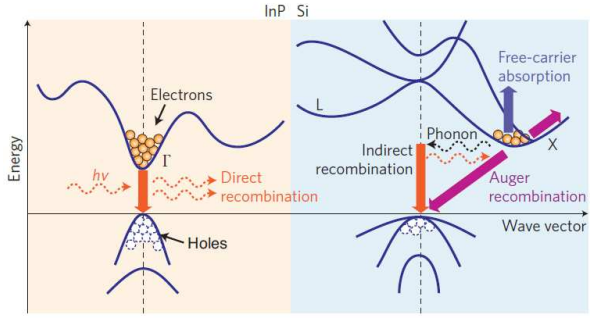

Figure 1.2: Energy band diagrams and major carrier transition processes in InP and silicon crystals. The electron-hole recombination in a direct bandgap structure (such as InP) shown on the left, results in photon emission while in an indirect bandgap structure (such as Si) depicted on the right, a weak photon emission occurs based on a phonon-assisted electron-hole recombination [4].

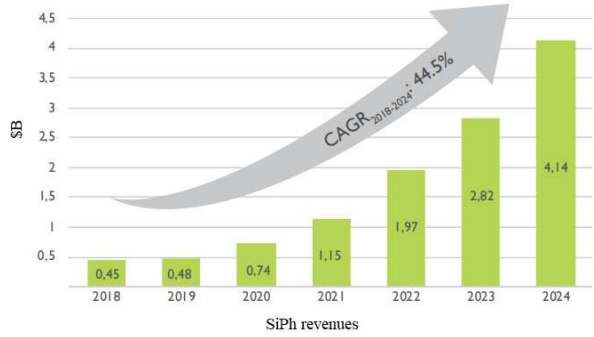

Figure 1.3: 2018-2024 silicon photonics transceiver forecast [6].

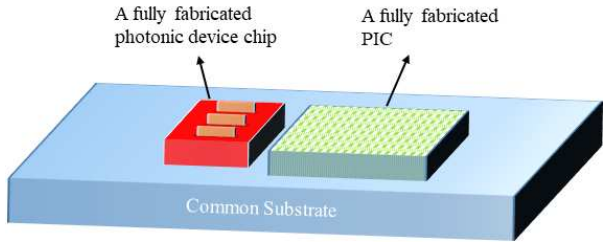

Figure 1.4: A simple schematic of the hybrid integration technique. A gain chip is placed next to a Si PIC where both chips are mounted on a separate common substrate.

1.3 III-V/Si Integration Techniques

Different integration methods have been used to combine III-V lasers with silicon photonics. The following sections discuss the different integration approaches used either in research or industry.

1.3.1 Hybrid integration

As illustrated in the Figure 1.4, the hybrid integration approach includes all techniques of integration using the optical connection of photonic device chips such as lasers to an adjacent silicon photonics circuit. Using this approach, the superior performance of the native III-V gain chip can be maintained on its own substrate. In the following, different techniques of hybrid integration are discussed.

1.3.1.1 Photonic wire bonding

Photonic wire bonding (PWB) is an optical integration and packaging technique which connects different optical components using low insertion loss and free form wires made by beam-shaping elements [11, 12]. This connection can be made between two silicon photonics chips or from a standalone component such as a laser to a silicon photonics chip. Figure 1.5 depicts a SEM micrograph of a multi-chip assembly of passive silicon photonic waveguides with an InP DFB laser array using wire bonds. In order to connect two chips by photonic wire bonds, first they are mounted on a common substrate and loaded into a photonic wire bonder. Then, the photoresist is dropped onto areas of interest and by using automated image recognition software the alignment markers and waveguides are

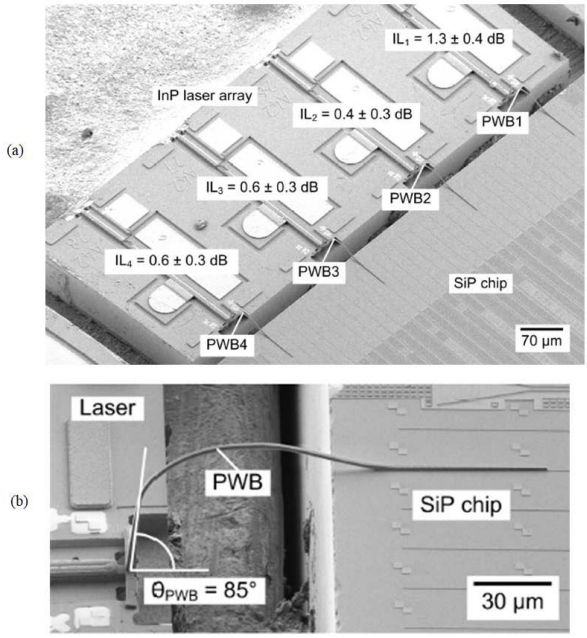

Figure 1.5: Hybrid multi-chip module combining passive silicon photonic waveguides with an InP DFB laser array. a) A SEM image of the chip, including four laser diodes (LD1…LD4), each connected to a silicon photonic on-chip waveguide via a PWB (PWB1…PWB4). b) Side-view of PWB1 [13].

found. The tool afterwards calculates the trajectory that minimizes the bend loss of the 3D waveguides. After that, a direct-write two-photon laser lithography [14] is performed to polymerize photoresist which is followed by a development process to wash away the resist that has not been polymerized. Finally, the photonic wire bonds are encapsulated by means of a lower refractive index material.
Low optical insertion loss of 0.4 dB per bond is reported in connecting InP-based edge emitting laser diodes to a passive silicon photonic circuit [13]. The technique does not need any active alignment and a high optical misalignment tolerance is achievable by recent developments. However, the integration approach does not scale well to a large number of optical interfaces.

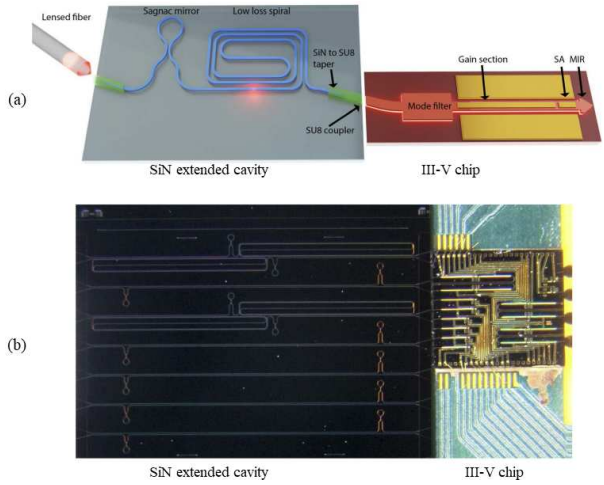

Figure 1.6: Butt-coupling integration technique. a) A schematic of a designed SiN extended cavity butt-coupled to a III-V chip. b) The fabricated integrated chip where the SiN external cavity and the active chip mounted to the PCB contain several laser structures [17].

1.3.1.2 Butt-coupling

In this technique, light is coupled between chips in the same plane. In other words, the light beam is coupled in or out in laterally between chips. Thus, in order to achieve high coupling efficiencies (typically larger the 80 %) high quality facets have to be made on all components involved in the process and the mode matching requirement needs to be met [15]. Figure 1.6(a) depicts the design schematic of a III-V chip butt-coupled to a SiN extended cavity. Based on this schematic, several laser structures are integrated to a SiN chip as shown in Figure 1.6(b).
Lionix demonstrated up to 100 mW on chip optical power by butt-coupling multiple gain sections sharing a common laser mirror. The integrated lasers show a low intrinsic linewidth of 320 Hz as well as a low relative intensity noise of <-160 dBc/Hz [16].

1.3.1.3 Flip-chip bonding

The concept of this integration technique was first introduced by IBM in the late 1960s, and was known as controlled collapse chip connection (C4) for microelectronic assembly [18]. In contrast to other techniques of hybrid integration, the flip-chip approach directly connects face-down electrical or optical components onto the substrate using solder or conductive polymer bumps between the chip and the substrate [19].

Flip-chip bonding has been used a lot in the past two decades to integrate III-V active components on silicon photonics platforms [20, 21]. The III-V active components are fabricated on their own substrate using mature standard III-V processes and can be tested prior to integration on the silicon photonics circuits. Figure 1.7 illustrates this technique used in the integration of an SOA on a silicon photonics platform. As shown schematically in Figure 1.7(a), the fabricated SOA is diced and is flipped to be bonded on the silicon trench created by removing the upper cladding layer, the silicon layer, and the BOX layer. This needs both the III-V component and the substrate to be aligned by performing passive alignment using alignment markers on the SOA and the silicon photonic platform. After depositing AuSn as

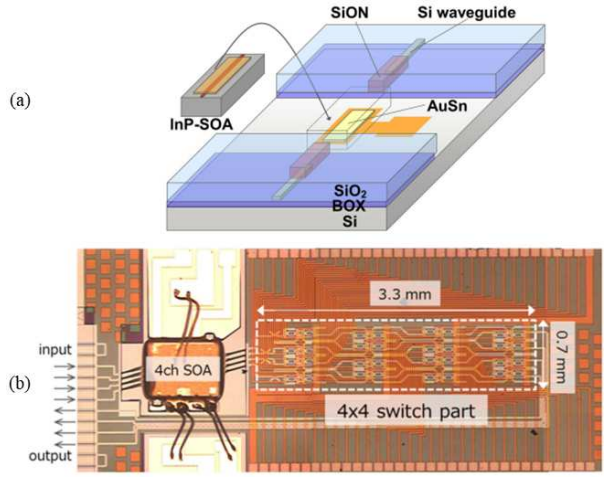

Figure 1.7: Flip-chip bonding integration technique. a) A schematic of a flip-chip approach for providing in-line amplification. b) The fabricated integrated chip where the SOA is flip-chip bonded to a silicon substrate. [20].

a solder, the face-to-face integration is carried out by means of a flip-chip bonder. The horizontal and vertical alignment are done within the alignment accuracy of the machine. In addition, the load of the bonder controls the thickness of the solder by providing the desired temperature. Figure 1.7(b) depicts the fabricated chip with the integrated SOA on the Si substrate using the aforementioned steps [20, 22].

1.3.2 Heterogeneous integration

Heterogeneous integration refers to the transfer of a non-Si component or thin film onto a silicon photonics platform. Unlike in the hybrid integration approach, here the III-V material is detached from its own substrate either before or after integration. Different techniques of heterogeneous integration are discussed in the following sections.

1.3.2.1 Die or wafer bonding

Bonding of a III-V epitaxial layer structure onto a SOI platform is the most common heterogeneous integration technique. In this approach, an unprocessed III-V die or wafer is bonded to a pre-processed silicon photonics die or wafer. As shown in Figure 1.8, multiple dies or wafers can be bonded to provide different functionalities on the silicon photonics chip.
Based on the material used in the interface of the III-V die or wafer and the silicon photonics die or wafer, this technique can be categorized into direct, molecular, metallic, and adhesive bonding. In direct bonding, two surfaces join directly by means of covalent bonds between them without using any intermediate layers [23]. Strict requirements such as a very high annealing temperature (higher than 500 °C) for a reliable bonding and surface cleanness, as well as the possible lattice mismatch issues, limit the use of this technique in heterogeneous integration [24]. The other techniques release these requirements by applying an appropriate interfacial layer. In molecular bonding, a thin film of a few nanometers typically consisting of a dielectric forms a strong covalent bond between silicon and the III-V material [25, 26]. This results in a lower required annealing temperature and reduces the surface roughness and topography requirements.
Eutectic bonding and thermo-compression bonding are the most important types of the metal bonding technique. Due to the opical absorption and the post-bonding fabrication limitations regarding the heterogeneous integration, this technique is typically used in the packaging of micro-electro-mechanical systems (MEMS) [27]. Finally, another approach which uses a proper polymer as the interfacial layer is called adhesive bonding. The most common polymer used as a glue to mate the III-V epitaxial layer and the silicon photonics chip is DVS-BCB (divinylsiloxane-

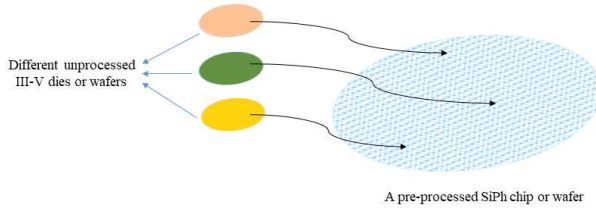

Figure 1.8: Schematic of a wafer-to-wafer bonding process. After the completion of the bonding process, the III-V substrate is selectively removed and standard III-V processing is performed to pattern the III-V devices.

bis-benzocyclobutene) [28]. Significant advantages are provided using adhesive bonding as a heterogeneous integration technique. It is highly tolerant to the surface roughness and cleanness. The surface preparation for both the III-V epitaxial layer and the SOI is limited and protection to the patterned features on the SOI is provided. Using this polymer, an annealing temperature lower than 280 °C suffices for a reliable bonding process. However, DVS-BCB has a very low thermal conductivity compared to the silicon and III-V materials which is a potential issue especially in the integration of light sources [29, 30].

1.3.2.2 Micro-transfer-printing

Micro-transfer printing (μTP) is another heterogeneous integration technique in which partially or fully fabricated components are printed on the desired locations of the prefabricated target chip. This technique is based on the switching between adhesion and release of loosely bound devices to and from an elastomeric material called stamp. This switching between adhesion and release is controlled through controlling the velocity of the stamp [31]. Figure 1.9 shows the general schematic of different steps of this technique. First the components or devices are fabricated on their own substrate called donor or source. Then a soft elastomeric stamp such as a commercially available polydimethylsiloxane (PDMS) rubber is contacted to the surface of the source. In order to have a sufficient adhesion to pick up the components, the velocity of the PDMS stamp has to be higher than a critical value. This phenomenon is a prerequisite to a successful picking by providing sufficient separation energy between transferable components and their substrate. Equation (1.1) describes the dependency of the separation energy rate [32]:

$$G = G_0[1 + (v/v_0)^n] \tag{1.1}$$

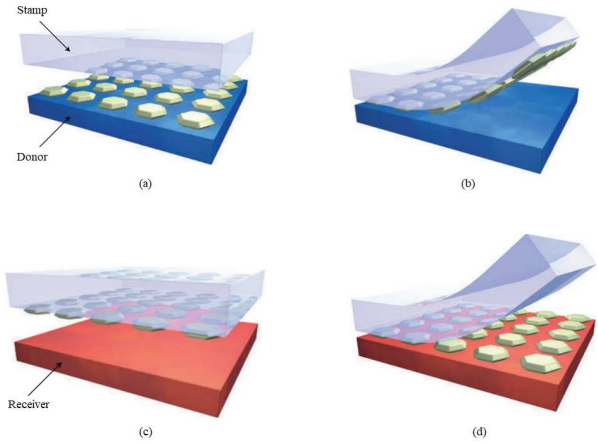

Figure 1.9: Schematic illustration of the TP integration technique. a) A source or donor containing loosely bound components as well as a stamp are prepared. b) Picking process, the stamp is brought in contact with transferable components quickly. c) The stamp containing the components is aligned with the receiving substrate. d) Printing process, The stamp containing the components is brought in contact with the receiving substrate slowly [31].

where G_0 denotes the critical energy release rate when the peeling velocity V is equal to zero, V_0 is the reference peeling velocity corresponding to an energy release rate of $2G_0$, and the exponent n is a fitting parameter which can be determined experimentally [32]. As can be derived from equation (1.1), at a speed higher than the critical speed V_c, the separation energy between the stamp and film (or transferable components) is higher than the separation energy between the film and its donor substrate. The critical velocity V_c is found as [32]:

$$V_c = V_0\left(\frac{G_{film/substrate} - G_0}{G_0}\right)^{\frac{1}{n}} \tag{1.2}$$

This mechanism corresponds to a picking process as depicted in Figure 1.10. After a successful picking process, the stamp will be aligned on a specific location of the receiver substrate for the printing process (Figure 1.9 (c,d)). Regarding the printing process, a reverse of the picking mechanism is required to have a stronger adhesion between the receiver substrate and the film than between the film and the stamp. This is achieved by operating at a speed slower than V_c [33].

The above-mentioned scenario seems to be straightforward for films with weak bonds to their donor substrate. The scenario can be different for III-V films that

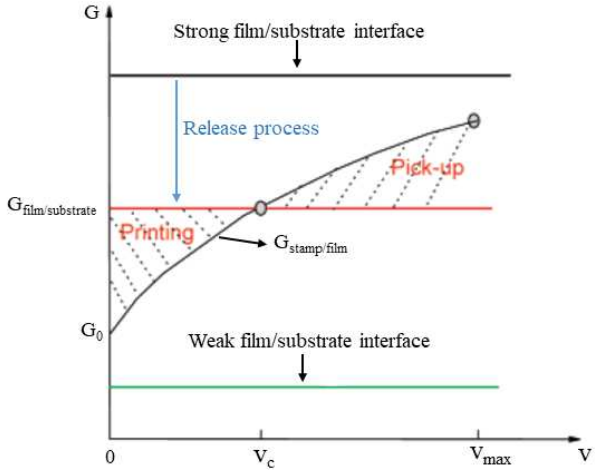

Figure 1.10: Schematic illustration of the separation energy rates between the film and substrate as well as the substrate and stamp. Very weak and very strong interfaces between film and substrate are shown with horizontal lines at the bottom and top of the diagram, respectively, corresponding to pickup only and printing only [32].

have strong chemical bonds to their substrate. As Figure 1.10 illustrates, the required separation energy rate for the strong interface between the film and the corresponding substrate is much higher than the provided separation energy by the stamp in the picking process. In order to overcome the issue of picking up the III-V film from its substrate, an appropriate release layer has to be grown on top of the source substrate. After a top-down fabrication process, a proper selective under-etching of the release layer is used to tether the fabricated devices to the

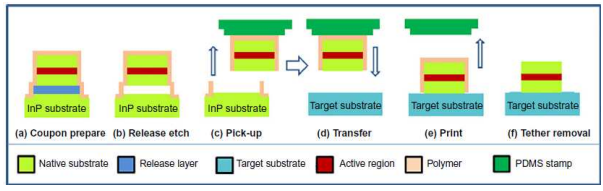

Figure 1.11: Schematic illustration of the TP technique for integration of III-V material onto a target substrate [34].

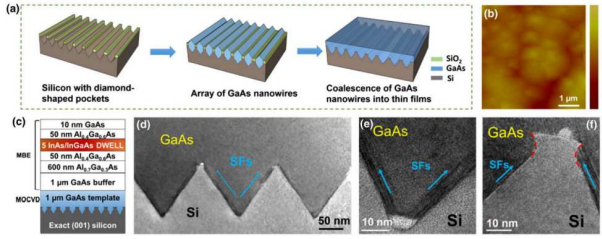

Figure 1.12: Illustration of the epitaxial growth of InAs QDs micro-disks on GoVS substrate. (a) Procedure of growing antiphase-domain-free GaAs thin films out of a highly ordered array of planar GaAs nanowires on silicon substrates with diamond-shaped pockets. (b) AFM image of approximately 1 μm coalesced GaAs thin film grown on the nanowire arrays. The vertical bar is 25 nm. (c) Schematic of the as-grown structure. (d)-(f) Cross- sectional TEM images of the V-grooved structure, showing stacking faults (indicated by the blue arrows) trapped by the silicon pockets. Reproduced from [35, 36].

substrate (Figure 1.11). These suspended devices, anchored to the substrate, have a weaker interface with the substrate and can be picked up by breaking the tethers.

1.3.3 Direct epitaxial growth

In this integration technique, III-V crystals are grown on the SOI wafer. Due to the significant lattice mismatch between most direct bandgap III-V materials, with lattice constants between 5.6 and 6.5 Å, and the silicon with a lattice constant of 5.431 Å, as well as the differences in thermal expansion coefficient and the polar/non-polar interface, this integration technique is more challenging than heterogeneous integration approaches [37].

Several approaches have been developed for the epitaxial growth of III-V materials on silicon. Planar heteroepitaxy exploits specific techniques such as inserting intermediate layers or manipulation of a graded Ge/GeSi/Si substrate to improve the quality of the grown III-V layers by reducing defects in bulk III-V materials [38, 39]. Figure 1.12 shows one example of planar heteroepitaxy where instead of growing on a blanket silicon substrate, a GaAs-on-V-grooved-Si (GoVS) template is utilized to grow InAs quantum dots (QDs) for high performance O-band lasing [36]. Other approaches combined with planar heteroepitaxy such as using an offcut silicon substrate (4°-6° offcut angle) or incorporating a strained dislocation filter, resulted in a reduction of the defect density down to $10^5/cm^2$ [40, 41]. Using QDs as an active region, these epitaxial techniques resulted in the demonstration of high performance lasers with low threshold currents and high output powers as well as high

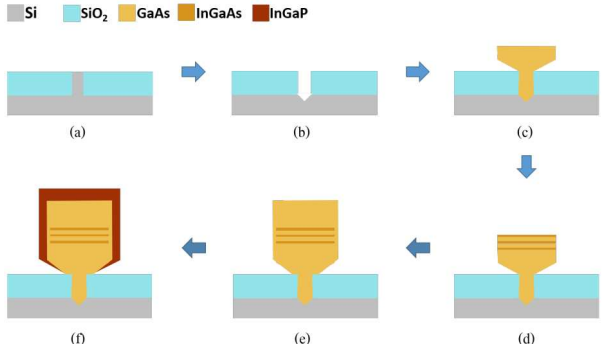

Figure 1.13: Illustration of GaAs nano-ridge epitaxy process. (a) A silicon wafer patterned with a SiO_2 mask using a shallow trench isolation process. (b) The V-shape Si trenches are obtained by tetramethylammonium hydroxide wet etch process. (c) the growth of GaAs inside and outside of the trench, respectively. (d) The growth of three $In_{0.2}Ga_{0.8}As$ QWs. (e) The growth of the top GaAs barrier and (f) Deposition of a InGaP passivation layer [35]

wall-plug efficiencies [41, 42]. However, due to the use of the intermediate layers between the active region and the silicon, these techniques encounter significant challenges in silicon photonics applications due to the inefficient coupling of the light to a silicon waveguide [43, 44].

In order to facilitate the coupling of the light to a silicon waveguide, selective area growth (SAG) is proposed. In this epitaxial growth technique, the need for using a thick buffer layer is relaxed. By applying SiO_2 as a mask on a patterned silicon substrate, the appropriate growth is performed due to the difference in the growth rate on top of the silicon and SiO_2 mask. Using SAG combined with other modification techniques such as directional heteroepitaxy, vertical/planar nanowires growth, and aspect ratio trapping (ART), CMOS compatible integrated active components have been demonstrated [35]. One example of this fabrication strategy is depicted in Figure 1.13. Using ART and nano-ridge engineering, high quality nano-ridge growth has been achieved and lasing with optical excitation has been demonstrated [35, 45].

1.3.4 Regrowth on a bonded template

This heterogeneous integration technique, as the name implies, combines the advantages of both bonding and direct epitaxial growth techniques. As Figure 1.14 illustrates, first a proper III-V die or wafer is bonded on a patterned SOI substrate.

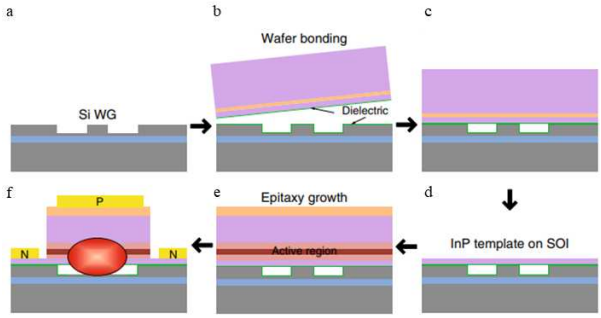

Figure 1.14: Schematic of the process flow of the regrowth on a bonded template for III-V-on-Si integration. (a) The SOI chip is patterned beforehand. (b) A III-V die or wafer such as InP is bonded on the patterned SOI. (c,d) The III-V substrate and other sacrificial or cap layers are selectively etched to leave the InP template layer on top of the SOI. (e,f) A standard active region will be grown on the III-V-on-SOI platform and the post-processing will be carried out [46].

Then, the InP substrate and other sacrificial or cap layers are selectively etched to leave the InP template layer on top of the SOI. Subsequently, a standard active region based on MQW structures or QDs will be grown on the III-V-on-SOI platform. Using a bonded III-V platform relaxes the challenges of lattice and polar/apolar mismatch mentioned in the previous section. Using this technique, a threading-dislocation density (TDD) smaller than 1×10^5 cm^{-2} is reported [46]. In addition, a scalable cost-effective manufacturing can be promised by this technique [47]. However, the more complicated fabrication process remains a significant issue in most commercial applications.

1.4 State-of-the-art heterogeneously integrated InP-on-Si single mode lasers

Semiconductor lasers are the most important and challenging components of silicon photonics. As photonic integrated circuits are penetrating in different market segments, efficient heterogeneously integrated light sources are desirable. Especially in the context of datacom, wall-plug efficiency is critical. In addition, small footprint integrated transmitters have attracted much attention to decrease the final package size and cost of the transceivers. In recent years, there have been dedicated efforts, both in academia and industry to improve the performance of various light sources

on Si [48–50]. Among the demonstrated integrated light sources, edge emitting laser diodes such as distributed feedback (DFB) lasers or distributed Bragg reflector (DBR) lasers are the preferred light sources when fabricating low-cost integrated transmitters for O-band and C-band WDM systems. In addition, they exhibit high modulation bandwidth and output power.
Here, we review integrated light sources which have been demonstrated in silicon photonics.

1.4.1 Distributed Feedback lasers

In [51], a III-V-on-silicon DFB laser based on adhesive bonding with a wall-plug efficiency of about 9% has been demonstrated at room temperature considering the output power of both facets. As shown in Figure 1.15, the reported DFB laser structure is based on a 680 μm long quarter-wave shifted second-order grating. The DFB grating is defined by a 180 nm deep etch into the 400 nm silicon. Due to the use of a deep etch in the DFB grating the optical mode is predominantly confined to the active III-V waveguide layer. In order to couple the light to the silicon waveguide underneath, two 185 μm long spot-size converters are incorporated at both ends of the cavity. The reported threshold current, the side mode suppression ratio (SMSR), and the measured intrinsic linewidth of the laser are 35 mA, 50 dB, and 1 MHz, respectively. Using the same configuration, [52, 53] demonstrated high modulation speed of III-V-on-silicon lasers with large confinement factor in the

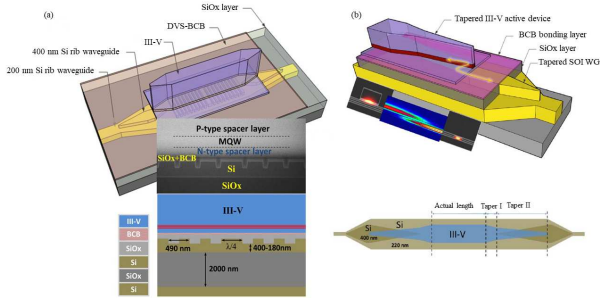

Figure 1.15: Schematic illustration of the III-V-on-Si DFB laser realized by adhesive bonding.(a) Three-dimensional view of the III-V-on-Si DFB laser as well as the longitudinal cross sections of the schematic and the SEM image of the fabricated device. (b) Using a long spot-size converter to couple the light from the III-V active region to the Si waveguide underneath [51].

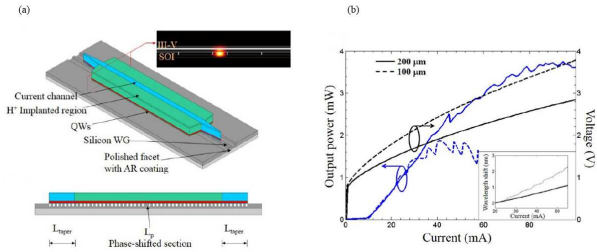

Figure 1.16: Illustration of the heterogeneously integrated DFB laser. (a) Simple scematic of a fabricated laser as well as the lateral view presenting the DFB grating. (b) L-I and I-V curves of a 200 μm (solid line) and 100 μm (dash line) hybrid DFB lasers with quarter phase-shifted sections [54]

III-V active region with both direct and electroabsorption modulation approaches.

Low-threshold short-cavity III-V-on-Si DFB lasers fabricated with a low temperature molecular bonding process have been reported in [54, 55]. In Figure 1.16(a) the schematic of the heterogeneously integrated DFB laser from [54] is shown. The devices have been fabricated with a III-V epitaxial stack and a 500 nm thick silicon layer on top of a 1 μm thick buried oxide (BOX) layer. The fundamental TE mode is designed to be equally confined to the silicon and III-V waveguides with a confinement factor of 5.6% in the III-V active region. A 90 nm deep first-order surface grating is also defined in the silicon underneath to define the laser cavity with two different lengths of 100 μm and 200 μm. In order to suppress higher order modes in this design, the III-V mesa is designed to be 24 μm wide, in which a 4 μm wide current channel has been defined by proton implantation. Wall-plug efficiencies up to 3% and 2% were achieved at 1 mW output power for the 100 μm and 200 μm long lasers, respectively [14]. Similar work [15] demonstrated other improvements on III-V-on-silicon C-band DFB lasers.

Heterogeneously integrated DFB lasers operating in the O-band were demonstrated by Intel in [56]. Lasing is reported up to 150 °C and a wall-plug efficiency of 15% is achieved at 80 °C. However, direct modulation has not been demonstrated with these devices. To achieve a short cavity length with a large confinement factor in the active region, a combination of direct bonding and epitaxial regrowth has been applied for fabricating membrane lasers on a SiO_2/Si substrate [57]. High performance either in terms of power consumption or modulation bandwidth has been achieved, but at the expense of more complex fabrication [58, 59].

1.4.2 Distributed Bragg Reflector lasers

Distributed Bragg Reflector (DBR) lasers are another type of single mode lasers which offer more potential for laser performance engineering compared to DFB lasers. DBR lasers have the potential to use an ultra-long external cavity that can be implemented in a low-loss silicon photonics platform.
As shown in Figure 1.17, an extended III-V-on-Si DBR laser with 1 kHz linewidth and over 37 mW output power, as well as a ring-assisted III-V-on-Si DBR laser with a linewidth less than 500 Hz have been demonstrated [60]. A 15 mm long, low-kappa Bragg reflector defined in the ultra low-loss silicon waveguide helps reducing the laser linewidth while providing high output power and single-mode operation. High-Q ring resonators in the laser cavity can further reduce the laser linewidth by enhancing the cavity length near resonance and sharpening the cavity filter. In [61], high-performance lasers on SiN with tens of milliwatts output power through the SiN waveguide are demonstrated. A sub-kHz fundamental linewidth as well as a relative intensity noise (RIN) below -150 dB/Hz up to 20 GHz have been reported.

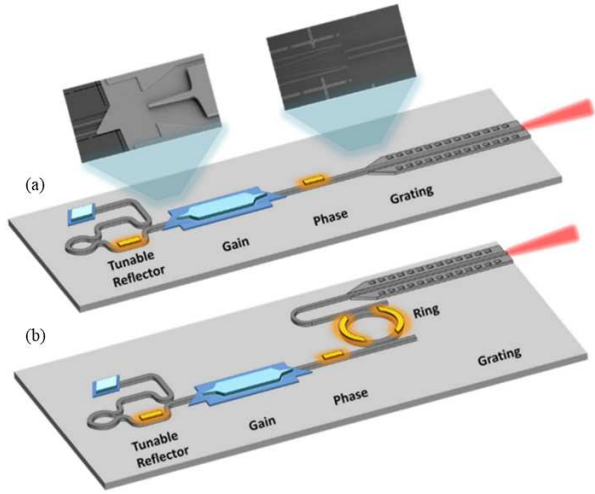

Figure 1.17: Schematic of the Extended DBR laser, with SEM images of the transitions between the various sections of the laser. (b) A ring resonator is incorporated in the cavity to further improve the low noise performance of the laser [60].

1.4.3 Widely tunable lasers

A heterogeneously integrated III-V-on-Si laser with a tuning range of 8 nm was reported in [62]. The device was fabricated by integration of a III-V gain section, a silicon ring resonator for wavelength selection as well as two silicon Bragg grating reflectors as back and front mirrors. A SMSR higher than 45 dB and an output power up to 10 mW were achieved at 20 °C. The measured laser linewidth was reported to be 1.7 MHz. [63] reported a 40 nm tuning range (from 1560 nm to 1600 nm) using the Vernier effect between two ring resonators incorporated in the ring laser cavity. Lower than 1 MHz intrinsic linewidth is achieved, which can be decreased to 550 kHz in the optimum operation point.

Figure 1.18 represents a C-band optical transmitter with an integrated widely-tunable III-V-on-Si laser on the IMEC iSiPP50G platform realized by micro-transfer printing [64]. The threshold current is around 100 mA and an on-chip optical power of 2 mW at a bias current of 130 mA is achieved. By driving both heaters of the ring resonator Vernier filter and the phase section simultaneously, the wavelength can be finely tuned to obtain a 40 nm tuning range. [65] demonstrated widely-tunable narrow-linewidth semiconductor lasers using a ring-resonator based mirror as the extended cavity. The lasers operate within an ultra-wide wavelength tuning range of 110 nm, containing three optical communication bands (S+C+L). The total footprint of the device is smaller than 0.81 mm^2 and the measured intrinsic linewidth is around 220 Hz.

1.5 Research objectives

This PhD thesis focuses on the realization of heterogeneously integrated III-V-on-Silicon C-band DFB lasers via adhesive bonding. Due to a single frequency

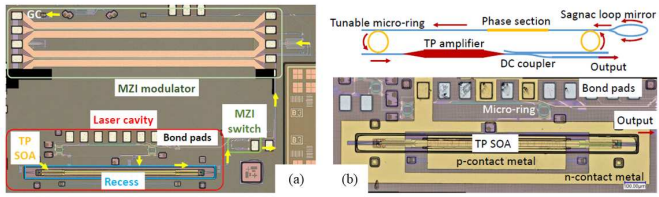

Figure 1.18: A widely tunable III-V-on-Si laser. (a) Schematic layout of the laser cavity.(b) Microscope image of the fabricated device realized by transfer-printing technique on the imec iSiPP50G platform [64].

emission, a DFB laser diode is a good candidate for the required light source in optical communication applications. For data center links and other optical interconnects it is very important to have low power consumption and still have sufficient optical output power. This implies then that the laser should have good efficiency (slope efficiency in mW/mA and wall-plug efficiency) and low threshold current. Commercial DFB lasers based on a monolithic InP substrate are available for fiber optics communication with an output power larger than 10 mW as well as a threshold current between 10 and 20 mA [66]. High power, long cavity commercial DFB lasers with wall-plug efficiencies up to 40% and threshold currents of around 50 mA are available [67]. However, to achieve such a high wall-plug efficiency, these lasers need to be biased up to several hundreds of mA resulting in a high power consumption. In this thesis, we look specifically at lasers on silicon, because such lasers can be readily integrated with other silicon photonic components, and heterogeneously integrated III-V-on-Si lasers have so far not been realized with good wall-plug efficiency and low power consumption. So, the main goal of this work is to achieve a high wall-plug efficiency at a rather low current (e.g., below 50 mA). We aim to improve the wall-plug efficiency of C-band DFB lasers on silicon with several percent to over 10%. Additionally, we aimed to get a relatively high modulation bandwidth, with rather low intensity noise and linewidth.

1.6 Outline of the thesis

This thesis includes five chapters, of which the content is summarized below. In Chapter 2 the theory of the DFB laser diodes is discussed. Two well-known models in analyzing the behavior of the DFB lasers are discussed. In order to study the behavior of the propagating forward and backward waves inside the cavity, the coupled mode theory is explained and some useful relations are derived. Then, the rate equations model is presented to investigate the time evolution of the carrier density and photon density inside the cavity. Based on the rate equations model, the threshold analysis as well as the above threshold behavior are investigated. In addition, the small signal and the large signal behavior of laser diodes, followed by the noise characteristics are given using the rate equations model.
In chapter 3, we first give an overview of the heterogeneously integrated III-V-on-Si DFB lasers, which were fabricated in UGent-IMEC Photonics Research Group (PRG). We discuss the issues concerning the design of these structures and present some experimental results to characterize these lasers for further optimization. Then, the motivation of this thesis on achieving small footprint integrated DFB lasers are discussed by presenting some ideas for further optimization of the integrated DFB lasers. Subsequently, a standard process flow of a III-V epitaxial layer is given.
Chapter 4 contains the theoretical and experimental knowledge presented in previ-

ous chapters to demonstrate high efficiency, short cavity III-V-on-Si DFB lasers. First, we describe the experimental results of heterogeneously integrated DFB lasers realized by adhesive bonding with symmetric output waveguide. The static characterization of a 200 μm long DFB laser depicts above 12 % wall-plug efficiency at 25 °C with a threshold current of around 10.5 mA. In addition, 20 Gbps NRZ-OOK direct modulation and transmission over a 2 km long single mode fiber are successfully demonstrated. Next, we demonstrate more efficient III-V-on-Si DFB lasers by further optimizing the short cavity lasers with a single output waveguide. The devices not only show higher wall-plug efficiency, but also exhibit a very low noise performance in terms of having a low relative intensity noise (RIN) and a low spectral linewidth.
Finally, the conclusions of this work are given in Chapter 5 followed by a short discussion of the future prospects.

1.7 Publications

This dissertation has led to the following list of publications in conferences and international peer-reviewed journals.

1.7.1 Publications in international journals

1. **J. Rahimi**, N. Singh, J. Van Kerrebrouck, J. Bauwelinck, G. Roelkens, and G. Morthier, "High wall-plug efficiency and narrow linewidth1 III-V-on-silicon C-band DFB laser diodes", *Optics Express*, vol. 30, no. 15, pp. 27983–27992, 2022.

2. **J. Rahimi**, J. Van Kerrebrouck, B. Haq, J. Bauwelinck, G. Roelkens, and G. Morthier, "Demonstration of a High-Efficiency Short-Cavity III-V-on-Si C-Band DFB Laser Diode", *IEEE Journal of Selected Topics in Quantum Electronics*, vol. 28, no. 3, pp. 797–804, 2021.

3. B. Haq, **J. Rahimi**, J. Zhang, A. Gocalinska, E. Pelucchi, B. Corbett, and G. Roelkens, "Micro-transfer-printed III-V-on-silicon C-band distributed feedback lasers", *Optics Express*, vol. 28, no. 22, pp. 32793–32801, 2020.

4. M. Shahin, **J. Rahimi**, J. Van Kerrebrouck, P. Ossieur, X. Yin, J. Bauwelinck, G. Roelkens, and G. Morthier, "80-Gbps NRZ-OOK electro-absorption modulation of InP-on-Si DFB laser diodes", *IEEE Photonics Technology Letters*, vol. 31, no. 7, pp. 533–536, 2019.

1.7.2 Publications at international conferences

1. **J. Rahimi**, N. Singh, J. Van Kerrebrouck, J. Bauwelinck, G. Roelkens, and G. Morthier, "High Wall-plug-efficiency III-V-on-silicon C-band DFB Laser Diodes", *OECC/PSC* , Japan, 2022.

2. **J. Rahimi**, J. Van Kerrebrouck, B. Haq, J. Bauwelinck, G. Roelkens, and G. Morthier, "High-efficiency short-cavity III-V-on-Si C-band DFB laser diodes", *Silicon Photonics XVII (SPIE)*, vol. 12006, pp. 118–122, 2022.

3. **J. Rahimi**, M. Shahin, K. Van Gasse, G. Roelkens, and G. Morthier, "Characterization of optical loss and carrier lifetime in integrated III-V/SOI distributed feedback lasers", *Annual Symposium of the IEEE Photonics Society Benelux Chapter*, Netherlands, 2019.

4. G. Morthier, M. Shahin, **J. Rahimi**, P. Ossieur, X. Yin, J. Bauwelinck, and G. Roelkens, "Towards high-speed InP-on-silicon DFB lasers with low power consumption", *International conference on optics and electro-optics*, India, 2019.

5. M. Shahin, **J. Rahimi**, J. Van Kerrebrouck, A. Abbasi, K. Van Gasse, M. Muneeb, L. Breyne, P. Ossieur, X. Yin, J. Bauwelinck, G. Roelkens, and G. Morthier, "Demonstration of 80 Gbps NRZ-OOK Electro-Absorption Modulation of InP-on-Si DFB Laser Diodes", *CLEO: Science and Innovations*, 2019.

Bibliography

[1] R. Kerdock and D. Wolaver, "Atlanta fiber system experiment: results of the atlanta experiment," *Bell System Technical Journal*, vol. 57, no. 6, pp. 1857–1879, 1978.

[2] B. J. Puttnam, R. Luís, W. Klaus, J. Sakaguchi, J.-M. D. Mendinueta, Y. Awaji, N. Wada, Y. Tamura, T. Hayashi, M. Hirano, *et al.*, "2.15 Pb/s transmission using a 22 core homogeneous single-mode multi-core fiber and wideband optical comb," in *2015 European Conference on Optical Communication (ECOC)*, pp. 1–3, IEEE, 2015.

[3] G. P. Agrawal, *Fiber-optic communication systems*, vol. 222. John Wiley & Sons, 2012.

[4] D. Liang and J. E. Bowers, "Recent progress in lasers on silicon," *Nature photonics*, vol. 4, no. 8, pp. 511–517, 2010.

[5] A. Y. Liu and J. Bowers, "Photonic integration with epitaxial III-V on silicon," *IEEE Journal of Selected Topics in Quantum Electronics*, vol. 24, no. 6, pp. 1–12, 2018.

[6] "Silicon photonics and photonic integrated circuits: Technology, industry and market trends," *Technical report*, 2019.

[7] C. A. Thraskias, E. N. Lallas, N. Neumann, L. Schares, B. J. Offrein, R. Henker, D. Plettemeier, F. Ellinger, J. Leuthold, and I. Tomkos, "Survey of photonic and plasmonic interconnect technologies for intra-datacenter and high-performance computing communications," *IEEE Communications Surveys & Tutorials*, vol. 20, no. 4, pp. 2758–2783, 2018.

[8] H. Mekawey, M. Elsayed, Y. Ismail, and M. A. Swillam, "Optical interconnects finally seeing the light in silicon photonics: Past the hype," *Nanomaterials*, vol. 12, no. 3, p. 485, 2022.

[9] S. Lischke, A. Peczek, J. Morgan, K. Sun, D. Steckler, Y. Yamamoto, F. Korndörfer, C. Mai, S. Marschmeyer, M. Fraschke, *et al.*, "Ultra-fast germanium

photodiode with 3-dB bandwidth of 265 GHz," *Nature Photonics*, vol. 15, no. 12, pp. 925–931, 2021.

[10] A. Rahim, J. Goyvaerts, B. Szelag, J.-M. Fedeli, P. Absil, T. Aalto, M. Harjanne, C. Littlejohns, G. Reed, G. Winzer, *et al.*, "Open-access silicon photonics platforms in europe," *IEEE Journal of Selected Topics in Quantum Electronics*, vol. 25, no. 5, pp. 1–18, 2019.

[11] P.-I. Dietrich, M. Blaicher, I. Reuter, M. Billah, T. Hoose, A. Hofmann, C. Caer, R. Dangel, B. Offrein, U. Troppenz, *et al.*, "In situ 3D nanoprinting of free-form coupling elements for hybrid photonic integration," *Nature Photonics*, vol. 12, no. 4, pp. 241–247, 2018.

[12] N. Lindenmann, S. Dottermusch, M. L. Goedecke, T. Hoose, M. R. Billah, T. P. Onanuga, A. Hofmann, W. Freude, and C. Koos, "Connecting silicon photonic circuits to multicore fibers by photonic wire bonding," *Journal of lightwave Technology*, vol. 33, no. 4, pp. 755–760, 2014.

[13] M. R. Billah, M. Blaicher, T. Hoose, P.-I. Dietrich, P. Marin-Palomo, N. Lindenmann, A. Nesic, A. Hofmann, U. Troppenz, M. Moehrle, *et al.*, "Hybrid integration of silicon photonics circuits and InP lasers by photonic wire bonding," *Optica*, vol. 5, no. 7, pp. 876–883, 2018.

[14] M. Deubel, G. Von Freymann, M. Wegener, S. Pereira, K. Busch, and C. M. Soukoulis, "Direct laser writing of three-dimensional photonic-crystal templates for telecommunications," *Nature materials*, vol. 3, no. 7, pp. 444–447, 2004.

[15] R. Marchetti, C. Lacava, L. Carroll, K. Gradkowski, and P. Minzioni, "Coupling strategies for silicon photonics integrated chips," *Photonics Research*, vol. 7, no. 2, pp. 201–239, 2019.

[16] J. P. Epping, R. M. Oldenbeuving, D. Geskus, I. Visscher, R. Grootjans, C. G. Roeloffzen, and R. G. Heideman, "High power, tunable, narrow linewidth dual gain hybrid laser," in *Advanced Solid State Lasers*, pp. ATu1A–4, Optical Society of America, 2019.

[17] E. Vissers, S. Poelman, C. O. de Beeck, K. Van Gasse, and B. Kuyken, "Hybrid integrated mode-locked laser diodes with a silicon nitride extended cavity," *Optics Express*, vol. 29, no. 10, pp. 15013–15022, 2021.

[18] Z. Zhang and C. Wong, "Recent advances in flip-chip underfill: materials, process, and reliability," *IEEE transactions on advanced packaging*, vol. 27, no. 3, pp. 515–524, 2004.

[19] D. Pedder, "Flip chip solder bonding for microelectronic applications," *Microelectronics International*, 1988.

[20] T. Matsumoto, T. Kurahashi, R. Konoike, K. Suzuki, K. Tanizawa, A. Uetake, K. Takabayashi, K. Ikeda, H. Kawashima, S. Akiyama, *et al.*, "Hybrid-integration of SOA on silicon photonics platform based on flip-chip bonding," *Journal of Lightwave Technology*, vol. 37, no. 2, pp. 307–313, 2018.

[21] T. Matsumoto, T. Kurahashi, K. Tanizawa, K. Suzuki, A. Uetake, K. Takabayashi, K. Ikeda, H. Kawashima, and S. Akiyama, "In-line optical amplification for Si waveguides on 1×8 splitter and selector by flip-chip bonded InP-SOAs," in *2016 Optical Fiber Communications Conference and Exhibition (OFC)*, pp. 1–3, IEEE, 2016.

[22] R. Konoike, K. Suzuki, T. Inoue, T. Matsumoto, T. Kurahashi, A. Uetake, K. Takabayashi, S. Akiyama, S. Sekiguchi, S. Namiki, *et al.*, "SOA-integrated silicon photonics switch and its lossless multistage transmission of high-capacity WDM signals," *Journal of lightwave technology*, vol. 37, no. 1, pp. 123–130, 2018.

[23] D. Liang and J. E. Bowers, "Recent progress in heterogeneous III-V-on-silicon photonic integration," *Light: Advanced Manufacturing*, vol. 2, no. 1, pp. 59–83, 2021.

[24] U. Gösele, Y. Bluhm, G. Kästner, P. Kopperschmidt, G. Kräuter, R. Scholz, A. Schumacher, S. Senz, Q.-Y. Tong, L.-J. Huang, *et al.*, "Fundamental issues in wafer bonding," *Journal of Vacuum Science & Technology A: Vacuum, Surfaces, and Films*, vol. 17, no. 4, pp. 1145–1152, 1999.

[25] Q.-Y. Tong, Q. Gan, G. Hudson, G. Fountain, and P. Enquist, "Low temperature InP/Si wafer bonding," *Applied physics letters*, vol. 84, no. 5, pp. 732–734, 2004.

[26] D. Pasquariello and K. Hjort, "Plasma-assisted InP-to-Si low temperature wafer bonding," *IEEE Journal of Selected Topics in Quantum Electronics*, vol. 8, no. 1, pp. 118–131, 2002.

[27] D. Li, Z. Shang, Y. She, and Z. Wen, "Investigation of Au/Si eutectic wafer bonding for MEMS accelerometers," *Micromachines*, vol. 8, no. 5, p. 158, 2017.

[28] F. Niklaus, H. Andersson, P. Enoksson, and G. Stemme, "Low temperature full wafer adhesive bonding of structured wafers," *Sensors and Actuators A: Physical*, vol. 92, no. 1-3, pp. 235–241, 2001.

[29] I. Christiaens, G. Roelkens, K. De Mesel, D. Van Thourhout, and R. Baets, "Thin-film devices fabricated with Benzocyclobutene adhesive wafer bonding," *Journal of Lightwave Technology*, vol. 23, no. 2, p. 517, 2005.

[30] G. Roelkens, J. Brouckaert, D. Van Thourhout, R. Baets, R. Nötzel, and M. Smit, "Adhesive bonding of InP/ InGaAsP dies to processed silicon-on-insulator wafers using DVS-bis-Benzocyclobutene," *Journal of the Electrochemical Society*, vol. 153, no. 12, p. G1015, 2006.

[31] M. A. Meitl, Z.-T. Zhu, V. Kumar, K. J. Lee, X. Feng, Y. Y. Huang, I. Adesida, R. G. Nuzzo, and J. A. Rogers, "Transfer printing by kinetic control of adhesion to an elastomeric stamp," *Nature materials*, vol. 5, no. 1, pp. 33–38, 2006.

[32] X. Feng, M. A. Meitl, A. M. Bowen, Y. Huang, R. G. Nuzzo, and J. A. Rogers, "Competing fracture in kinetically controlled transfer printing," *Langmuir*, vol. 23, no. 25, pp. 12555–12560, 2007.

[33] C. Linghu, S. Zhang, C. Wang, and J. Song, "Transfer printing techniques for flexible and stretchable inorganic electronics," *npj Flexible Electronics*, vol. 2, no. 1, pp. 1–14, 2018.

[34] B. Corbett, R. Loi, J. O'Callaghan, and G. Roelkens, "Transfer printing for silicon photonics," in *Semiconductors and Semimetals*, vol. 99, pp. 43–70, Elsevier, 2018.

[35] Y. Shi, *GaAs nano-ridge lasers epitaxially grown on silicon*. PhD thesis, Ghent University, 2020.

[36] Y. Wan, J. Norman, Q. Li, M. Kennedy, D. Liang, C. Zhang, D. Huang, Z. Zhang, A. Y. Liu, A. Torres, *et al.*, "1.3 μm submilliamp threshold quantum dot micro-lasers on Si," *Optica*, vol. 4, no. 8, pp. 940–944, 2017.

[37] Y. Shi, Z. Wang, J. Van Campenhout, M. Pantouvaki, W. Guo, B. Kunert, and D. Van Thourhout, "Optical pumped InGaAs/GaAs nano-ridge laser epitaxially grown on a standard 300-mm Si wafer," *Optica*, vol. 4, no. 12, pp. 1468–1473, 2017.

[38] T. Soga, S. Hattori, S. Sakai, M. Takeyasu, and M. Umeno, "Characterization of epitaxially grown GaAs on Si substrates with III-V compounds intermediate layers by metalorganic chemical vapor deposition," *Journal of applied physics*, vol. 57, no. 10, pp. 4578–4582, 1985.

[39] J. Carlin, S. Ringel, E. Fitzgerald, M. Bulsara, and B. Keyes, "Impact of GaAs buffer thickness on electronic quality of GaAs grown on graded Ge/GeSi/Si substrates," *Applied Physics Letters*, vol. 76, no. 14, pp. 1884–1886, 2000.

[40] S. Chen, W. Li, J. Wu, Q. Jiang, M. Tang, S. Shutts, S. N. Elliott, A. Sobiesierski, A. J. Seeds, I. Ross, *et al.*, "Electrically pumped continuous-wave III-V quantum dot lasers on silicon," *Nature Photonics*, vol. 10, no. 5, pp. 307–311, 2016.

[41] J. Kwoen, B. Jang, J. Lee, T. Kageyama, K. Watanabe, and Y. Arakawa, "All MBE grown InAs/GaAs quantum dot lasers on on-axis Si (001)," *Optics express*, vol. 26, no. 9, pp. 11568–11576, 2018.

[42] D. Jung, J. Norman, M. Kennedy, C. Shang, B. Shin, Y. Wan, A. C. Gossard, and J. E. Bowers, "High efficiency low threshold current 1.3 μ m InAs quantum dot lasers on on-axis (001) GaP/Si," *Applied Physics Letters*, vol. 111, no. 12, p. 122107, 2017.

[43] C. Shang, E. Hughes, Y. Wan, M. Dumont, R. Koscica, J. Selvidge, R. Herrick, A. C. Gossard, K. Mukherjee, and J. E. Bowers, "High-temperature reliable quantum-dot lasers on si with misfit and threading dislocation filters," *Optica*, vol. 8, no. 5, pp. 749–754, 2021.

[44] Y. Wan, C. Shang, J. Norman, B. Shi, Q. Li, N. Collins, M. Dumont, K. M. Lau, A. C. Gossard, and J. E. Bowers, "Low threshold quantum dot lasers directly grown on unpatterned quasi-nominal (001) si," *IEEE Journal of Selected Topics in Quantum Electronics*, vol. 26, no. 2, pp. 1–9, 2020.

[45] Y. Han, W. K. Ng, C. Ma, Q. Li, S. Zhu, C. C. Chan, K. W. Ng, S. Lennon, R. A. Taylor, K. S. Wong, *et al.*, "Room-temperature InP/InGaAs nano-ridge lasers grown on Si and emitting at telecom bands," *Optica*, vol. 5, no. 8, pp. 918–923, 2018.

[46] Y. Hu, D. Liang, K. Mukherjee, Y. Li, C. Zhang, G. Kurczveil, X. Huang, and R. G. Beausoleil, "III/V-on-Si MQW lasers by using a novel photonic integration method of regrowth on a bonding template," *Light: Science & Applications*, vol. 8, no. 1, pp. 1–9, 2019.

[47] T. Hiraki, T. Aihara, T. Fujii, K. Takeda, T. Kakitsuka, T. Tsuchizawa, and S. Matsuo, "Integrated DFB laser diode and high-efficiency mach-zehnder modulator using membrane III-V semiconductors on Si photonics platform," in *2019 IEEE International Electron Devices Meeting (IEDM)*, pp. 33–4, IEEE, 2019.

[48] D. Liang and J. E. Bowers, "Recent progress in heterogeneous III-V-on-silicon photonic integration," *Light: Advanced Manufacturing*, vol. 2, no. 1, pp. 59–83, 2021.

[49] D. J. Blumenthal, "Photonic integration for UV to IR applications," *APL Photonics*, vol. 5, no. 2, p. 020903, 2020.

[50] A. Malik, C. Xiang, L. Chang, W. Jin, J. Guo, M. Tran, and J. Bowers, "Low noise, tunable silicon photonic lasers," *Applied Physics Reviews*, vol. 8, no. 3, p. 031306, 2021.

[51] S. Keyvaninia, S. Verstuyft, L. Van Landschoot, F. Lelarge, G.-H. Duan, S. Messaoudene, J. Fedeli, T. De Vries, B. Smalbrugge, E. Geluk, *et al.*, "Heterogeneously integrated III-V/silicon distributed feedback lasers," *Optics letters*, vol. 38, no. 24, pp. 5434–5437, 2013.

[52] A. Abbasi, B. Moeneclaey, J. Verbist, X. Yin, J. Bauwelinck, G.-H. Duan, G. Roelkens, and G. Morthier, "Direct and electroabsorption modulation of a III–V-on-silicon DFB laser at 56 gb/s," *IEEE Journal of Selected Topics in Quantum Electronics*, vol. 23, no. 6, pp. 1–7, 2017.

[53] M. Shahin, J. R. Vaskasi, J. Van Kerrebrouck, P. Ossieur, X. Yin, J. Bauwelinck, G. Roelkens, and G. Morthier, "80-Gbps NRZ-OOK electroabsorption modulation of InP-on-Si DFB laser diodes," *IEEE Photonics Technology Letters*, vol. 31, no. 7, pp. 533–536, 2019.

[54] C. Zhang, S. Srinivasan, Y. Tang, M. J. Heck, M. L. Davenport, and J. E. Bowers, "Low threshold and high speed short cavity distributed feedback hybrid silicon lasers," *Optics express*, vol. 22, no. 9, pp. 10202–10209, 2014.

[55] C. Zhang, S. Zhang, J. D. Peters, and J. E. Bowers, "8$\times$ 8$\times$ 40 Gbps fully integrated silicon photonic network on chip," *Optica*, vol. 3, no. 7, pp. 785–786, 2016.

[56] R. Jones, P. Doussiere, J. B. Driscoll, W. Lin, H. Yu, Y. Akulova, T. Komljenovic, and J. E. Bowers, "Heterogeneously integrated InP/silicon photonics: fabricating fully functional transceivers," *IEEE Nanotechnology Magazine*, vol. 13, no. 2, pp. 17–26, 2019.

[57] S. Matsuo, T. Fujii, K. Hasebe, K. Takeda, T. Sato, and T. Kakitsuka, "Directly modulated buried heterostructure DFB laser on SiO_2/Si substrate fabricated by regrowth of InP using bonded active layer," *Optics express*, vol. 22, no. 10, pp. 12139–12147, 2014.

[58] S. Yamaoka, N.-P. Diamantopoulos, H. Nishi, R. Nakao, T. Fujii, K. Takeda, T. Hiraki, T. Tsurugaya, S. Kanazawa, H. Tanobe, *et al.*, "Directly modulated membrane lasers with 108 GHz bandwidth on a high-thermal-conductivity silicon carbide substrate," *Nature Photonics*, vol. 15, no. 1, pp. 28–35, 2021.

[59] N.-P. P. Diamantopoulos, S. Yamaoka, T. Fujii, H. Nishi, K. Takeda, T. Tsuchizawa, T. Kakitsuka, and S. Matsuo, "47.5 GHz Membrane-III-V-on-Si Directly Modulated Laser for Sub-pJ/bit 100-Gbps Transmission," in *Photonics*, vol. 8, p. 31, Multidisciplinary Digital Publishing Institute, 2021.

[60] D. Huang, M. A. Tran, J. Guo, J. Peters, T. Komljenovic, A. Malik, P. A. Morton, and J. E. Bowers, "High-power sub-kHz linewidth lasers fully integrated on silicon," *Optica*, vol. 6, no. 6, pp. 745–752, 2019.

[61] C. Xiang, J. Guo, W. Jin, L. Wu, J. Peters, W. Xie, L. Chang, B. Shen, H. Wang, Q.-F. Yang, *et al.*, "High-performance lasers for fully integrated silicon nitride photonics," *Nature communications*, vol. 12, no. 1, pp. 1–8, 2021.

[62] S. Keyvaninia, G. Roelkens, D. Van Thourhout, C. Jany, M. Lamponi, A. Le Liepvre, F. Lelarge, D. Make, G.-H. Duan, D. Bordel, *et al.*, "Demonstration of a heterogeneously integrated III-V/SOI single wavelength tunable laser," *Optics express*, vol. 21, no. 3, pp. 3784–3792, 2013.

[63] J. Zhang, Y. Li, S. Dhoore, G. Morthier, and G. Roelkens, "Unidirectional, widely-tunable and narrow-linewidth heterogeneously integrated III-V-on-silicon laser," *Optics Express*, vol. 25, no. 6, pp. 7092–7100, 2017.

[64] J. Zhang, E. Soltanian, B. Haq, S. Ertl, J. Rimböck, B. Matuskova, E. Pelucchi, A. Gocalinska, J. Van Campenhout, G. Lepage, *et al.*, "Integrated optical transmitter with micro-transfer-printed widely tunable III-V-on-Si laser," in *Optical Fiber Communication Conference*, pp. Tu2D–2, Optica Publishing Group, 2022.

[65] M. A. Tran, D. Huang, J. Guo, T. Komljenovic, P. A. Morton, and J. E. Bowers, "Ring-resonator based widely-tunable narrow-linewidth Si/InP integrated lasers," *IEEE Journal of Selected Topics in Quantum Electronics*, vol. 26, no. 2, pp. 1–14, 2019.

[66] "https://www.sacher-laser.com."

[67] "https://www.sintec.sg/lasers/443.html."

2

Theory of distributed feedback laser diodes

In this chapter, some fundamental concepts of semiconductor diode lasers with a focus on DFB lasers are covered.

2.1 Introduction 2-2

2.2 Coupled mode theory 2-3

2.3 Rate equations model 2-10

2.3.1 Threshold analysis 2-11

2.3.2 Above threshold characteristics 2-11

2.3.3 Small signal characteristics 2-13

2.3.4 Large signal characteristics 2-15

2.3.5 Noise characteristics of laser diodes 2-17

2.4 Wall-plug and differential efficiencies 2-22

2.5 Linewidth of laser diodes with distant reflections 2-23

2.6 Conclusion 2-26

2.1 Introduction

Semiconductor diode lasers are a key component of optical-fiber communication networks. Their capability of being directly modulated along with the development of optical fibers has resulted in an extensive development of the optical fiber communication. The first generation of semiconductor diode lasers were demonstrated in 1962 by forward biasing a simple p-n junction using crystalline blocks of GaAs or $GaAs_{1-x}P_x$ [1–3]. In these early demonstrations, two parallel facets were made to provide an optical feedback and form the laser cavity. However, high threshold current densities limited the performance of these diode lasers to the use of pulsed current sources as well as a cooled operation much below room temperature. These issues were overcome by the invention of the double heterojunction (DH) lasers where the lower bandgap GaAs material was sandwiched between two larger bandgap $Ga_xAl_{1-x}As$ layers (as shown in Figure 2.1(a)). Figure 2.1(b) depicts the energy diagram of the conduction and valence bands of a DH structure where the free electrons and holes simultaneously exist in the middle GaAs layer with a lower bandgap energy. The middle layer, known as the active region, has also a higher refractive index and the DH structure therefore forms an optical waveguide. As a result of the improvements in DH lasers, threshold current densities around 1000 A/cm^2 as well as continuous operation at room temperature were obtained [4, 5].
In the 1980s, 100 Mbit/s data transmission through optical fibers had been achieved using DH Fabry-Perot laser diodes [6]. Although by careful design of the active region dimensions the Fabry-Perot laser can just have a single transverse mode, it still contains several longitudinal modes due to the broadband reflector at the ends of the cavity. This limits the capability of DH Fabry-Perot lasers for the transmission of high-bit-rate data through optical fibers. In order to overcome this

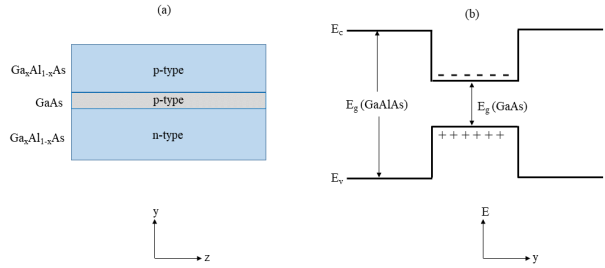

Figure 2.1: a) Illustration of a DH laser diode made by sandwiching a lower bandgap material such as GaAs between two higher bandgap materials such as GaAlAs. b) An energy diagram of the conduction and valence bands versus transverse distance.

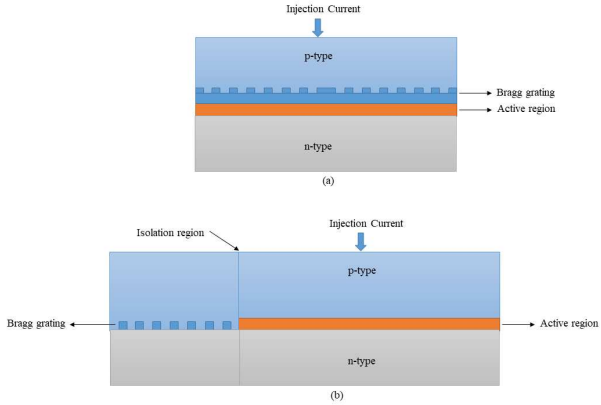

Figure 2.2: Schematic of the single mode laser configurations. a) A distributed feedback semiconductor laser. b) a distributed Bragg reflector semiconductor laser.

limitation, semiconductor lasers with a single longitudinal mode such as DFB and DBR lasers have been demonstrated.

In such lasers, a Bragg grating is present along the light propagation direction. In a DFB laser, as shown in the Figure 2.2(a), the Bragg grating is incorporated along the cavity. In other words, for a DFB laser the Bragg grating or DFB grating determines the cavity length, and it is patterned below or above the active region. For a DBR laser, as depicted in Figure 2.2(b), the Bragg grating is placed outside of the active section of the device. In this thesis, we particularly concentrate on the DFB lasers. In the following sections we briefly discuss the theory of these lasers.

2.2 Coupled mode theory

For a laser containing a Bragg grating, the behavior of the forward and backward propagating waves can be described by the coupled mode theory extracted from Maxwell's equations. By assuming two counter propagating waves alongside the propagation direction z, $F(z,t)$ being the forward component and $R(z,t)$ the backward or reverse component, the total electric field $E(z,t)$ inside the cavity can be written as:

$$E(z,t) = F(z,t)exp(j(\beta_0 z - \omega t)) + R(z,t)exp(j(-\beta_0 z - \omega t)) \qquad (2.1)$$

where β_0 is the propagation constant at Bragg frequency and ω denotes the angular frequency of the propagating field. By using the slowly varying amplitude approximation [7], the counter propagating components $F(z,t)$ and $R(z,t)$ can be derived from Maxwell's equations as follows [6, 8]:

$$\frac{1}{v_g}\frac{\partial F(z,t)}{\partial t} + \frac{\partial F(z,t)}{\partial z} = (g - j\delta)F(z,t) + j\kappa R(z,t) + F_{sp}^{+} \tag{2.2}$$

$$\frac{1}{v_g}\frac{\partial R(z,t)}{\partial t} - \frac{\partial R(z,t)}{\partial z} = (g - j\delta)R(z,t) + j\kappa F(z,t) + F_{sp}^{-} \tag{2.3}$$

here, v_g is the group velocity of the propagating light inside the laser cavity, g describes the net field gain per unit length, κ is the coupling coefficient between the forward and backward electric field components, F_{sp}^{+} and F_{sp}^{-} denote the spontaneous emission which is a zero mean complex Gaussian excitation. In equations 2.2 and 2.3, the deviation from Bragg condition is denoted by δ which can be derived as:

$$\delta = \frac{\omega}{c} n_{eff}(z,t) - \frac{\pi}{\Lambda} \tag{2.4}$$

where c is the speed of light, n_{eff} represents the effective refractive index, and Λ denotes the pitch of the grating.

Equations (2.2) and (2.3) describe the large signal time domain modelling of a DFB laser with a lossless first order grating. Due to the time dependent components as well as the random spontaneous noise terms, solving these equations is challenging. However, for the stationary operation and when neglecting the noise, the coupled wave equations transform to:

$$\frac{dF(z)}{dz} = (g - j\delta)F(z) + j\kappa R(z) \tag{2.5}$$

$$\frac{dR(z)}{dz} = -(g - j\delta)R(z) - j\kappa F(z) \tag{2.6}$$

by applying Pauli matrices σ_i and defining a two-component Van der Waerden notation $\psi = \begin{pmatrix} F \\ R \end{pmatrix}$, the above set of coupled equations can be expressed as [9]:

$$\frac{d\psi(z)}{dz} = H\psi(z) \tag{2.7}$$

where the Hamiltonian operator H is defined as follows:

$$H = j(\delta - jg)\sigma_3 - \kappa\sigma_2 \tag{2.8}$$

in which the complex matrices σ_2 and σ_3 are defined as follow:

$$\sigma_2 = \begin{pmatrix} 0 & -j \\ j & 0 \end{pmatrix} \tag{2.9}$$

$$\sigma_3 = \begin{pmatrix} 1 & 0 \\ 0 & -1 \end{pmatrix} \tag{2.10}$$

In order to find a general solution for the spinor electric fields inside the cavity a vector $\vec{\mu}$ where $H = \vec{\mu} \cdot \vec{\sigma}$ is defined as follows:

$$\vec{\mu} = j(\delta - jg)\hat{x_3} - \kappa\hat{x_2} \tag{2.11}$$

where $\psi(z)$ can be given alongside the laser cavity at two specific positions z_1 and z_2 with the following equation [9]:

$$\psi(z_2) = exp(H(z_2 - z_1))\psi(z_1) \tag{2.12}$$

given by properties of Pauli matrices, $\vec{\mu} \cdot \vec{\mu} = \mu^2 = H^2$. Therefore, the exponential term in equation (2.12) can be written as [9]:

$$exp(H(z_2 - z_1)) = cosh(\mu(z_2 - z_1)) + \frac{\vec{\mu}.\vec{\sigma}}{\mu} sinh(\mu(z_2 - z_1)) \tag{2.13}$$

By assuming the continuity of the electric field and its derivative along the propagation direction (where there is a DFB grating and where there is no DFB grating) and using the proper boundary conditions, some useful relations can be extracted. First, we discuss the case of a uniform DFB grating with non-reflective facets. As shown in Figure 2.3(a), for such a structure, there is no phase shift in the Bragg

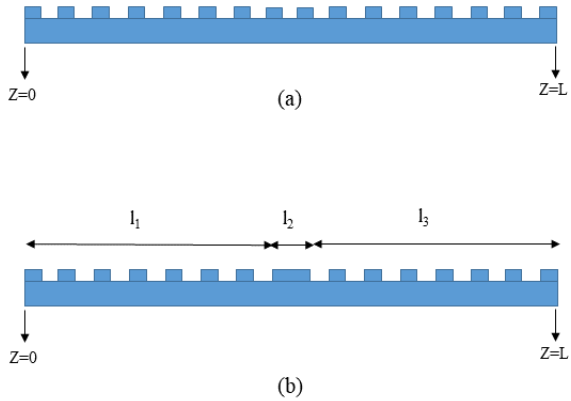

Figure 2.3: Schematics of DFB grating structures with a total length of L. a) A uniform Bragg grating with no phase shift section. b) A Bragg grating with a phase shift defined by the section with a length l_2.

grating. The reflection coefficient of such a system can be defined by dividing the amplitude of the wave propagating backward ψ_R to the amplitude of the wave propagating forward ψ_F. At z = L, the wave function can be written as $\psi(L)$ = $\begin{pmatrix}1\\0\end{pmatrix}$ since for $z > L$ there is no backward component. On the other hand the wave at z = 0 can be found by backward propagation of $\psi(L)$ using (2.12):

$$\psi(0) = exp(-HL)\psi(L) \tag{2.14}$$

Using equations (2.14) and (2.13), the reflection coefficient R is given after some simplifications by the following equation:

$$R = \frac{j\kappa sinh(\mu L)/\mu}{cosh(\mu L) - j((\delta - jg)/\mu)sinh(\mu L)} \tag{2.15}$$

The reflectivity $|R|$ is plotted in Figure 2.4 versus the detuning factor for the κL = 1 at different values of gL. As it is shown, for a uniform DFB grating with non-reflecting facets, there are two longitudinal modes in the cavity with the same gain. The spectral spacing between these to simultaneous modes symmetrically placed at the edges of the gap describes the stop-band of the DFB laser. In order to find a relation for the stop-band of a DFB laser with uniform grating one can calculate the zeros of the reflectivity $|R|$ plotted in Figure 2.4. Given by the equation (2.15), zeros of $|R|$ occur at μL = jnπ (n =1,2,...). From equation (2.15) at g=0 we have:

$$\delta = \pm\sqrt{\kappa^2 + n^2\pi^2/L^2}, n = 1, 2, ... \tag{2.16}$$

The deviation from the Bragg condition can be written as a frequency variation as follows [10]:

$$\delta = n(\omega - \omega_0)/c \tag{2.17}$$

here, n denotes the refractive index of the field propagating inside the cavity, c represents the speed of light, and ω_0 is the Bragg angular frequency. Using $\Delta\nu$ = c $\Delta\lambda/\lambda_B^2$, equation (2.16) for a first order lossless grating can be written as:

$$\Delta\lambda = \frac{\lambda_B^2}{2\pi n_{eff} L}\sqrt{(\kappa L)^2 + \pi^2} \tag{2.18}$$

where $\Delta\lambda$ is the half of the stopband width of the uniform grating DFB laser, λ_B denotes the Bragg wavelength, and $\Delta\nu$ describes the difference between the oscillation frequency and the Bragg frequency ν_0.
As can be seen in Figure 2.4, the reflection coefficient increases by increasing gL, as shown from 0 to 3 in the figure. Theoretically, a dramatic increase to infinity in the reflection coefficient of the system indicates an oscillator. The threshold gain of this system can be obtained by setting the denominator of the equation (2.15) equal to zero. After some simplification, the threshold gain for a DFB laser with a

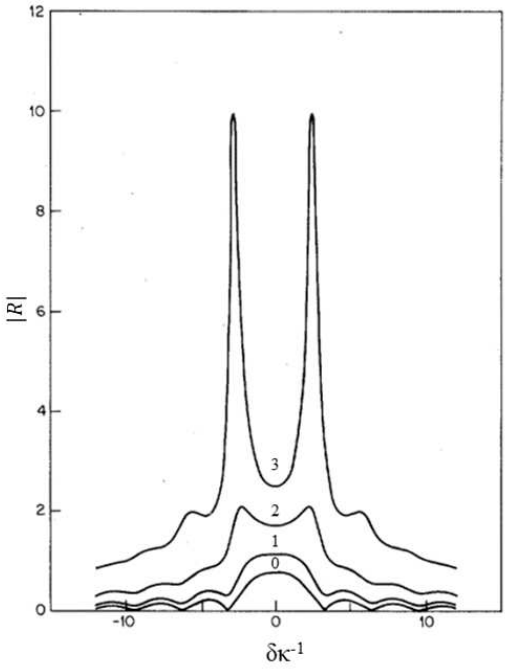

Figure 2.4: Absolute value of the reflectivity value R for the uniform DFB grating given in equation (2.15) versus the deviation from the Bragg condition. The values of gL corresponding to each curve are written on top of the curve for the κL=1 [9].

uniform grating and large κL can be approximated by [9]:

$$g_{th} = 2\pi^2/(\kappa^2 L^3) \tag{2.19}$$

Due to the degeneracy between two oscillating modes, there is no lasing at the Bragg wavelength. In order to have a lasing mode at the Bragg wavelength, the degeneracy of the symmetric modes at the edges of the stopband in the uniform grating has to be broken. There are usually three approaches to achieve this goal. Adding a highly reflective facet at one side of the cavity or using a gain coupling mechanism [10–12] can break the dual mode degeneracy and provide lasing at the Bragg frequency. However, the drawback of these two methods is the difficulty in

controlling the lasing wavelength since it is not predictable which of the modes at the edges of the stopband will lase.

The third and the most common approach is adding a phase shift into the uniform grating to break the dual mode degeneracy. The same approach used in the uniform grating case can be applied to study the behavior of the system with a ϕ= π/2 phase shift in the DFB grating. Here, we consider a phase shift section with a length of l_2 in the middle of the grating structure (as shown in Figure 2.3(b)). Again, assuming a DFB laser with non-reflective facets, we derive a set of equations similar to the uniform grating case. The same hypothesis for $z > L$ where we assumed there is no backward wave component is still valid here since no grating structure is incorporated in that region. However, for the backward propagation of the field the scenario is somehow different due to the perturbation created by the phase shift section in the middle of the grating structure. By determining the wave at z = L as $\psi(L)$, the backward propagation after a length of l_3 (as shown in Figure 2.3(b)) will be $exp(-Hl_3)\ \psi(L)$. Then the small section with the length of l_2 causes a phase shift as $exp(-j\phi\sigma_3)$ and after propagating along the length l_1 (which is similar to the propagation in the section wilt the length of l_3) the field component at z = 0 can be given by [9]:

$$\psi(0) = exp(-Hl_1)exp(-j\phi\sigma_3)exp(-Hl_3)\psi(L) \tag{2.20}$$

By setting ϕ = $\pi/2$ and after some simplifications, the reflection coefficient R is derived as follows:

$$R = \frac{2\kappa(\delta - jg)(sinh(\mu L/2)/\mu)^2}{\frac{\kappa^2}{\mu^2} - \frac{(\delta - jg)^2}{\mu^2}cosh(\mu L) - j((\delta - jg)/\mu)sinh(\mu L)} \tag{2.21}$$

Adding a phase shift of π/2 which corresponds to a $\lambda/4$ shift in the middle of the cavity, introduces a π/2 shift to the phase of each wave passing along this section. A π shift will be added to the round-trip phase of the fields which removes the dual mode degeneracy.

The absolute value of the reflection coefficient defined in the equation (2.21) is plotted in Figure 2.5 for κL = 1 at different values of gL. As it is shown, for a DFB grating with a λ/4 phase shift and non-reflective facets there is a dominant longitudinal mode in the middle of the stopband. Similar to the case of the uniform grating, zeros of $|R|$ can be found by the following relation:

$$\delta = \pm\sqrt{\kappa^2 + 4n^2\pi^2/L^2}, n = 1, 2, ... \tag{2.22}$$

By using δ=$\Delta\omega/v_g$ and $\Delta\nu$ = $c\ \Delta\lambda/\lambda_B^2$, after some simplifications the following relation for a DFB grating with λ/4 phase shift can be derived from equation (2.22) as:

$$\Delta\lambda = \frac{\lambda_B^2}{2\pi n_{eff}L}\sqrt{(\kappa L)^2 + 4\pi^2} \tag{2.23}$$

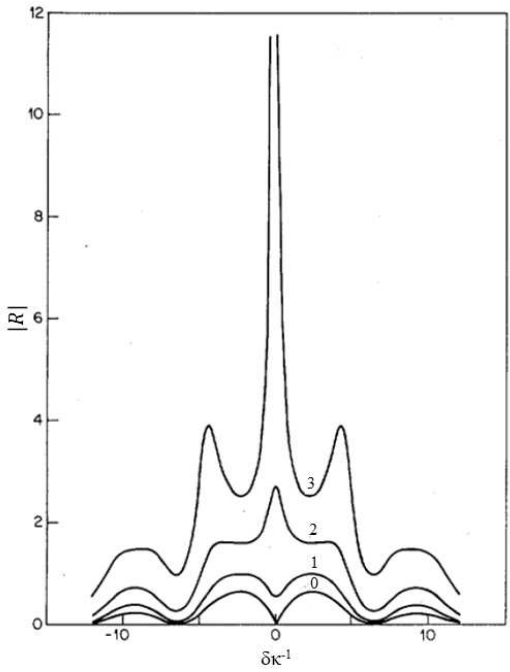

Figure 2.5: Absolute value of the reflectivity R for a DFB grating with $\phi = \pi/2$ phase shift given in equation (2.21) versus the deviation from the Bragg condition for κL=1. The values of gL corresponding to each curve are written on top of the curve [9].

Equation (2.23) describes the spectral width between two zeros of the lossless first order DFB grating with λ/4 phase shift and anti-reflective facets. As can be seen in Figure 2.5, $\Delta\lambda$ in equation (2.23) corresponds to the half of the stopband.
As depicted in Figure 2.5, the reflectivity increases by increasing gL. The threshold gain of the DFB grating with a λ/4 phase shift can be obtained by setting the denominator of the equation (2.21) equal to zero. After some simplifications, the threshold gain for a DFB laser with a λ/4 phase shift and large κL can be approximated as [9]:

$$g_{th} = 4\kappa exp(-\kappa L) \tag{2.24}$$

In the following section we discuss another approach used for analyzing semiconductor lasers.

2.3 Rate equations model

This model is based on the rate equations of carrier and photon densities inside the laser cavity. Depending on the active region, several rate equations might be needed to model the laser behavior. However, for a semiconductor laser with a quantum well (QW) active region, two coupled equations are sufficient to represent the interaction between the carrier density N (number of carriers per active region volume V) and the photon density $N_{p,m}$ (number of photons per cavity volume V_p occupied by photons) for mode m. In contrast to the coupled mode model discussed before, the solution of these coupled rate equations is often explicitly analytic or can be computed rapidly using a straightforward ordinary differential equations solver. In addition, the small-signal approach helps to illustrate the physics of modulation and noise. The variation of the carrier density N and the photon density $N_{p,m}$ is described as follows [13]:

$$\frac{dN}{dt} = \frac{\eta_i I}{qV} - \frac{N}{\tau} - v_g g N_{p,m} \tag{2.25}$$

$$\frac{dN_{p,m}}{dt} = [\Gamma v_g g - \frac{1}{\tau_p}]N_{p,m} + \Gamma R'_{sp} \tag{2.26}$$

In the above equations, I and η_i are the injection current and the injection efficiency, respectively. τ denotes the carrier lifetime and the term $\frac{N}{\tau}$ in the carrier rate equation describes the carrier decay mechanism caused by the spontaneous and nonradiative recombinations as follows [13, 14]:

$$\frac{N}{\tau} = AN + BN^2 + CN^3 \tag{2.27}$$

where nonradiative recombination terms AN and CN^3 describe the surface recombination due to defects and Auger recombination, respectively. BN^2 is a radiative recombination term and counts for the spontaneous emission. The last term in the equation (2.25) denotes the stimulated emission where v_g and g stand for the group velocity and the gain coefficient, respectively. The carrier and photon rate equations are coupled through this stimulated emission term.
Another important parameter appearing in the photon density rate equation is τ_p which describes the photon lifetime in the cavity. It can be written as:

$$\frac{1}{\tau_p} = v_g(\alpha_m + \alpha_i) \tag{2.28}$$

with α_m the distributed mirror loss experienced by the photons of the mode of interest and α_i representing the internal cavity loss. The term $\Gamma R'_{sp}$ in the equation

(2.26) represents the fraction of the spontaneous emission coupled to the mode of interest (R'_{sp} = $\beta_{sp}R_{sp}$, where β_{sp} is the spontaneous emission factor that denotes the percentage of the total spontaneous emission R_{sp}, coupled into the lasing mode). The parameter Γ is the confinement factor of the mode in the active region given by $\frac{V}{V_p}$.

2.3.1 Threshold analysis

At the steady state operation of the device, the time derivatives can be set to zero. Thus, using equations (2.25) and (2.26) we have:

$$I = \frac{qV}{\eta_i}(\frac{N}{\tau} + v_g g(N) N_{p,m}) \tag{2.29}$$

$$N_{p,m} = \frac{\Gamma R'_{sp}(N)}{\frac{1}{\tau_p} - \Gamma v_g g} \tag{2.30}$$

at the threshold point, the laser has no stimulated emission and the whole optical power is generated via the spontaneous emission mechanism. Therefore, the terms related to the stimulated emission can be set to zero. The threshold current of the laser from the equation (2.29) can be found as:

$$I_{th} = \frac{qV}{\eta_i}\frac{N_{th}}{\tau} \tag{2.31}$$

from the equation (2.30) the threshold gain can be written as [13]:

$$\Gamma v_g g_{th} \equiv \frac{1}{\tau_p} \equiv (\alpha_m + \alpha_i) v_g \tag{2.32}$$

where g_{th} =$g(N_{th})$.

2.3.2 Above threshold characteristics

For a laser operating above the threshold point, the carrier density $N(t)$ fluctuates around N_{th}. On the other hand, since the system is in resonance as the small signal gain is equal to the optical loss of the resonator, equation (2.32) is still valid. Using equation (2.32), we can rewrite the steady state equations (2.29) and (2.30) as:

$$I(N) = \frac{qV}{\eta_i}(\frac{N_{th}}{\tau} + v_g g_{th} N_{p,m}) \tag{2.33}$$

$$N_{p,m} = \frac{R'_{sp}(N_{th})/v_g}{g_{th} - g(N)} \tag{2.34}$$

As can be derived from equations (2.33) and (2.34), N and g never exceed N_{th} and g_{th} under a finite injection current level. On the other hand, for bias currents above the threshold, spontaneous emission as well as the nonradiative recombination quantities clamp to their threshold values. Substituting the equation (2.31) into the equation (2.33), the photon density above the threshold can be rewritten as [13]:

$$N_{p,m} = \frac{\eta_i (I - I_{th})}{q v_g g_{th} V} \tag{2.35}$$

The optical energy inside the cavity can be calculated by multiplying N_p by the energy per photon $h\nu$ and the cavity volume V_p. Then the output power can be achieved by multiplying the stored energy in the cavity with the energy loss rate through the distributed mirror loss $v_g \alpha_m$. Using equations (2.32) and (2.35), the optical output power of the laser above threshold can be expressed by [13]:

$$P = \frac{\eta_i \alpha_m}{(\alpha_m + \alpha_i)} \frac{h\nu}{q} (I - I_{th}) \tag{2.36}$$

Equation (2.36) gives the total output power from both facets. By incorporating a highly reflective facet at one side of the cavity, it represents the total output power obtained from the output facet. As can be derived from equation (2.36) and Figure 2.6, the total output power above threshold increases linearly with increasing the injection current while the carrier number and material gain clamp to their threshold value.

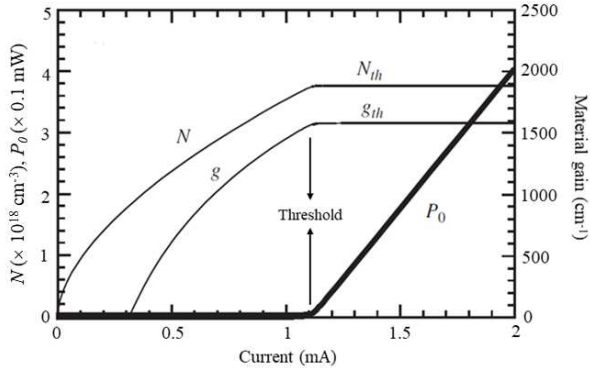

Figure 2.6: Evolution of the optical output power, the carrier number, and the material gain versus injection current for an in-plane semiconductor laser [13].

2.3.3 Small signal characteristics

In this section we discuss the direct modulation performance of a single mode laser diode due to a small perturbation in the injection current. Assuming a single mode laser such as a DFB laser with a side mode suppression ratio (SMSR) larger than 30 dB, we can neglect the effect of other modes in derivations of the related equations [15]. By applying a modulation current $I(t) = I_0 + I_1 e^{j\omega t}$ to the laser, where I_1 is the amplitude of the modulation ($I_1 \ll I_0$) and ω denotes the modulation angular frequency, the time dependent carrier and photon densities can be written as:

$$N(t) = N_0 + Re(N_1 e^{j\omega t}) \tag{2.37}$$

$$N_{p,m}(t) = N_{p,m0} + Re(N_{p,m1} e^{j\omega t}) \tag{2.38}$$

Before proceeding further, we first need to modify the gain term in equations (2.25) and (2.26) since the gain g in general is a function of the carrier density N and the wavelength λ as:

$$g(N, \lambda) = a(\lambda)(N - N_{tr}) \tag{2.39}$$

which can be modulated due to the applied modulation current. In the above equation, $a = dg/dN$ represents the differential gain of the system which is a wavelength dependent parameter, and N_{tr} denotes the carrier density at the transparency. By substituting equation (2.37) in (2.39) we have:

$$g(N, \lambda) = a(\lambda)(N_0 + Re(N_1 e^{j\omega t}) - N_{tr}) = g_{th} + a(\lambda) Re(N_1 e^{j\omega t}) \tag{2.40}$$

where the threshold gain is replaced at the steady state. By substituting equations (2.37), (2.38), and (2-40) in the rate equations (2.25) and (2.26) and collecting the alike terms we have:

$$j\omega N_1 = \frac{\eta_i I_1}{qV} - \frac{N_1}{\tau} - v_g g_{th} N_{p,m1} - a v_g N_1 N_{p,m0} \tag{2.41}$$

$$j\omega N_{p,m1} = \Gamma a v_g N_1 N_{p,m0} \tag{2.42}$$

Using equations (2.41) and (2.42) and by defining $P_{ac} = v_g \alpha_m N_{p,m1} h\nu V_p$, the transfer function $\frac{P_{ac}(\omega)}{I_1(\omega)}$ can be derived as [13]:

$$\frac{P_{ac}(\omega)}{I_1(\omega)} = \frac{\eta_i h\nu}{q} \frac{\alpha_m v_g (v_g a N_{p,m0})}{\frac{v_g a N_{p,m0}}{\tau_p} - \omega^2 + j\omega[v_g a N_{p,m0} + \frac{1}{\tau}]} \tag{2.43}$$

where the natural angular frequency of the system can be derived from the denominator of the above equation as:

$$\omega_R = \sqrt{\frac{v_g a N_{p,m0}}{\tau_p}} = \sqrt{\frac{\Gamma v_g a}{qV} \eta_i (I - I_{th})} \tag{2.44}$$

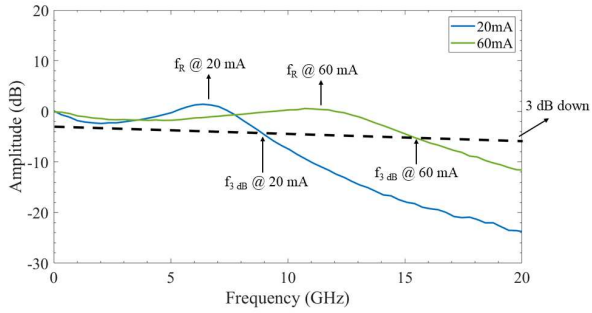

Figure 2.7: Small signal characteristics of a DFB laser at two different injection currents of 20 and 60 mA (two different output power) and positions of relaxation resonance frequency f_R and f_{3dB} on the small signal response.

where for the third expression we replaced $N_{p,m0}$ from the equation (2.35). By increasing the injection current (which is equivalent to the increase in the output power above threshold) the resonance frequency f_R increases as depicted in Figure 2.7 where the small signal response of a DFB laser is plotted at two different injection currents. On the other hand, the $\omega_{3\,dB}$ where the received electrical power drops to half of its DC value, can be estimated by $\sqrt{1+\sqrt{2}}\,\omega_R \approx 1.55\,\omega_R$ for a small damping [13]. After some simplifications we can write the $f_{3\,dB}$ as follows:

$$f_{3\,dB} \approx \frac{1.55}{2\pi}\sqrt{\frac{\Gamma v_g a}{h\nu V}\frac{(\alpha_i+\alpha_m)}{\alpha_m}P_0} \tag{2.45}$$

Similar to the resonance frequency the $f_{3\,dB}$ also improves by increasing the output power. However, due to the thermal limitations as well as the high power mirror facet damage, the small signal response might be diminished for very high output powers [13].

Equations (2.44) and (2.45) are simple and straightforward relations based on a simple model for the gain parameter. In order to investigate the small signal dynamics of a laser diode thoroughly, some well-known effects such as gain compression and lateral spatial hole burning have to be considered [13, 16]. However, for the operation of the laser well above threshold, these relations are accurate and useful in investigating the device behavior. As can be derived from these equations, one way to increase the small signal bandwidth of the laser is to decrease the cavity volume. On the other hand, in order to avoid the limitations of the high power operation, one can minimize the threshold current to boost the bandwidth according to (2.44) which for a DFB laser is achievable by increasing the coupling coefficient

of the grating or decreasing the mirror loss. However, this in turn can increase the cavity lifetime which will diminish the small signal performance of the laser. Therefore, all these trade-offs have to be considered in designing and fabricating efficient laser diodes, specifically DFB lasers.

2.3.4 Large signal characteristics

The small signal response discussed in the previous section deals with small perturbations in the steady state condition. However, for practical purposes, in communication applications, pulses with fast transitions are involved for which the amplitude of the perturbation is comparable with the steady state injection current. Therefore, the linear approach used in the investigation of the small signal dynamics is no more valid in the large signal analysis.

Unlike the small signal analysis, the large signal response of the laser diode based on the rate equations cannot be solved analytically and numerical methods based on the iteration scheme have to be used. This can be done by using well-known numerical methods for solving ordinary differential equations such as fourth-order Runge–Kutta method. Figure 2.8 depicts the large signal analysis of a DFB laser by plotting the carrier and photon densities versus time. Indeed, there are some important concepts which need to be discussed further here. As can be seen in Figure 2.8, by applying a DC current at $t = 0$, the carrier density follows the injection current with a finite rise time. However, the photon density does not increase till the carrier density reaches the threshold. At this point, the photon density turns on with an overshoot after a delay time of t_d which is called the turn-on delay of the laser.
The turn-on delay of the laser can be derived using the rate equations (2.25) and

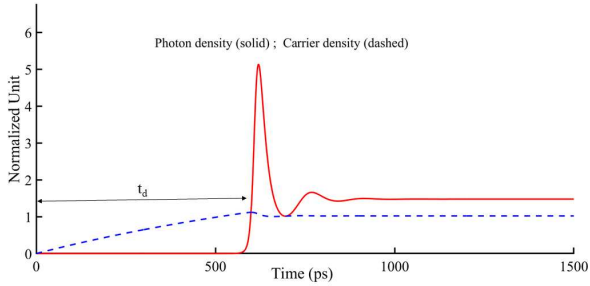

Figure 2.8: Typical carrier and photon density behavior of a single mode laser when it is switched on. The current is supposed to be applied at $t = 0$.

(2.26). By assuming the initial bias current as I_1 and the modulated current as I_2 we can consider two possible cases for the large signal modulation of the laser.

i) $I_1 < I_{th}$: for the initial bias current below its threshold value, the carrier density N is smaller than the threshold density N_{th} and the photon density is very small (there is only the spontaneous emission), hence the stimulated emission term in the carrier rate equation can be neglected. Thus, equation (2.25) can be written as:

$$\frac{dN}{dt} = \frac{\eta_i I}{qV} - \frac{N}{\tau} \tag{2.46}$$

If now the modulation is applied and the current is switched on from I_1 below the threshold to the value I_2 above the threshold, the carrier density increases to reach the threshold value and clamp at N_{th}. The turn-on delay time can be derived from equation (2.46) according to [17]:

$$t_d = \tau \ln \frac{I_2 - I_1}{I_2 - I_{th}} \tag{2.47}$$

The carrier lifetime τ of the typical DFB laser diodes with InGaAlAs and InGaAsP MQW active region is of the order of ns which leads to a turn-on delay time of a similar order of magnitude if the laser diode is biased below threshold. This operation condition cannot be tolerated in high bit rate data transmission. However, this issue can be avoided if the laser is biased well above threshold which is the second possible case as will be discussed below.

ii) $I_1 > I_{th}$: Even when the laser diode is biased above the threshold current, by applying the modulation current the photon density follows the variation with a time delay. However, since the laser operates at the steady state well above threshold, the carrier density is close to the threshold value.
In order to investigate the large signal modulation of the laser biased above the threshold current, the rate equations (2.25) and (2.26) have to be solved numerically. However, an intuitive analytical approach can be derived with some valid approximations. To this end, suppose the laser is biased at I_1 above the threshold current with a photon density $N_{p,m1}$ and at the time $t = 0$, a pulse current with a peak value of I_2 is applied. After a time interval of t_{on} (which is much smaller than carrier lifetime τ) the photon density reaches to a value $N_{p,m2}$ which is larger than $N_{p,m1}$. Therefore, rate equations (2.25) and (2.26) for the time interval $t = 0 < t < t_{on}$ can be written as:

$$\frac{dN}{dt} = \frac{I_2 - I_1}{qV} \tag{2.48}$$

$$\frac{dN_{p,m}}{dt} = \Gamma v_g a (N - N_{th}) N_{p,m} \tag{2.49}$$

where we used equations (2.32) and (2.39). After some simplifications, the switch-on time of the laser can be derived as [18]:

$$t_{on} = \frac{\sqrt{2}}{\omega_R}\sqrt{\ln\frac{N_{p,m2}}{N_{p,m1}}} = \frac{\sqrt{2}}{\omega_R}\sqrt{\ln\frac{P_2}{P_1}} \tag{2.50}$$

here P_1 and P_2 are the output optical power of the laser corresponding to bias currents I_1 and I_2, respectively. ω_R is the angular relaxation resonance frequency of the small signal response of the system given in the equation (2.44). The equation (2-50) assures that for a typical laser diode biased above threshold, the turn-on delay time of smaller than 100 ps is achievable which is desirable for high bit rate data transmission [18]. In this regard, for a large signal modulation, the DFB laser is usually biased above threshold before applying the large signal modulation current.

2.3.5 Noise characteristics of laser diodes

In derivations of the equations described in sections 2.3.1 and 2.3.2, we assumed the steady state condition in which the carrier and photon densities are constant. However, in reality the carrier and photon recombination and generation are random processes. These random processes cause instantaneous time variations in the carrier and photon densities even under a constant bias condition. Thus, the output optical power fluctuates due to the variations in the photon density which results in intensity noise. These fluctuations in the light intensity are expressed by the so-called relative intensity noise (RIN). On the other hand, the random modulation of the carrier density leads to variations in the lasing wavelength which causes a finite spectral linewidth for the lasing mode. This spectral linewidth of the main mode of the laser is usually called the laser linewidth.
In order to quantify the noise behavior in laser diodes, we modify the rate equations (2.25) and (2.26). To investigate the frequency and phase noise of the laser diode we need to add another rate equation for the phase of the optical mode. Indeed, as the optical gain changes as a result of the fluctuation in the carrier population N, the refractive index n of the optical mode also changes. In other words, amplitude modulation in semiconductor lasers always leads to phase modulation due to the carrier-induced changes in the mode index. Therefore by adding a proper rate equation for the phase of the optical mode the complete set of rate equations can be written as [13, 19]:

$$\frac{dN}{dt} = \frac{\eta_i I}{qV} - \frac{N}{\tau} - v_g g N_{p,m} + F_N \tag{2.51}$$

$$\frac{dN_{p,m}}{dt} = [\Gamma v_g g - \frac{1}{\tau_p}]N_{p,m} + \Gamma R'_{sp} + F_P \tag{2.52}$$

$$\frac{d\phi}{dt} = \frac{1}{2}\alpha\Gamma v_g dN + F_\phi \tag{2.53}$$

where time dependent functions F_N, F_P, and F_ϕ are the Langevin forces which are assumed to have a Gaussian distribution with zero mean as follow [19, 20]:

$$\langle F_i(t)F_j(t')\rangle = 2D_{ij}\delta(t-t') \tag{2.54}$$

here $i, j = P, N, or \phi$, and D_{ij} represent the diffusion coefficients. The major contribution to the laser noise originates in two diffusion coefficients $D_{PP} = \Gamma R'_{sp} N_{p,m}$ and $D_{\phi\phi} = \Gamma R'_{sp}/2N_{p,m}$, since other terms can be virtually set to zero [13, 19]. In addition, α in equation (2.53) denotes the linewidth enhancement factor which describes the relationship between the real and imaginary part of the carrier induced index variation [21].
In order to derive accurate relations for the RIN and linewidth, we modify the gain defined in equation (2.39) by considering the fact that its variation dg can be further affected by both carrier and photon density variations as [13]:

$$dg = adN - a_p dN_{p,m} \tag{2.55}$$

where $a = \partial g/\partial N$, and $a_p = -\partial g/\partial N_{p,m}$. Equation (2.55) shows that the gain increases with rising carrier density while it decreases with increasing photon density.

2.3.5.1 Relative Intensity Noise

Assuming a laser diode with a mean optical power of P_0, as shown in Figure 2.9, the RIN is defined as the noise of the optical power $\delta P(t)$ to the mean power $\langle P(t)\rangle^2$ according to:

$$RIN = \frac{\langle \delta P(t)^2\rangle}{\langle P(t)\rangle^2} = \frac{\langle \delta P(t)^2\rangle}{P_0^2} \tag{2.56}$$

By defining the intensity-autocorrelation function as [19]:

$$C_{PP}(\tau) = \langle \delta P(t)\delta P(t+\tau)\rangle / P_0^2 \tag{2.57}$$

where the $\delta P = P - P_0$ stands for small fluctuations in the power level, the Fourier transform of the $C_{PP}(\tau)$ represents the RIN spectrum according to [19]:

$$RIN(\omega) = \int_{-\infty}^{\infty} C_{PP}(\tau)e^{-j\omega t}\, dt \tag{2.58}$$

Using equations (2.51) and (2.52) and linearizing them in δN and $\delta N_{p,m}$, the RIN of a laser diode can be approximated by [13]:

$$\frac{RIN}{\Delta f} = \frac{h\nu}{P_0}\left[\frac{a_1 + a_2\omega^2}{\omega_R^4}|H(\omega)^2| + 1\right] \tag{2.59}$$

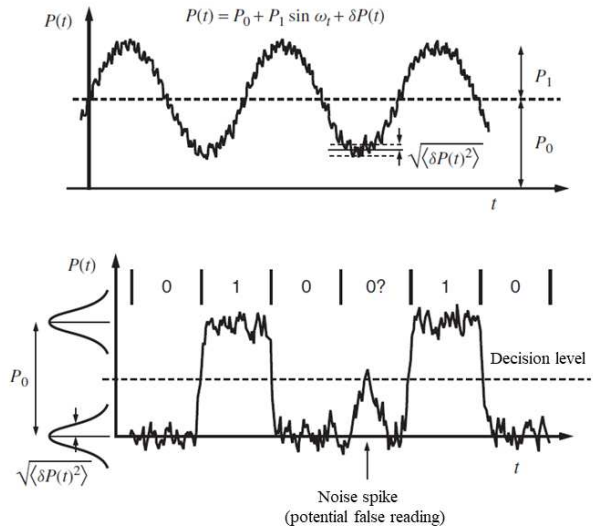

Figure 2.9: The demonstration of the noise in modulated laser signals for both analog and digital applications [13].

where $H(\omega)$, the small signal modulation transfer function, a_1 and a_2 are defined as:

$$H(\omega) = \frac{\omega_R^2}{\omega_R^2 - \omega^2 + j\gamma\omega} \tag{2.60}$$

$$a_1 = \frac{2\Gamma R'_{sp} P_0}{N_{p,m} h\nu \tau_{\Delta N}^2} + \eta_0 \omega_R^4 [\frac{(I + I_{th})}{(I - I_{th})} - 1] \tag{2.61}$$

$$a_2 = \frac{2\Gamma R'_{sp} P_0}{N_{p,m} h\nu} - 2\eta_0 \omega_R^2 \frac{\Gamma a_p}{a} \tag{2.62}$$

here γ is the damping rate of the relaxation oscillation [13]. As can be derived from the equation (2.60) and Figure 2.10, there is a strong peak in the RIN spectrum around the relaxation oscillation frequency ω_R. In addition, for an emitted field in a complete coherent state, the noise power spectral density is limitted to a minimum value of $h\nu P_0$ which is called the shot noise floor of the laser. At a low output power, the noise is more dominant and has significant enhancement near the relaxation resonance frequency of the laser. At higher powers, the RIN is decreased and

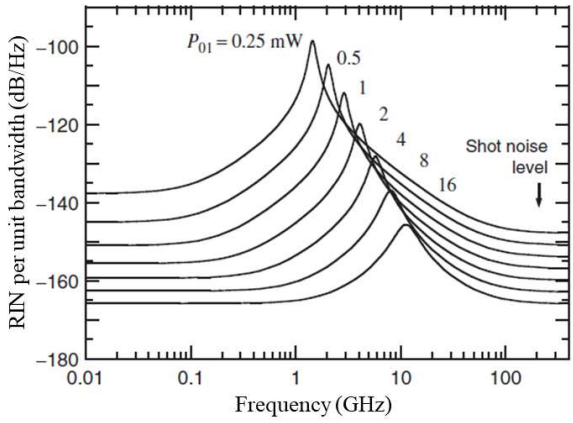

Figure 2.10: Calculated relative intensity noise at different output power levels for an InGaAs/GaAs in-plane laser [13].

is closer to the shot noise limit with flatter response at frequencies beyond the relaxation resonance frequency [13].

2.3.5.2 Laser linewidth

By taking the Fourier transform of the equation (2.53), the frequency noise spectral density can be written as [13]:

$$S_\nu(\omega) = (\frac{\alpha\Gamma v_g a}{4\pi})^2 S_N(\omega) + \frac{1}{4\pi^2} D_{\phi\phi} \tag{2.63}$$

where $D_{\phi\phi} = \Gamma R'_{sp}/2N_{p,m}$. The first term in the right hand side of the above equation denotes the carrier noise, which induces refractive index changes yielding the lasing frequency to fluctuate, and the second term is the intrinsic phase noise of the laser caused by the spontaneous emission. The carrier density noise spectral density is given by [13]:

$$S_N(\omega) = \frac{2R'_{sp}}{(v_g a)^2 \Gamma N_{p,m}} |H(\omega)|^2 \tag{2.64}$$

The FM noise behavior of a diode laser is dominated by the $1/f$ and thermal noise at low frequencies which are not included in equation (2.63). At higher frequencies,

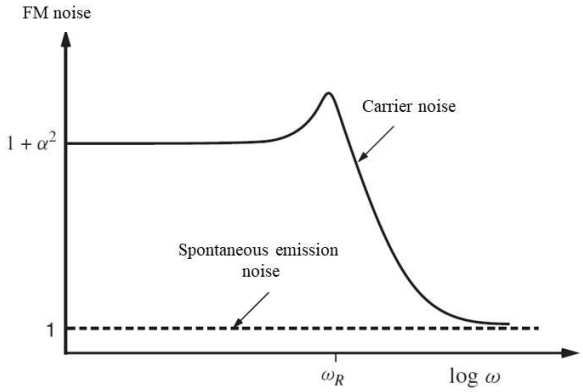

Figure 2.11: Frequency noise spectrum illustrating contributions from both carrier and spontaneous emission noise [13].

as depicted in Figure 2.11, the carrier noise is the major term. However, at high enough frequencies it also becomes negligible and the FM noise of the laser mainly stems from the spontaneous emission noise.
The spectral linewidth $\Delta\nu$ defined as the full-width at half-maximum (FWHM) of the Lorentzian shape spectral linewidth is given by [13, 22]:

$$\Delta\nu = 2\pi S_\nu(0) = \frac{\Gamma R'_{sp}}{4\pi N_{p,m}}(1+\alpha^2) \tag{2.65}$$

Using $R'_{sp} = \Gamma v_g g_{th} n_{sp}/V$ and $N_{p,m} = P/(h\nu V_p v_g \eta_0 \Gamma g_{th})$, and substituting them into the equation (2.65) one gets [13]:

$$\Delta\nu = \frac{(\Gamma v_g g_{th})^2 \eta_0}{4\pi P} n_{sp} h\nu (1+\alpha^2) \tag{2.66}$$

where P is the optical output power and $\eta_0 = \frac{\alpha_m}{\alpha_i+\alpha_m}$ denotes the optical efficiency of the laser. The first term in the equation (2.65) describes the contribution of the spontaneous emission in the intrinsic linewidth of the laser diode and the second term is the broadening mechanism caused by the carrier fluctuations. Indeed, the linewidth enhancement factor α is a measure of the gain changes due to the carrier induced fluctuations in the refractive index of the lasing mode which is typically between 2 and 6 [13]. The intrinsic linewidth which is also called Lorentzian linewidth decreases with increasing output power. The rebroadening of the linewidth at the very high power levels is also observed experimentally which can be due to

the fluctuation of the bias current, $1/f$ noise, or the effect of side modes specifically in a DFB laser [22, 23]. As can be indirectly derived from the equation (2.65), the linewidth becomes narrower using longer cavities since the spontaneous emisson noise is lower for the longer cavities.

2.4 Wall-plug and differential efficiencies

The wall-plug efficiency of a laser system can be defined as its total electrical-to-optical power efficiency. Indeed, the ratio of optical output power P_o to the consumed electrical input power P_e is called the wall-plug efficiency of the laser and is usually represented in percentage as follows:

$$WPE = \frac{P_o}{P_e} \times 100 \tag{2.67}$$

Depending on the definition of the consumed electrical power on the wall plug, it can include losses in the power supply as well as the power required for the cooling system or it can only be calculated based on the electrical power delivered to the laser system. As it is common for a laser diode case, we follow the second definition in this work and consider the consumed electrical power delivered to the laser contact pads.

Among the different types of semiconductor lasers, vertical cavity surface emitting lasers (VCSELs) can be good candidates for interconnects due to their high wall-plug efficiency, compactness and low threshold. They can provide up to 60 % wall-plug efficiency [24, 25]. However, their limited optical power makes them less desirable wavelength-division multiplexing (WDM) modules [26]. On the other

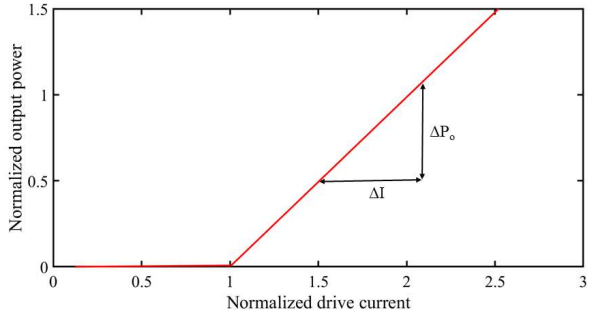

Figure 2.12: The typical L-I curve of an in-plane laser diode .

hand, edge emitting laser diodes such as DFB or distributed Bragg reflector (DBR) lasers are suitable for the fabrication of compact WDM sources, but have suffered from somewhat lower wall-plug efficiency in the past. A high wall-plug efficiency normally leads to a low electrical power consumption for the optical transmitter and requires typically also less power consuming cooling. This is especially important where many transmitters are present in a limited area (e.g., in datacenters).
Another important characteristic of a laser system (specifically a diode laser such as a DFB laser) is the differential efficiency of the laser above the threshold. As Figure 2.12 illustrates, the differential efficiency is defined as the slope ($\Delta P_o/\Delta I$) of the laser L-I (laser output power versus the bias current) above the threshold value. For a laser diode, the L-I curve is typically close to linear above its threshold, hence the differential efficiency is sometimes expressed as the slope efficiency.
The differential quantum efficiency η_d of a laser diode can be related to the slope efficiency according to:

$$\eta_d = \frac{\Delta P_o}{\Delta I}\frac{q}{h\nu} \tag{2.68}$$

By taking a derivative with respect to the current in the equation (2.36), we get:

$$\frac{\Delta P_o}{\Delta I} = (\frac{h\nu}{q})\eta_d = (\frac{h\nu}{q})\frac{\eta_i \alpha_m}{\alpha_i + \alpha_m} \tag{2.69}$$

2.5 Linewidth of laser diodes with distant reflections

Incorporating an optical feedback provided by an external mirror or even the reflection from a grating coupler on a chip, can have beneficial or detrimental effects on the performance of laser diodes. For a Fabry-Perot laser, the optical feedback can act as a filter to suppress the side modes while in single mode lasers such as a DFB laser it can be useful in narrowing the laser linewidth or even tuning the lasing wavelength.
Figure (2.13) depicts the schematic configuration of a single cavity (solitary) laser diode with facets placed at $z = 0$ and $z = L$ and an external feedback modeled by a reflection of r_{2ext} which together form a compound cavity. It is assumed there are no multiple reflections inside the single cavity laser, as well as the external cavity (e.g a solitary Fabry-Perot laser coupled to an external cavity). Although the following derivations will be carried out for solitary laser diode without multiple reflections along the cavity, it is shown that the results qualitatively apply for a DFB laser case [18]. However, a more precise and complicated model to analyze the feedback effects in DFB lasers can be found in [27].
The phase condition for the compound cavity shown in Figure 2.13 can be written as [18]:

$$2\beta L + \phi_r = 2n\pi \tag{2.70}$$

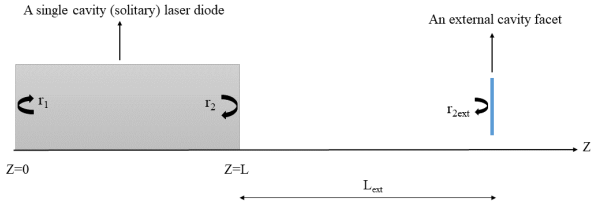

Figure 2.13: Schematic of a single cavity (solitary) laser diode coupled to an external cavity with a length of L_{ext}. The configuration as a whole builds a compound cavity.

Here β is the propagation constant of the field in the solitary laser and the round trip phase ϕ_r injected by the external feedback is equal to $2\pi\nu\tau_{ext}$ where ν is the frequency of the lasing mode and τ_{ext} describes the round trip delay time of the reflected field (forth and back in the external cavity of the length L_{ext}). It is now useful to extend and investigate further the equation (2.70) by defining the effective index of the cavity as $n_{eff} = c\beta/2\pi\nu$, with c the speed of light in the vacuum. By substituting the latter term in the equation (2.70) and using the fact that the effective index of the cavity as well as the emission frequency change due to the feedback, we get [18]:

$$\Delta\phi_L = \Delta(n_{eff}\nu)\frac{4\pi L}{c} + \phi_r = \frac{4\pi L}{c}[\nu_0\Delta n_{eff} + n_{eff}(\nu - \nu_0)] + \phi_r \quad (2.71)$$

where ν_0 denotes the emission frequency of the laser without any external reflector. $\Delta\phi_L$ is the round trip phase change compared to $2n\pi$ with $n = 0, 1, 2, 3, ...$ (the allowed longitudinal modes of the solitary cavity are determined by the phase condition when the round trip phase is a multiple of 2π). Therefore, the emission frequencies of the compound cavity are determined by $\Delta\phi_L$=0. On the other hand, the change in the effective index of the lasing mode can be related to the change in the carrier density and the gain. By applying these relations and after some simplifications, the change in the round trip phase of the compound cavity can be written as [18]:

$$\Delta\phi_L = 2\pi\tau_L(\nu - \nu_0) + \kappa_{ext}\sqrt{1+\alpha^2}sin(2\pi\nu\tau_{ext} + \arctan\alpha) \quad (2.72)$$

here, $\tau_L = 2n_gL/c$ denotes the round trip time of the solitary laser where n_g is the group refractive index of the mode and α describes the linewidth enhancement factor. The parameter κ_{ext} is the coupling coefficient of the external feedback to the laser cavity which in reality expresses the strength of the external feedback and is defined as:

$$\kappa_{ext} = \frac{r_{2ext}}{r_2}(1 - |r_2|^2) \quad (2.73)$$

In order to investigate the effect of the external feedback on the emission frequencies of the laser, the round trip phase change $\Delta\phi_L$ given in the equation (2.72) is plotted versus the frequency in Figure (2.14). Three different regimes are analyzed in this figure based on the strength of the external feedback by defining a feedback coefficient C which is related to the coupling coefficient κ_{ext} as:

$$C = \frac{\tau_{ext}}{\tau_L}\kappa_{ext}\sqrt{1+\alpha^2} \tag{2.74}$$

Without an external reflector the $\Delta\phi_L$ varies linearly with the frequency and as it is depicted with the dashed curve in the Figure (2.14), there will be a zero in the frequency axis for $\nu = \nu_0$. The solid line in this figure illustrates the effect of the weak external feedback with $C < 1$. As can be seen with a weak external feedback $\Delta\phi_L$ still varies monotonically and a single zero for the $\Delta\phi_L$ occurs similar to the case without feedback. However, the emission frequency is shifted due to the effect of the external feedback. Finally, for a strong reflector ($C > 1$), multiple zeros for the $\Delta\phi_L$ can be found due to the strong oscillation yielding to several external cavity modes. This regime can make the laser spectrum unstable by well-known mechanisms such as coherence collapse in which multiple oscillating modes can result in an intrinsic linewidth of the order of GHz.

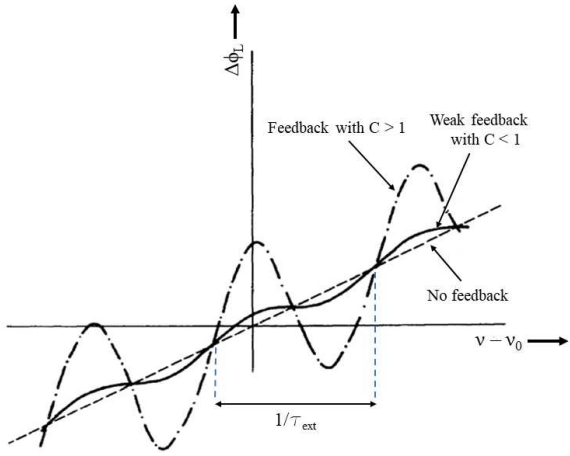

Figure 2.14: The round trip phase change $\Delta\phi_L$ versus optical frequency ν with and without optical feedback. The phase condition for the compound cavity is satisfied for $\Delta\phi_L = 0$ [18].

Now, by understanding the mechanism of the external feedback and its effect on the laser emission frequency, we move one step further to investigate how the spectral linewidth of the laser can be affected by the external feedback. It is shown that the effect of the external feedback can be implemented in the rate equations (2.52) and (2.53) as below [18]:

$$\frac{dN_{p,m}}{dt} = [\Gamma v_g g - \frac{1}{\tau_p}]N_{p,m} + \Gamma R'_{sp} + F_p + \frac{2}{\tau_L}K_{ext}\sqrt{N_{p,m}(t)N_{p,m}(t-\tau_{ext})}. \cos(\omega_0\tau_{ext} + \phi(t) - \phi(t-\tau_{ext})) \tag{2.75}$$

$$\frac{d\phi}{dt} = \frac{1}{2}\alpha\Gamma v_g adN + F_\phi - \frac{1}{\tau_L}K_{ext}\sqrt{\frac{N_{p,m}(t-\tau_{ext})}{N_{p,m}(t)}}. \cos(\omega_0\tau_{ext} + \phi(t) - \phi(t-\tau_{ext})) \tag{2.76}$$

Unfortunately, there are no analytical solutions for the above nonlinear equations. However, by performing a small signal analysis, it is shown that the linewidth of a compound cavity laser with an external feedback can be related to the linewidth of the solitary laser (equation (2.66)) according to [28–31] :

$$\Delta\nu_c = \frac{\Delta\nu}{[1 + C\cos(\phi_{ext} + \arctan\alpha)]^2} \tag{2.77}$$

As can be derived from equation (2.77), for a laser without feedback (C=0), $\Delta\nu_c = \Delta\nu$. Depending on the feedback coefficient C and the phase of the external cavity ϕ_{ext}, the linewidth of the compound cavity can increase or decrease. If $\phi_{ext} = 2n\pi - \arctan\alpha$, the feedback system is in-phase and the linewidth will be narrowed to $\Delta\nu/(1+C)^2$. On the other hand for the out of phase feedback regime ($\phi_{ext} = 2n\pi + \pi - \arctan\alpha$), the linewidth will be broadened to $\Delta\nu/(1-C)^2$. For the condition between the minimum and the maximum value, the linewidth of the compound cavity laser depends on the external cavity phase and for a specific phase and feedback condition it can be also equal to the linewidth of the solitary laser. Experimental results proved that linewidth narrowing up to an order of magnitude is achievable by applying a proper feedback and phase tuning [32, 33].

2.6 Conclusion

In this chapter we discussed the theory of DFB lasers. We started with a brief introduction on semiconductor laser diodes and discussed the need for single mode lasers. We then briefly discussed the coupled mode equations, which were solved approximately for two different types of DFB lasers. After that, we focused on the rate equations. Using these equations, the static and dynamic behavior of the laser followed by the noise analysis, have been investigated. Subsequently, the wall-plug

and differential efficiencies have been explained. Finally, the effect of the external feedback on the linewidth of the laser has been studied.

Bibliography

[1] R. N. Hall, G. E. Fenner, J. Kingsley, T. Soltys, and R. Carlson, "Coherent light emission from GaAs junctions," *Physical Review Letters*, vol. 9, no. 9, p. 366, 1962.

[2] M. I. Nathan, W. P. Dumke, G. Burns, F. H. Dill Jr, and G. Lasher, "Stimulated emission of radiation from GaAs p-n junctions," *Applied Physics Letters*, vol. 1, no. 3, pp. 62–64, 1962.

[3] N. Holonyak Jr and S. F. Bevacqua, "Coherent (visible) light emission from Ga ($As_{1-x}P_x$) junctions," *Applied Physics Letters*, vol. 1, no. 4, pp. 82–83, 1962.

[4] I. Hayashi, M. Panish, P. Foy, and S. Sumski, "Junction lasers which operate continuously at room temperature," *Applied Physics Letters*, vol. 17, no. 3, pp. 109–111, 1970.

[5] J. Ripper, J. Dyment, L. D'Asaro, and T. Paoli, "Stripe-geometry double heterostructure junction lasers: mode structure and CW operation above room temperature," *Applied Physics Letters*, vol. 18, no. 4, pp. 155–157, 1971.

[6] J. E. Carroll, J. Whiteaway, D. Plumb, and R. Plumb, *Distributed feedback semiconductor lasers*, vol. 10. IET, 1998.

[7] L. Zhang and J. E. Carroll, "Large-signal dynamic model of the DFB laser," *IEEE Journal of Quantum Electronics*, vol. 28, no. 3, pp. 604–611, 1992.

[8] L. Zhang, S. F. Yu, M. Nowell, D. Marcenac, J. Carroll, and R. Plumb, "Dynamic analysis of radiation and side-mode suppression in a second-order DFB laser using time-domain large-signal traveling wave model," *IEEE Journal of Quantum Electronics*, vol. 30, no. 6, pp. 1389–1395, 1994.

[9] S. McCall and P. Platzman, "An optimized $\pi/2$ distributed feedback laser," *IEEE journal of quantum electronics*, vol. 21, no. 12, pp. 1899–1904, 1985.

[10] H. Kogelnik and C. Shank, "Coupled-wave theory of distributed feedback lasers," *Journal of applied physics*, vol. 43, no. 5, pp. 2327–2335, 1972.

[11] J. Buus, *Single frequency semiconductor lasers*. SPIE Press, 1991.

[12] H. Ghafouri-Shiraz, *Distributed feedback laser diodes and optical tunable filters*. John Wiley & Sons, 2003.

[13] L. A. Coldren, S. W. Corzine, and M. L. Mashanovitch, *Diode lasers and photonic integrated circuits*. John Wiley & Sons, 2012.

[14] J. Hader, J. Moloney, and S. Koch, "Beyond the abc: carrier recombination in semiconductor lasers," in *Physics and Simulation of Optoelectronic Devices XIV*, vol. 6115, pp. 304–310, SPIE, 2006.

[15] R. S. Tucker, "High-speed modulation of semiconductor lasers," *IEEE transactions on electron devices*, vol. 32, no. 12, pp. 2572–2584, 1985.

[16] G. Morthier and P. Vankwikelberge, *Handbook of distributed feedback laser diodes*. Artech House, 2013.

[17] K. Konnerth and C. Lanza, "Delay between current pulse and light emission of a gallium arsenide injection laser," *Applied Physics Letters*, vol. 4, no. 7, pp. 120–121, 1964.

[18] K. Petermann, *Laser diode modulation and noise*, vol. 3. Springer Science & Business Media, 1991.

[19] G. P. Agrawal and N. K. Dutta, *Long-wavelength semiconductor lasers*, vol. 1. Springer, 1986.

[20] M. Lax, "Classical noise IV: Langevin methods," *Reviews of Modern Physics*, vol. 38, no. 3, p. 541, 1966.

[21] C. Henry, "Theory of the linewidth of semiconductor lasers," *IEEE Journal of Quantum Electronics*, vol. 18, no. 2, pp. 259–264, 1982.

[22] G. P. Agrawal, *Fiber-optic communication systems*, vol. 222. John Wiley & Sons, 2012.

[23] K. Kikuchi, "Effect of 1/f-type FM noise on semiconductor-laser linewidth residual in high-power limit," *IEEE Journal of Quantum Electronics*, vol. 25, no. 4, pp. 684–688, 1989.

[24] M. Miller, M. Grabherr, R. King, R. Jager, R. Michalzik, and K. J. Ebeling, "Improved output performance of high-power VCSELs," *IEEE Journal of Selected Topics in Quantum Electronics*, vol. 7, no. 2, pp. 210–216, 2001.

[25] T. Kageyama, K. Takaki, S. Imai, Y. Kawakita, K. Hiraiwa, N. Iwai, H. Shimizu, N. Tsukiji, and A. Kasukawa, "High efficiency 1060nm VCSELS for low power consumption," in *2009 IEEE International Conference on Indium Phosphide & Related Materials*, pp. 391–396, IEEE, 2009.

[26] S. Matsuo and T. Kakitsuka, "Low-operating-energy directly modulated lasers for short-distance optical interconnects," *Advances in Optics and Photonics*, vol. 10, no. 3, pp. 567–643, 2018.

[27] F. Favre, "Theoretical analysis of external optical feedback on DFB semiconductor lasers," *IEEE Journal of Quantum Electronics*, vol. 23, no. 1, pp. 81–88, 1987.

[28] P. Spano, S. Piazzolla, and M. Tamburrini, "Theory of noise in semiconductor lasers in the presence of optical feedback," *IEEE journal of quantum electronics*, vol. 20, no. 4, pp. 350–357, 1984.

[29] Y. Chen, "Phase noise characteristics of single mode semiconductor lasers with optical feedback," *Applied physics letters*, vol. 44, no. 1, pp. 10–12, 1984.

[30] R. Tkach and A. Chraplyvy, "Regimes of feedback effects in 1.5-μm distributed feedback lasers," *Journal of Lightwave technology*, vol. 4, no. 11, pp. 1655–1661, 1986.

[31] H. Olesen, J. Osmundsen, and B. Tromborg, "Nonlinear dynamics and spectral behavior for an external cavity laser," *IEEE journal of quantum electronics*, vol. 22, no. 6, pp. 762–773, 1986.

[32] M. Fleming and A. Mooradian, "Spectral characteristics of external-cavity controlled semiconductor lasers," *IEEE Journal of Quantum Electronics*, vol. 17, no. 1, pp. 44–59, 1981.

[33] E. Brinkmeyer, W. Brennecke, R. Ulrich, *et al.*, "Fibre Bragg reflector for mode selection and line-narrowing of injection lasers," *Electronics letters*, vol. 3, no. 22, pp. 134–135, 1986.

3

Design and fabrication of III-V-on-Si C-band distributed feedback laser diodes

This chapter describes the design and the standard fabrication procedure for heterogeneously integrated InP on SOI DFB lasers. First, we give an overview of the typical III-V-on-Si DFB laser configuration which has been developed for the heterogeneous integration approach in the UGent Photonics Research Group and discuss the drawback of these structures. Then, we present the idea of how to optimize these structures and improve the performance of the III-V-on-Si DFB lasers. Subsequently, the standard process flow is described.

3.1 Overview of earlier III-V-on-Si DFB lasers 3-2
3.1.1 Optical loss characterization 3-3
3.1.2 Carrier lifetime characterization 3-5
3.2 Optical design of a compact cavity 3-8
3.3 Integrated lasers realized by bonding 3-13
3.3.1 SOI Fabrication 3-13
3.3.2 Bonding Process 3-16
3.3.3 III-V Process flow 3-18
3.4 Conclusion 3-29

3.1 Overview of earlier III-V-on-Si DFB lasers

Figure 3.1 gives a schematic of a typical heterogeneously integrated DFB laser on the Si-on-insulator (SOI) platform, which has been developed in the UGent Photonics Research Group over the last two decades. A rib waveguide and DFB grating are patterned on a 400 nm thick Si device layer by a 180 nm deep dry etch using 193 nm deep UV lithography. Then, the silicon waveguide layer is planarized and a thin DVS-BCB layer is used to bond III-V materials on top of the SOI. After that, by using a standard III-V processing, an active waveguide on top of the Si waveguide is fabricated and by a metallization process electrical contacts are provided.

As can be seen in Figure 3.1, the structure is divided into three parts. In the center of the device, the optical mode is dominantly confined to the III-V waveguide, which provides the required gain for the lasing. At both sides of this configuration, there is a coupling region that couples light from the III-V waveguide to the underlying silicon waveguide by means of an adiabatic taper coupler [1, 2]. After coupling to the silicon waveguide underneath, light is guided by the silicon waveguide without any III-V layer on top. The output light can be collected through a grating or edge coupler fabricated on the same chip.

There are major challenges with this conventional design which limit the performance of the realized devices. First, the optical mode in this configuration is

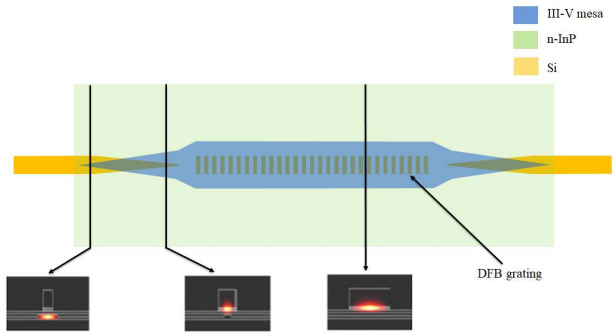

Figure 3.1: The top and cross-sectional views of the coupling structure of heterogeneously integrated III-V-on-Si lasers. In these early demonstrated devices, the optical mode is strongly confined to the III-V waveguide. In order to couple the light to the silicon waveguide underneath, long taper configurations have to be implemented both in the III-V and silicon waveguides.

strongly confined to the III-V waveguide layer. This can be beneficial in providing a higher modal gain and confinement factor, yielding higher bandwidth modulation characteristics. However, the cavity loss in these devices is high since the III-V material is highly absorbing due to the intervalence band absorption mechanism [3, 4]. As shown in the equation (2.36), by increasing the internal loss of the cavity the output power decreases, which leads to a lower wall-plug efficiency. In addition, since the optical mode is mostly confined to the III-V waveguide, incorporating a long taper configuration (>100 µm) is necessary to couple the light to the silicon waveguide underneath [1, 2]. Using such a long taper increases the power consumption of the laser diode since in addition to the cavity (the central part shown in Figure 3.1), the two long taper sections at the ends of the cavity have to be pumped. In the following, the characterization of the optical loss including the coupling loss of the taper and the internal loss of the cavity are discussed. In addition, the characterization of the carrier lifetime in two different epitaxial structures is given.

3.1.1 Optical loss characterization

We performed an experimental study on the coupling loss of the taper structure as well as the internal loss of the III-V cavity. Due to the specific configuration of such devices, incorporating tapered waveguides on both III-V and silicon layer is crucial to facilitate the coupling of light from the III-V active region to the silicon waveguide underneath. In order to measure the optical loss of the taper sections and that of the III-V cavity, it is necessary to accurately measure the transparency currents of similar lasers with different lengths. Then, the optical loss can be obtained by measuring a fiber-to-fiber transmission at the transparency currents of

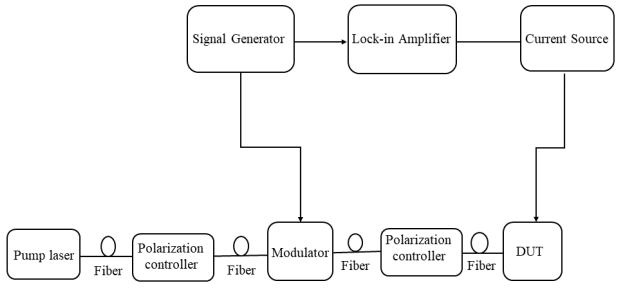

Figure 3.2: Block diagram of the setup for the transparency current measurement.

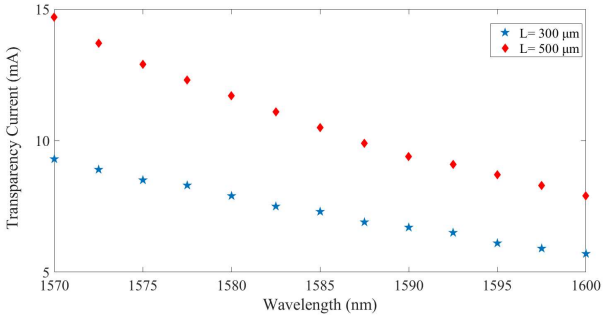

Figure 3.3: The measured transparency currents versus wavelength for two heterogeneously integrated DFB lasers with lengths of 300 µm and 500 µm.

the laser diodes with various lengths. To achieve this, we assume that the fiber-to-fiber transmission T of the full device (i.e. the cavity with taper sections and the input and output grating couplers) is obtained as follows:

$$T = T_1.T_2.e^{-\alpha_i L} \tag{3.1}$$

where, L represents the cavity length (in the case of a DFB laser it denotes the length of the Bragg grating), T_1 and T_2 denote the transmission from the two taper sections incorporated on each side of the cavity, and α_i describes the intrinsic loss coefficient which mainly originates from scattering and intervalence band absorption (IVBA) in the III-V layers. The setup for the transparency current measurement is depicted in Figure 3.2. To measure the transparency current, a tunable external cavity semiconductor laser (pump laser) is used to couple the light into the DFB laser cavity through the on-chip grating coupler. While the input signal is modulated, by sweeping the injection current of the DFB laser, the modulation of the voltage drop across the DFB laser can be detected by a lock-in amplifier. At the transparency current, a change of sign of the lock-in signal occurs because the rate of absorption and amplification balance each other. Thus, the carrier density is no longer affected by the injection of the modulated input signal [5].
The transparency currents as a function of the pump wavelength are measured for several fabricated III-V-on-Si DFB lasers. In Figure 3.3, the results for laser diodes with lengths of 300 µm and 500 µm are shown. By assuming that the light coupling from the silicon waveguide to the III-V waveguide at one side of the cavity is equal to the light coupling from the III-V waveguide to the silicon waveguide at the other side (which is a valid assumption based on the symmetric design of taper sections and the equal output power collected through both grating couplers), T_1 is equal to

T_2. Our measurement results on different structures operating at the transparency current, show up to 1 dB loss per taper section and an intrinsic loss of 20 cm^{-1}. A coupling coefficient between 135 to 200 cm^{-1} was reported for III-V-on-Si lasers with 340 µm long cavity [6]. According to the equation (2.24), a mirror loss of 0.9 cm^{-1} $< \alpha_m <$ 6 cm^{-1} can be derived for these devices.

3.1.2 Carrier lifetime characterization

Two different types of epitaxial structures have been used in the fabrication of heterogeneously integrated III-V-on-Si DFB lasers. Table 3.1 and 3.2 give the composition of these epitaxial layers.
The first epitaxial structure used in this thesis has an Al-containing active region. The detailed composition of the epitaxial structure is presented in Table 3.1. The active region comprises six InGaAlAs quantum wells (6 nm thick with an emission wavelength of 1.55 µm), which are surrounded by InGaAlAs barriers (10 nm thick) with a bandgap wavelength of 1.10 µm.
The second epitaxial stack used for the fabrication of DFB lasers is presented in Table 3.2. This stack consists of six InGaAsP quantum wells (7 nm thick with an emission wavelength of 1.55 µm) with 0.8 % compressive strain. The InGaAsP barriers surrounding the QW layers are 9 nm thick with 0.3 % tensile strain.
In order to measure the carrier lifetime, first the laser is probed by means of a proper RF probe and then the subthreshold RF reflection coefficient ($S11$) is measured using a N9923A FieldFox RF Vector Network Analyzer (VNA). The laser input impedance ($Z_{in} = V/I$) can be extracted from the measured (S_{11}), where I is the modulated current and V denotes the corresponding frequency dependent voltage between the contacts. Then, the differential carrier lifetimes can be found by fitting the real part of the extracted input impedance to the following relation:

$$Re(Z_{in}) = R_s + \frac{R_d}{1 + \omega^2 \tau^2} \tag{3.2}$$

where, impedances R_s and R_d are a frequency independent series resistance component and a frequency and bias dependent component, respectively [7]. Figure 3.4 depicts how the differential carrier lifetime is extracted by fitting to the extracted impedance versus frequency. Figure 3.4(a) illustrates the characterization result for a III-V-on-Si DFB laser with an InGaAsP MQW while Figure 3.4(b) describes the result for the device with an Al-containing MQW active region. It should be emphasized that the two different lasers have the same dimension and have been fabricated under the same fabrication process flow. In order to have a better understanding of the behavior of the differential carrier lifetime in these two different devices, Figure 3.5 depicts the behavior of the differential carrier lifetime versus

Layer	Layer type	Material	Thickness (nm)	Refractive index
28	Sacrificial	InP	100	
27	Etch stop	InGaAs	100	
26	For comparison with TP	InP	60	3.169
25	Cladding N	InP	200	3.169
24	Transition	$Al_{0.423}Ga_{0.047}In_{0.53}As$	40	3.2244
23	SCH	$Al_{0.329}Ga_{0.141}In_{0.53}As$	75	3.27818
12×6	Barrier	$Al_{0.2295}Ga_{0.2805}In_{0.49}As$	10	3.3849
11×6	Well	$Al_{0.075}Ga_{0.225}In_{0.7}As$	6	3.6294
10	Barrier	$Al_{0.2295}Ga_{0.2805}In_{0.49}As$	10	3.3849
9	SCH	$Al_{0.329}Ga_{0.141}In_{0.53}As$	75	3.27818
8	Transition	$Al_{0.423}Ga_{0.047}In_{0.53}As$	40	3.22444
7		Interface layer	5	
6	Cladding P	InP	1000	3.169
5	Cladding P	InP	500	3.169
4	Contact P	InGaAs	100	3.6
3	Contact P	InGaAs	100	3.6
2	Sacrificial	InP	150	
1	Etch stop	InGaAs	150	
	Substrate	InP		

Table 3.1: Description of the InGaAlAs epitaxial structure.

Layer	Layer type	Material	Thickness (nm)	Refractive index	Carrier conc.	Type
25	Sacrificial	InP	100			nid
24	Etch stop	InGaAs	100			nid
23	Cladding N	InP	190	3.169	$1e^{18}$	N
22	SCH	InGaAsP	100	3.3214		nid
11×6	Barrier	InGaAsP	9	3.3214		nid
10×6	Well	InGaAsP	7	3.5434		nid
9	Barrier	InGaAsP	9	3.3214		nid
8	SCH	InGaAsP	100	3.3214		nid
7	Cladding P	InP	500	3.169	$5e^{17}$	P
6	Cladding P	InP	1000	3.169	$2e^{18}$	P
5	Transition	InGaAsP	20	3.2244	$3e^{18}$	P
4	Contact P	InGaAs	200	3.6	$1.5e^{19}$	P
3	Sacrificial	InP	200			nid
2	Etch stop	InGaAs	200			nid
1		InP	50			nid
	Substrate	InP				N

Table 3.2: Description of the InGaAsP epitaxial structure.

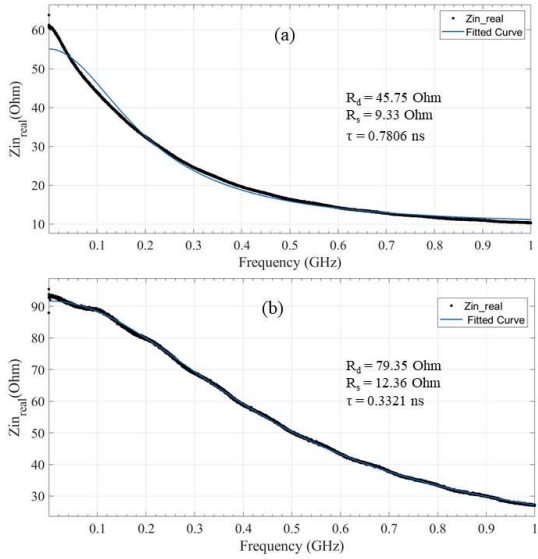

Figure 3.4: The real part of the measured input impedance of III-V-on-Si DFB lasers as well as the fitted curves at a bias current of 2 mA. a) The InGaAsP MQW DFB laser. b) The InAlGaAs MQW DFB laser.

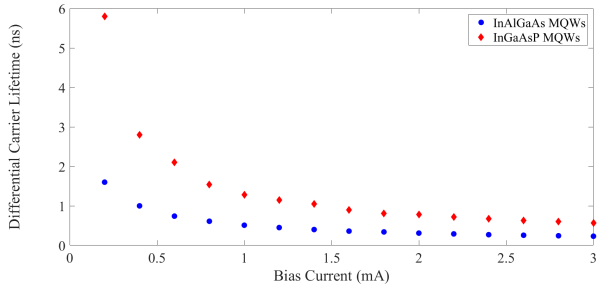

Figure 3.5: Measured differential carrier lifetime as a function of bias current for InAlGaAs and InGaAsP MQWs.

the bias current well below threshold. The frequency span of the measurement is from 30 kHz to 1 GHz in each of these measurements. As can be derived from Figure 3.5, it is observed that Al-containing MQWs have at least 50% faster carrier recombination time due to higher surface recombination.

3.2 Optical design of a compact cavity

According to equations (2.36) and (2.67), a large internal loss of the cavity decreases the output optical power and the corresponding wall-plug efficiency. In addition, it also diminishes the slope efficiency of the laser as given in the equation (2.69). A good compromise to obtain both rather low threshold current and sufficiently high slope efficiency is to try to have equal internal and mirror loss. In order to improve the performance of the heterogeneously integrated lasers, the optical mode inside the cavity has to be engineered. Since the III-V layer stack is highly absorbing due to the intervalence band absorption in the p-type cladding layers, pushing down the hybrid mode into the silicon waveguide can result in a reduction of the internal loss and an increase in internal efficiency. In addition, since the optical mode is predominantly confined to the silicon waveguide, a short linear taper is sufficient to fully couple the light to the SOI circuit. However, the resulting decrease of the optical confinement in the active region can increase the threshold gain (g_{th}) according to the equation (2.32). This results in an increase of the threshold current and a decrease of the modulation bandwidth as described in chapter 2 (section 2.3.3 and equations (2.44) and (2.45)). Considering this trade-off in designing the integrated laser cavity, we use equation (2.32) as follows:

$$g_{th} = \frac{\alpha_m + \alpha_i}{\Gamma} \tag{3.3}$$

where α_m and α_i denote the mirror loss and internal cavity loss, respectively. In order to minimize the threshold gain of the laser, we numerically calculate the internal loss and confinement factor versus the DFB grating etch depth (in a 400 nm silicon platform) and calculate the ratio of the internal loss (α_i) to the confinement factor. As shown in Figure 3.6(a), there is a minimum for the ratio of $\frac{\alpha_i}{\Gamma}$ at 40 nm grating etch depth , meaning that an etch depth of 40 nm can decrease the cavity's internal loss and still keep the confinement factor sufficient enough to meet the above-mentioned trade-off issues. The calculated mirror loss (α_m) is somewhat higher than the calculated internal loss for this etch depth (Figure 3.6(b)). The inclusion of scattering loss would in practice further increase the internal loss, such that mirror loss and internal loss become more equal for the etch depth of 40nm. In addition, in figure 3.6, the calculated values of $\frac{\alpha_i}{\Gamma}$ and $\frac{\alpha_m}{\alpha_i}$ are shown for an etch depth of 180 nm which is the standard etch depth in the previously

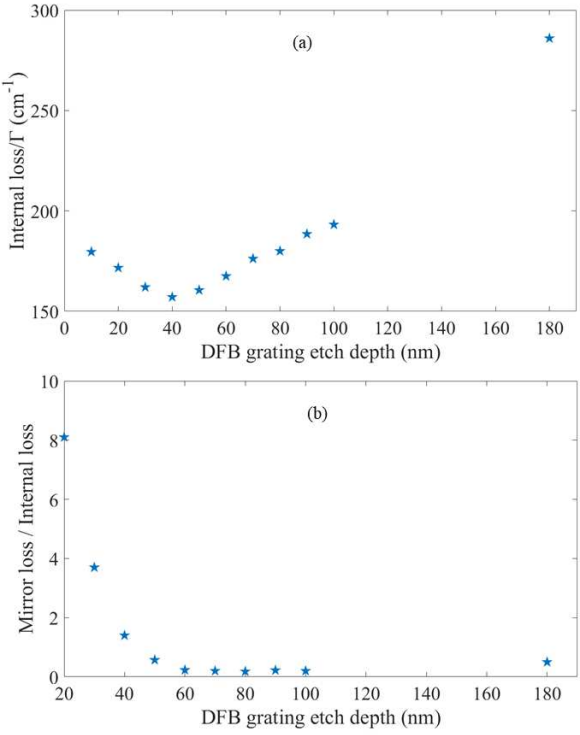

Figure 3.6: a) Calculated ratio of the simulated internal loss to the simulated confinement factor for a BCB thickness of 20 nm on the 400 nm silicon platform. b) Ratio of the calculated mirror loss to the calculated internal loss for a 200 μm long cavity.

fabricated devices (as discussed in section 3.1). As can be seen in Figure 3.6(b), there is an increase in the mirror loss for the 180 nm etch depth since the optical mode is strongly confined to the III-V waveguide and has a lower overlap with the underlying DFB grating.

In order to illustrate the behavior of the fundamental optical mode inside the cavity of a heterogeneously integrated DFB laser, the optical mode properties of the cavity for two different etch depths in the underlying silicon waveguide are simulated using the mode matching method. Figure 3.7 depicts the vertical cross-

section of the cavity (including the III-V epitaxial layers and the silicon waveguide underneath) where the fundamental optical mode profile is calculated. The InGaAsP epitaxial structure is used in this simulation of which the details are given in Table 3.2. In the following, we first discuss how to push down the optical mode into the silicon waveguide underneath by using a shallow etch DFB grating, and then we compare the simulation results with the previously fabricated lasers using a deep etch configuration.
In Figure 3.7(a) the fundamental mode for a cavity with a shallow etch (20 nm) silicon waveguide is calculated. Assuming a perfect first order DFB grating, a silicon waveguide configuration with 20 nm etch depth approximately corresponds to 40 nm surface etched DFB grating (in other words the average etch depth of the DFB grating is inserted in the modeling of the cavity cross-section). The width of the silicon waveguide and that of the III-V mesa is 2 μm. Based on the simulation

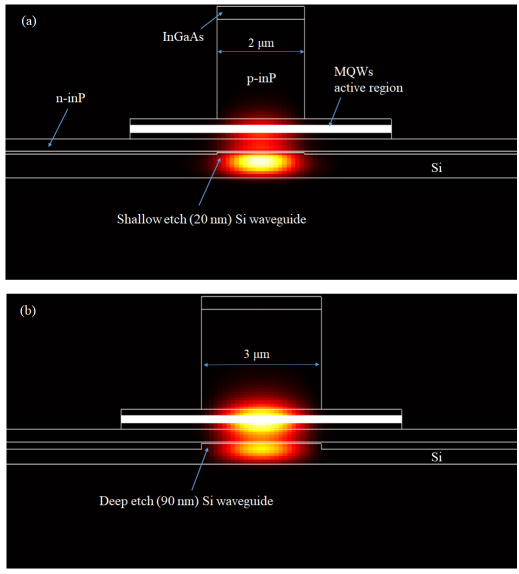

Figure 3.7: Profile of the fundamental optical mode in the III-V/Si cross-section. a) Mode profile in the laser cross-section with a shallow etch silicon waveguide and a narrow mesa. b) Mode profile in the laser cross-section with a deep etch silicon waveguide and a wide mesa.

results, the confinement factor of the optical mode in the active region is around 3.5% and the mode is strongly confined to the silicon waveguide. The calculated intrinsic (internal) loss of the cavity is 5.58 cm^{-1}.
Figure 3.7(b) depicts the optical mode profile in the laser cross-section with a 180 nm deep etch silicon waveguide and a wide mesa in which both III-V mesa and silicon waveguide are 3 µm wide. Indeed, this configuration represents the laser structures discussed in the previous section. Based on the simulation results, the optical mode is predominantly confined to the III-V waveguide with a confinement factor of around 6.7%. The calculated internal loss of the cavity in this case is found to be 19.2 cm^{-1}, which is in a good agreement with the characterization results of

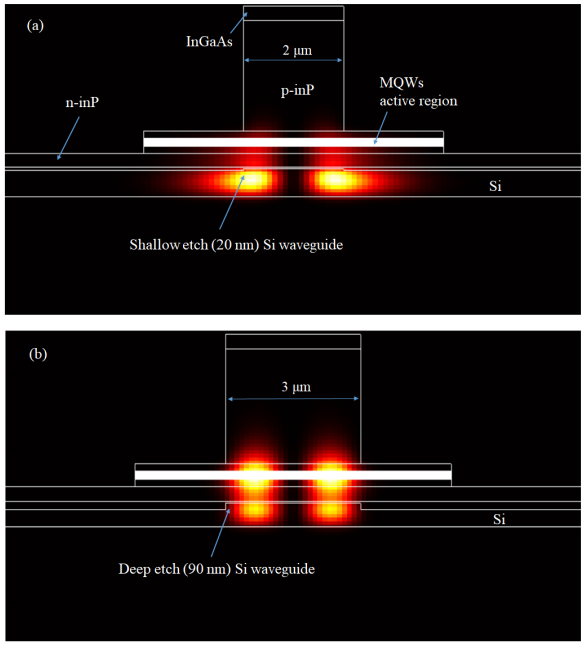

Figure 3.8: Profile of the higher order optical mode in the III-V/Si cross-section. a) Mode profile in the laser cross-section with a shallow etch silicon waveguide and a narrow mesa. b) Mode profile in the laser cross-section with a deep etch silicon waveguide and a wide mesa.

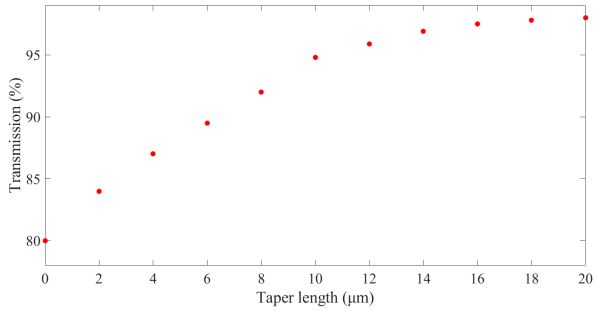

Figure 3.9: FDTD simulation of the coupling efficiency of the shallow etched III-V/Si waveguide to the silicon waveguide using a short taper configuration.

the internal loss given in the section 3.1.1.
Comparing the simulation results for the two cases shown in Figure 3.7, it is obvious how a shallow etch grating leads to a significant decrease in the internal loss of the cavity. In addition, we also use a narrower silicon waveguide in order to reduce the possibility of higher order mode propagation in the cavity. As it is shown in Figure 3.8(a), for a narrower silicon waveguide the higher order mode is more extended in the silicon slab while in the configuration with a wide waveguide (Figure 3.8(b)) the position of the higher order mode is completely inside the silicon rib waveguide which can result in a multimode operation of DFB lasers. This is one of the challenges that we have observed in some of the fabricated DFB lasers using a wide deeply etched silicon waveguide.

Finally, we investigate the required taper configuration for the shallow etch case and compare the results with the structure shown in Figure 3.1. Choosing a 20 nm shallow etched silicon waveguide (as shown in Figure 3.7) and a BCB thickness of 20 nm, the coupling efficiency of the III-V/Si waveguide to the silicon waveguide is calculated. Figure 3.9 depicts the simulated transmission of the taper structure as a function of the taper length using Lumerical FDTD. As shown in Figure 3.9, by incorporating a 10 μm linear taper, over 95% transmission is achieved for the fundamental optical mode. This substantial decrease in the taper length (compared to the long taper configuration used in earlier devices described in Figure 3.1) is the result of using a shallow etched silicon waveguide.

3.3 Integrated lasers realized by bonding

In this section the fabrication process flow of the adhesive bonding technique is explained. As we briefly mentioned in the first chapter, first the SOI circuit as well as the III-V epitaxial stack are prepared. Then, by using a wafer bonding tool, the III-V stack is bonded to the SOI chip or wafer. After that, the post-processing is carried out to fabricate laser structures such as lasers. In the following the fabrication process is described in more detail.

3.3.1 SOI Fabrication

Lithography is the main step in preparing a SOI circuit. It is a process of transferring information from a designed mask to a substrate. In order to perform this processing step, the target material (e.g the SOI wafer or sample) coated with a specific resist is exposed by a form of radiation. Then, based on the type of the lithography, the pattern can be made after a proper development process. There are several techniques for patterning in the semiconductor industry. Optical lithography (or photolithography) is the most common technique used for mass fabrication in CMOS manufacturing, which can be classified based on the wavelength of the light used in the process. The minimum feature size is determined by the wavelength of the light used to expose the photoresist.
In the previous work on the heterogeneously integrated DFB lasers (discussed in previous sections) in the Photonics Research Group, the DFB grating and rib waveguides were patterned on a 400 nm thick silicon device layer using 193 nm deep UV lithography and a 180 nm deep dry etching. However, there was no possibility to define a specific shallow etch configuration in these runs for our approach of optimizing the III-V-on-Si DFB lasers using a shallow etch DFB grating. In addition, the slow turn-around time of these runs has been a major challenge in this work. In this regard, we use electron beam (e-beam) lithography to pattern SOI samples. In the following we discuss this lithography process in more detail.

3.3.1.1 Electron-beam lithography

E-beam lithography is a powerful technique for making nanostructures that are too small to fabricate with conventional optical lithography. In this technique, a focused electron beam is used to expose a sample coated with a thin layer of e-beam sensitive resist. The exposed resist gets chemically modified via the direct writing of structures by moving the focused electron beam. Similar to the optical lithography,

e-beam lithography also utilizes positive or negative resists. The positive e-beam resist creates an image that is the same as the pattern drawn by the e-beam. In other words, by exposing the positive e-beam resist, it undergoes bond breaking and becomes soluble in the developer solution. On the other hand, non-exposed areas will be soluble in case of the negative e-beam resist.

In order to pattern samples, we use a Raith-VOYAGER e-beam lithography system in our cleanroom at UGent. The important system features include operation with acceleration voltages up to 50 KV, maximum write field size of 500 μm and automatic system setup (autofocus/autostigmator/automatic stage adjustment with mark recognition/automatic write-field alignment). The system can be used to pattern complex structures on masks of up to 7-inch diameter and wafers of up to 8-inch diameter, using direct-write procedures with ultra-high resolution in the nanometer range [8, 9].

The Raith-VOYAGER e-beam lithography system has two different writing modes, conventional writing and Fixed Beam Moving Stage (FBMS) writing. In conventional e-beam writing, the stage remains stationary and the electron beam is deflected. Therefore, the size of the writing field depends on the maximum deflection angle of the e-beam. This e-beam lithography tool has a maximum write field of 500×500 μm^2. Thus, the stage has to be moved beyond each write field, which results in alignment inaccuracies at the boundary of the writing field. For structures longer than one write field a misalignment at the boundary can occur which is often called a stitching error. The stitching errors result in higher optical waveguide losses and can produce reflections. It is critical to reduce the number of stitching errors in order to avoid performance degradation. Raith-Voyager overcomes this issue by providing a solution for writing long waveguides with a novel continuous writing mode, called FBMS. This stitching-error free mode can be used for writing of up to several cm long paths of arbitrary curvature, including tapered paths [8].

The SOI sample with a proper size (depending on the size of the lithography mask to be patterned) is cleaved from an SOI wafer. The protective photoresist layer on top of the sample is removed and the sample is loaded in the Tepla barrel etcher for 15 min O_2 plasma cleaning. After that, an AR-P 6200.09 (CSAR 62) resist is spin coated. CSAR 62 is a new positive ebeam resist with excellent structural resolution and comparable broad process windows to other resists. In addition, it has superior performance in terms of contrast and sensitivity when developed in AR 600-546. AR-P 6200.09 is spin coated at 1500 rpm for 60 s. Then, the sample is baked at 150 °C for 1 min. Subsequently, a water-soluble conductive polymer Electra 92 (AR-PC 5090), which is compatible with CSAR 62 is spin coated on top of the AR-P 6200.09 layer. This is beneficial in reducing the effect of charging and is particularly important when patterning dielectrics as charge can easily accumulate at a point which defocuses the e-beam and degrades the writing process. Electra 92 is spin coated at 2000 rpm for 60 s and the sample is then baked for 2 min at 90 °C.

The sample is now ready to be loaded in the e-beam lithography tool for exposure. In this work, the e-beam exposure is carried out in two steps. First, the shallow etch part of the design is exposed followed by the development and etching to pattern the shallow etch DFB grating. Then, the sample is again prepared for being exposed to pattern the 180 nm deep etch silicon waveguide and grating couplers. In the following, the details of the development and etching of the sample are explained.

3.3.1.2 Development and dry etching

After the completion of the first e-beam exposure, the sample is immersed in DI-water for 30 s to remove Electra 92. Then, it is developed in n-amylacetate for 1 min followed by an instantaneous immersion in IPA for 1 min. After the completion of the development, the pattern in the resist has been formed and can be transferred to silicon. To this end, a dry etching process called Reactive Ion Etching (RIE) is used. It is carried out in an Advanced Vacuum Vision 320 RIE tool equipped with 13.56 MHz RF excitation and a cooling system to maintain the sample plate temperature at 20 °C.

A mixture of CF_4, H_2 and SF_6 is used, which is inspired by an in-house developed etching process for silicon nitride and germanium. A power of 210 W, a pressure of 20 mTorr optimized together with the gas flow parameters (100 sccm for CF_4, 7 sccm for H_2 and 3 sccm for SF_6) are used. The etch rate is around 70-80 nm per minute for the silicon. However, due to the variation of the etching rate, some test structures are included in the design to track the etching by means of a thin-film measurement tool (Filmetrics) before and after etching.

After the completion of the etching (with the etch depth of 20-60 nm for the shallow etch part) in this step, the sample is loaded in the metalization tool to put a thin layer of gold on top of the alignment markers for the second exposure. Finally, the resist is removed in the RIE chamber with O_2 plasma or using the Tepla barrel etcher for 15 min O_2 plasma cleaning.

In order to perform the second exposure for patterning the silicon waveguide and grating couplers, the same procedure of preparing the SOI sample (i.e the ebeam resist coating followed by the spin coating of Electra-92) is carried out and the sample is loaded in the e-beam lithography tool for the second exposure. The exposed sample then can be developed with the same recipe used for the first step followed by RIE etching. Finally, the ebeam resist is removed after 15 min O_2 plasma cleaning in the Tepla barrel etcher and the SOI sample is ready for the bonding process. Figure 3.10 depicts the fabricated SOI sample in which the first patterning step including the DFB grating as well as the second patterning step containing the silicon waveguide and grating couplers are shown.

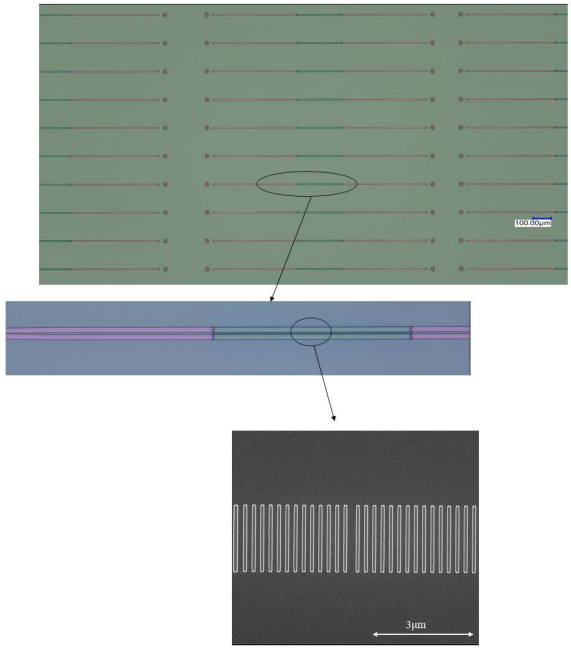

Figure 3.10: The fabricated SOI circuit using the ebeam lithography. The insets depict the silicon waveguide and the surface etched DFB grating, respectively.

3.3.2 Bonding Process

After the preparation of the SOI sample, the III-V die has to be prepared for the bonding process. In this work we use a III-V die of which the size depends on the corresponding design patterned on the SOI sample. As described in Tables 3.1 and 3.2, two sacrificial layers are grown on each side of the bonding compatible III-V epi. The first sacrificial layer is a thin film of InP which is selectively removed by pure HCl. The second sacrificial layer is an InGaAs thin film which can be etched away by a piranha (H_2SO_4:H_2O_2:H_2O solution with the corresponding ration of 1:1:18) solution. After removing the second sacrificial layer, the n-InP contact layer is exposed. In order to have a better adhesion to the SOI sample, a thin layer of SiO_2 (5 to 10 nm) is deposited using a Plasma-enhanced chemical vapor deposition

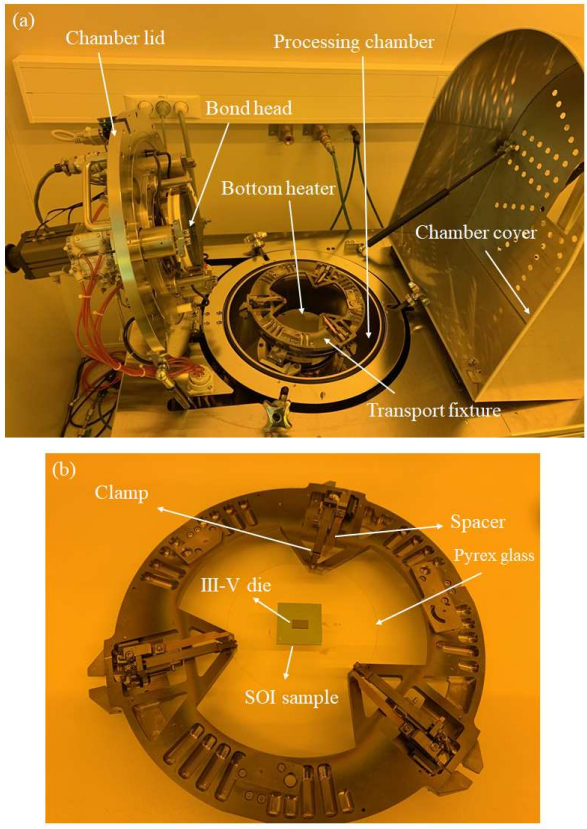

Figure 3.11: Illustration of the machine bonding. a) The basic components of the Süss Microtec ELAN CB6L wafer bonder. b) The transport fixture for handling 100 mm diameter wafers with samples to be bonded on top.

(PECVD) process. At this stage, the III-V die is ready for the bonding process.

In order to bond the III-V die to the SOI sample, a thin layer of a diluted BCB solution (1 volume of Dow Chemical's Cyclotene 3022-35 solution mixed with 10 volumes of Mesitylene) is spin coated on the SOI sample. The spin coating is performed in two steps at 500 RPM and then at 3000 RPM in order to have a good

planarization. The SOI sample is then baked for 15 min at 150 °C to let mesitylene evaporate. After that, the substrate is slowly cooled down and can be taken off at 70 °C.
Figure 3.11(a) depicts the Suss MicroTec ELAN CB6L wafer bonding machine. The interior of the bonding machine includes a top and bottom bonding head to apply force and a transport fixture where the samples can be mounted. First, the III-V die is flipped on the SOI sample to cover the patterned design on the SOI, and then the SOI substrate is mounted on a carrier wafer made of Pyrex glass. After that, the carrier wafer is placed on the transport fixture (Figure 3.11(b)) and another Pyrex glass is placed on top of the sample which is fixed by clamping the carrier wafers. The transport fixture can then be loaded into the bonding machine.
After loading the fixture into the processing chamber, the chamber lid is closed accurately and the chamber is pumped-down and heated to 150 °C with a ramp of 15 °C/min for 10 min. The applied force per area of the III-V die is set to 400 kPa. After maintaining the pressure on the dies for 10 min at 150 °C, the temperature is increased up to 280 °C, with a ramp of 1.5 °C/min. Upon reaching 280 °C, the dies are kept at this temperature for 60 min in a nitrogen atmosphere to cure the DVS-BCB layer. After curing, the bonded samples are cooled down (at 6-10 °C/min) and unloaded from the processing chamber. The next step is to remove the thick InP substrate.

3.3.3 III-V Process flow

A brief overview of the III-V process flow is represented in Figure 3.12. Each step will be discussed in more detail in the following sections.

3.3.3.1 Substrate and sacrificial layers removal

Figure 3.13 (a) depicts the sample after the completion of the bonding process. The InP substrate, which is a few hundreds of micron thick, is removed by using a wet etch process. In order to selectively etch the substrate, a 1:3 H_2O:HCl solution is used at the temperature of 40-50 °C. The heating up of the solution is critical for having a uniform removal of the substrate, without creating 'ears' at the edges of the die [6]. After around 10-15 min, the substrate is completely etched and the first sacrificial layer, which is a thin film of InGaAs, is exposed. The InGaAs thin film is removed after immersion in a Piranha solution for around 1 min. After that, the 100 nm InP sacrificial layer is removed using a pure HCl solution for 5-10 sec. The etching process will finish on the InGaAs contact layer (Figure 3.13(b)).

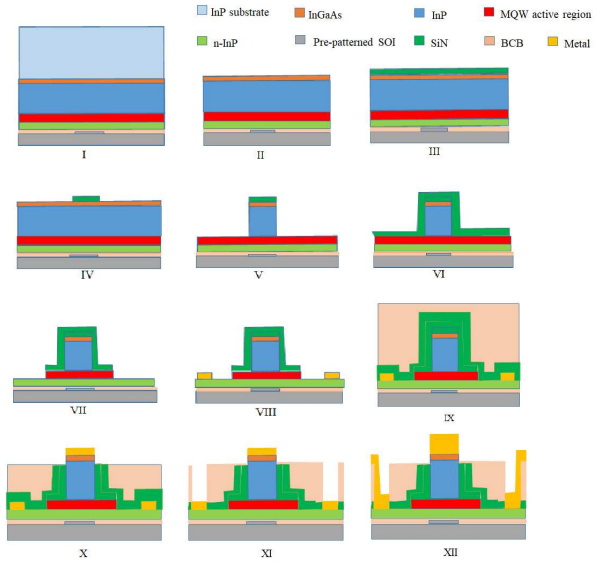

Figure 3.12: III-V process flow. (I) After bonding process. (II) After substrate removal. (III) SiNx deposition as a hard mask for the III-V mesa definition. (IV) Mesa is defined using an optical lithography. (V) Dry etching of the III-V mesa. (VI) Deposition of the SiNx as a sidewall protection layer as well as a hard mask for Wide active region patterning. (VII) Etching of the active region to expose the n-type InP contact layer. (VIII) N-contact metallization. (IX) Passivation of the structures using thick layers of SiNx and BCB. (X) Etching back the BCB and SiNx to expose the p-contact and p-contact metallization. (XI) Via opening, and (XII) Final metallization.

3.3.3.2 Mesa definition

In this step, the III-V mesa (waveguide) is defined for the further processing. The III-V mesa definition is one of the most critical steps of the fabrication of heterogeneously integrated lasers realized by bonding. Since the grating and the waveguides are already patterned on the SOI sample, a high alignment accuracy is needed for the demonstration of high performance devices. Specifically in case of a high efficiency DFB laser, the alignment accuracy has to be better than 200 nm. In order to define the III-V mesa, we first deposit a thin layer of SiO_2 (10 nm thick layer for providing a better adhesion) followed by 200 nm thick SiNx as a

hard mask. This deposition is done by PECVD at 270 °C. After that, an optical lithography is done using a positive resist. In our cleanroom we use MIR-701 which is a high resolution photoresist optimized for dry etching of sub-µm patterns.

After the lithography, the sample is developed in a diluted AZ 726 MIF Developer (MIF:H_2O 3:1). Tracking the color change of the sample as well as a microscope check of the sidewalls and taper tips of structures are necessary to make sure the lithography process is done correctly. After the development, the photoresist pattern

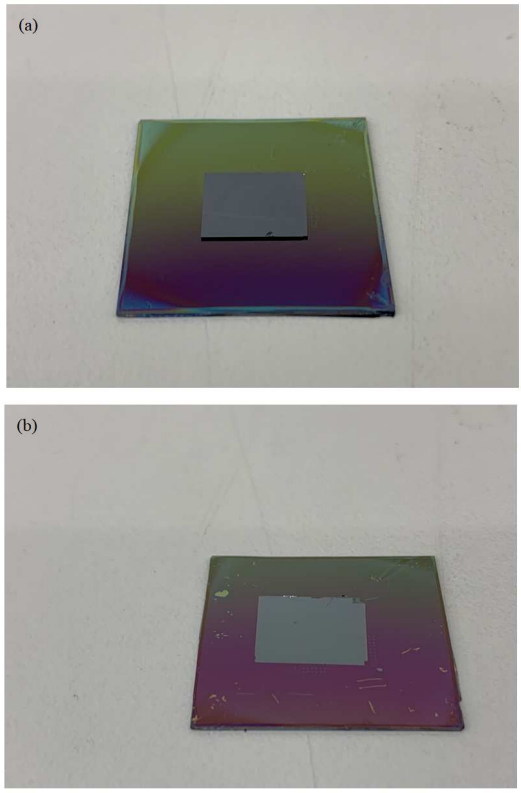

Figure 3.13: Photograph of a bonded sample. a) Before substrate removal. b) After substrate removal using a wet etching process.

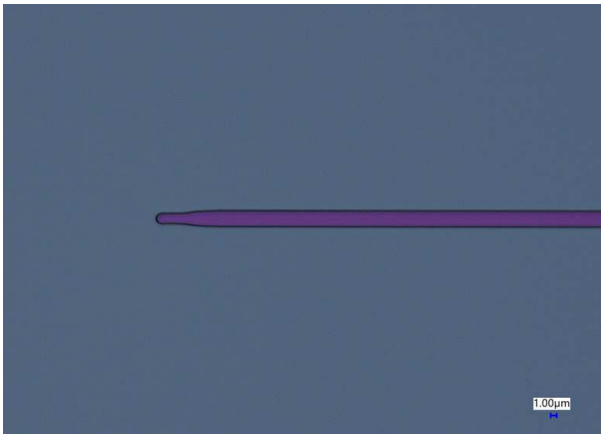

Figure 3.14: The mesa definition step using optical lithography. The mesa is defined by patterning the high resolution photoresist MIR-701 followed by the etching of SiNx

is created as shown in Figure 3.14. The sample is then loaded in the RIE tool to etch away the SiNx everywhere while the photoresist acts as a soft mask to transfer the pattern to the SiNx underneath. After etching of the SiNx, the photoresist is removed using acetone and IPA. The sample is rinsed in DI water followed by 30 sec of soft resist removal with RIE. At this stage, the top InGaAs contact layer is exposed except where the SiNx hard mask is patterned.

3.3.3.3 Mesa etching

In this step, a dry etching process is used to pattern the III-V mesa. After defining the mesa, the sample is loaded into the Inductively Coupled Plasma (ICP) etcher. The InGaAs contact layer is etched with an etch rate of around 40 nm per cycle using an in-house developed etching recipe for III-V etching. Next, we can use two approaches for etching of the thick InP cladding layer.
The first approach is to first etch a few hundreds nm into the InP layer using ICP etching and continue with wet etching at room temperature using a HCl:H_2O 1:1 solution. This solution will etch selectively the thick InP layer with a negative slope with an etch rate of 100 nm/min. For the wet etching process, the mesa is oriented along the [100] crystal axis and a V-shaped waveguide configuration is created (Figure 3.15(b)). This V-shaped mesa configuration leads to an effective optical

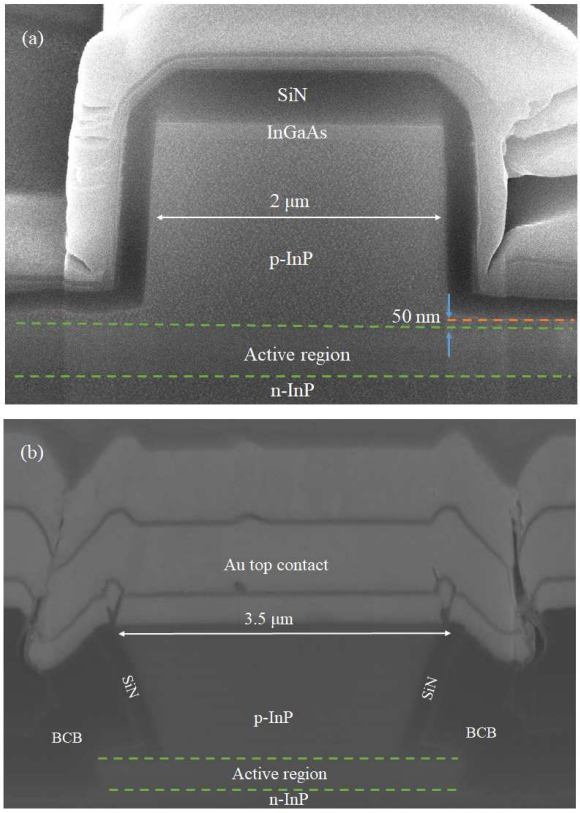

Figure 3.15: FIB cross-section of the fabricated devices. a) ICP dry etching of the mesa reulting in a rectangular waveguide. b) A V-shaped waveguide configuration using the combination of ICP dry etching and wet etching with a HCl:H_2O 1:1 solution.

and electrical confinement as well as narrow taper-tips on the bottom of the mesa, consequently coupling light more efficiently to the silicon waveguide underneath.

The second approach which is implemented in this work, uses the dry etching process to fully etch the InP cladding layer. Unlike the wet etching process, the ICP etching is anisotropic and results in a rectangular waveguide. In addition, it

improves the sidewall roughness of the III-V waveguide compared to the wet etching process. Figure 3.15 depicts the final shapes of the III-V mesa using the two etching processes. Figure 3.15 (a) represents a fully etched III-V mesa (the dry etching of the InGaAs and InP layers), resulting in a rectangular waveguide. However, as can be observed in Figure 3.15(a), the InP cladding layer is not completely etched and a thin film (with the thickness of a few tens of nm) of InP layer is left on top of the MQW active region. This can be beneficial in leaving the surface of the active region intact and decreasing the potential surface recombination, specifically in the case of the Al-containing active regions.

3.3.3.4 Active region patterning

In this step, the sample is loaded in the PECVD tool at 270 °C and a 200 nm thick mixed frequency SiNx is deposited. There are two purposes to deposit the SiNx layer in this step. First, to protect the sidewall of the III-V waveguide, specifically to prevent the p-InGaAs layer from being attacked in the piranha solution used in the following steps. Second, as will be discussed below, it can be used as a hard mask for patterning a wide active region.

Depending on the design, the active region can be patterned in different ways. In case of a narrow active region, the sample is loaded in the RIE chamber to etch away the SiNx deposited in the previous step. Careful attention has to be paid to avoid over etching the SiNx from the top of the mesa. It can be helpful to load a dummy silicon sample whenever a layer of SiNx is deposited. Thus, the thickness of the SiNx layer can be tracked before and after etching. Since the etching is anisotropic, the sidewall of the mesa is protected with SiNx while everywhere else the SiNx is etched. After that, the active region is patterned using ICP dry etching. The etch rate of InGaAsP and InGaAlAs MQW active regions in the ICP tool is around 30-40 nm/cycle and 10-15 nm/cycle, respectively. Figure 3.16(a) depicts the etching of a narrow active region. It is very critical to etch the active region completely using ICP dry etching since it is not a selective etching process and over etching of the active region will attack the thin n-InP layer underneath due to the faster etch rate of the ICP etching in InP. In order to prevent this, a wet etching is used for removing the very thin remaining layer of the active region. Based on the MQWs active region, different solutions are used. For the InGaAsP samples, an isotropic Piranha solution (H_2SO_4:H_2O_2:H_2O 1:1:18) is used to completely remove the active layer on top of the n-InP contact layer. Regarding the InGaAlAs active layer, a H_3PO_4:H_2O_2:H_2O 1:1:20 solution is used to etch the layer completely. As can be seen, an undercut during the wet etching occurs, which can be a major issue for a narrow mesa, specifically in the taper tip.

In order to decrease the scattering losses by keeping the optical mode far away from the rough sidewalls of the active region caused by the wet etching process, a

wide MQW active region is used. For the wide active region patterning, an optical lithography is carried out after SiNx deposition. By using an AZ 5214 positive resist with a thickness of around 2 µm, followed by the development, the active region is patterned. After that, the SiNx is etched using RIE dry etching. Subsequently, the resist is removed using acetone, IPA, and water. At this stage, the sample can be loaded in the ICP tool to etch down the active region. By tracking the etch rate and the height of the III-V mesa before and after etching, we will stop the dry etching before exposing the n-InP contact layer. Then, depending on the active region stack, a proper wet etching process can be used to etch away the residual active region. Figure 3.16 (b) depicts the wide active region structure patterned with SiNx hard

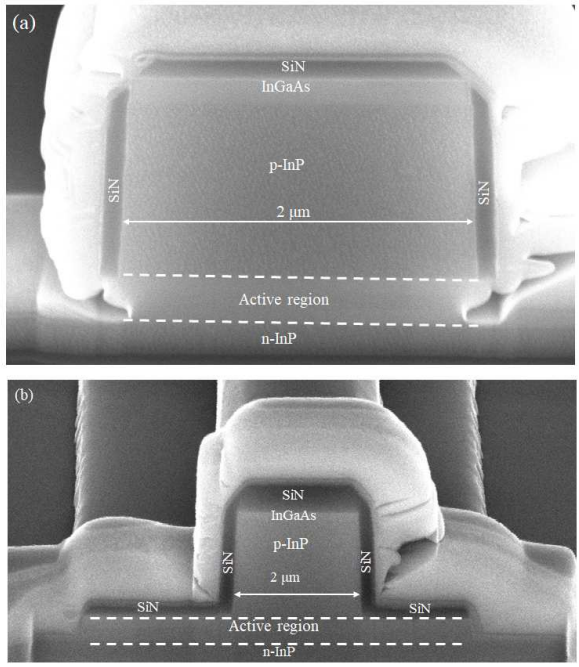

Figure 3.16: Active region patterning. a)A narrow active region which is etched through using the ICP dry etching and a proper piranha solution. b) A wide active region defined by the deposition of SiNx hard mask followed by an optical lithography.

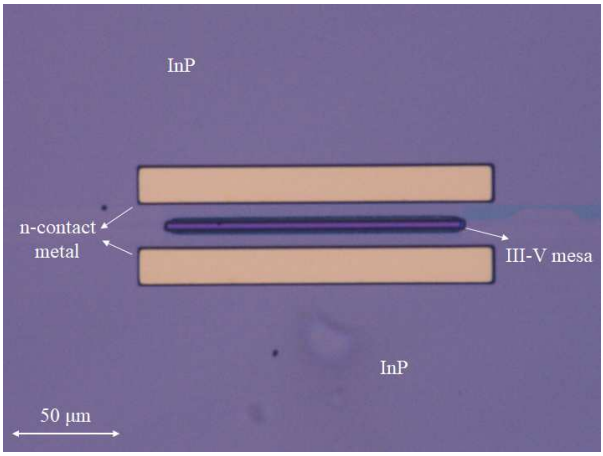

Figure 3.17: N-contact metallization after the lift-off process. A 30 nm/20 nm/50 nm Ni/Ge/Au metal layer stack to form an ohmic contact with n-InP and an extra 40 nm/100 nm Ti/Au is deposited.

mask.

3.3.3.5 N-contact metallization

After etching the active region, the sample is ready for the n-contact metallization. In order to improve the metal contact quality, which will result in a lower differential resistance, the metallization needs to be performed immediately. To this end, an image reversal lithography using a thick (3.5 µm) layer of Ti 35E photoresist is performed. In order to open the area where the metal contact will sit on, two types of optical exposure are carried out.

The first structure-defining exposure is done with a photo mask. Due to the photochemistry of the Ti 35E phtoresist, nitrogen is released during the first exposure. Thus, it is important to allow the nitrogen formed during the exposure to outgas before the reversal baking step to avoid the formation of bubbles in the resist pattern. This required delay or waiting time depends on the resist and the thickness used in the process. In our work, we wait around 20 min after the first esposure and then the sample is baked at 125 °C for 3 min. Finally, a flood exposure is done which is the last step in the image reversal process. To have a better opening into the thick resist profile, the flood exposure is carried out in two steps. The photoresist is

developed in a 1:3 H_2O: AZ 400 diluted developer. Then a 30 seconds RIE oxygen plasma cleaning is performed to remove the remaining resist in the recesses. In order to remove the native oxides and ensure a good ohmic contact, the sample is dipped in a 1:1:20 H_2SO_4: H_2O_2: H_2O Piranha etchant for 5 seconds. In addition, a short dip in a highly dilute solution of HCl:H_2O 1:40 can be beneficial in having a better ohmic contact. After that, the sample is immediately loaded in a Leybold Univex thermal evaporation/sputtering system to prevent the InP from oxidizing again. A 30 nm/20 nm/50 nm Ni/Ge/Au metal layer stack to form an ohmic contact with n-InP and an extra 40 nm/100 nm Ti/Au is deposited. After that, the lift-off process is carried out by immersing the sample in a bath of acetone to remove the unwanted metal. Figure 3.17 gives a microscope image of a device on the chip after the lift-off process.

3.3.3.6 Island definition and passivation

After n-metal contact deposition, the individual active structures (here different laser structures) need to be electrically isolated from each other. Thus, wide photoresist masks are separately patterned on each laser to cover the whole III-V mesa as well as the n-contacts on both sides of the laser. Since the III-V mesa in this step is relatively high (more than 2 µm), a thick resist patterning using an AZ 10XT positive photoresist is carried out. After developing the resist, the sample is shortly (few seconds) dipped in an HCl (37%) solution to etch the thin n-InP layer. The etching process of the InP thin film in a pure HCl etchant is extremely fast and is usually accompanied by the formation of micro-bubbles. The sample has to be rinsed with DI water immediately after the disappearance of bubbles. The other alternative is using a HCl:H_2O 1:1 solution for 2-3 min to etch n-InP layer. As depicted in Figure 3.18, all III-V layers are etched in this step and the underlying SOI structures are visible.
In the next step, the sample is loaded in the PECVD tool to deposit 600 nm mixed frequency SiNx at 270 °C. Then the devices are planarized using a thick DVS-BCB layer. To this end, a pure Cyclotene 3022-57 DVS-BCB resin is spin coated on the sample at 2000 rpm for 40 seconds. After that a BCB full cure procedure is applied at 280 °C using an Unitemp oven. The resulting DVS-BCB passivation layer is around 7 µm thick with about 80-90 nm topography.

3.3.3.7 P-contact metallization

In order to deposit the p-contact metal, the top InGaAs contact layer has to be exposed. Thus, we need to etch back the BCB and SiNx. An RIE dry etch with a 5 sccm:50 sccm SF_6:O_2 mixture is used to thin down the thick DVS-BCB layer.

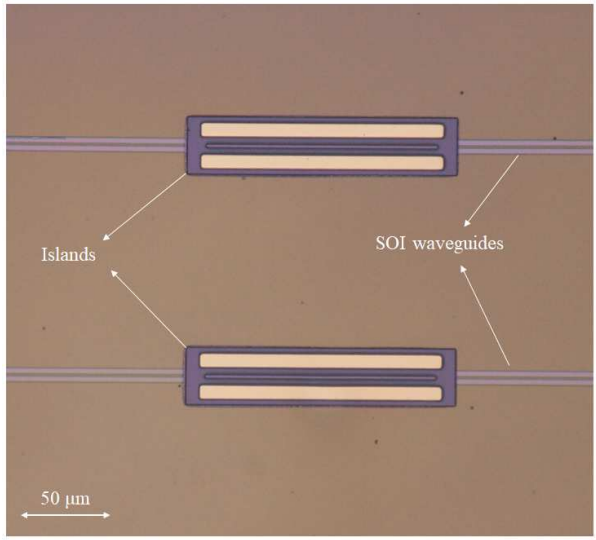

Figure 3.18: Island definition using an optical lithography followed by wet etching process to remove the n-InP in order to electrically isolate the active components.

The etch rate for the BCB under this recipe is around 300 nm/min and after almost 16 min the SiNx layer is exposed. Then, in the same tool we etch back the SiNx layer with another recipe (80 sccm:3 sccm:7 sccm CF_4:SF_6:H_2) to expose the top p-InGaAs contact layer. After the exposure of the p-InGaAs layer, an image reversal lithography using a 3 µm thick Ti35E photoresist layer (spin-coated at a speed of 4000 rpm for 40 seconds) is carried out to define the p-contact pattern. Then, the sample is developed followed by removing the residual photoresist using O2 plasma in the RIE chamber. Subsequently, the sample is shortly (a few seconds) dipped in a H_2SO_4:H_2O_2:H_2O 1:1:20 solution to remove the native oxide. At this stage the sample is ready for the p-contact metal deposition.
The sample is dried after the immersion and is immediately loaded into a Leybold Univex system for metal deposition. A 40nm-thick layer of Titanium is sputtered on the sample, followed by the thermal evaporation of a 150 nm-thick layer of gold. After the metal deposition, the sample is dipped into a bath of acetone for the lift-off process. Once the lift-off is completed, the sample is rinsed and dried. Figure 3.19 represents the top view microscope image of the chip where two laser structures are shown after the deposition of the p-contact metal. The n-contact and

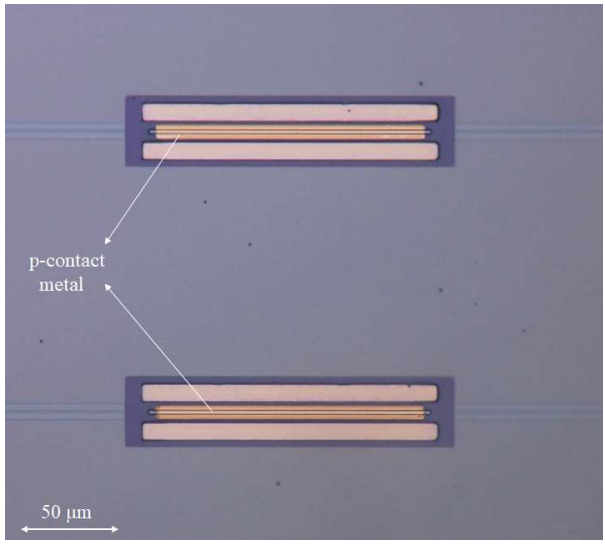

Figure 3.19: P-contact metallization after the lift-off process. A 40nm-thick layer of Titanium is sputtered on the sample, followed by the thermal evaporation of a 150 nm-thick layer of gold.

p-contact metal layers are isolated by the SiNx and DVS-BCB passivation layers to prevent a potential short circuit.

3.3.3.8 Final metallization

Once the p-contact metallization is completed, another image reversal lithography using a 4 µm thick Ti35E photoresist layer (spin-coated at a speed of 2500 rpm for 40 seconds) is carried out to define the via opening pattern. After that, the sample is loaded into the RIE chamber to etch away the whole DVS-BCB and SiNx layers in order to expose the n-contact metal deposited earlier.
Once the vias are completely open, the sample is rinsed with acetone, IPA and DI water. Finally, the last image reversal lithography using a 4 µm thick Ti35E photoresist layer (spin-coated at a speed of 2500 rpm for 40 seconds) is carried out to define the pattern of the final metal pads. The metallization is performed inside the Leybold Univex system using a 200 nm-thick layer of titanium, followed by

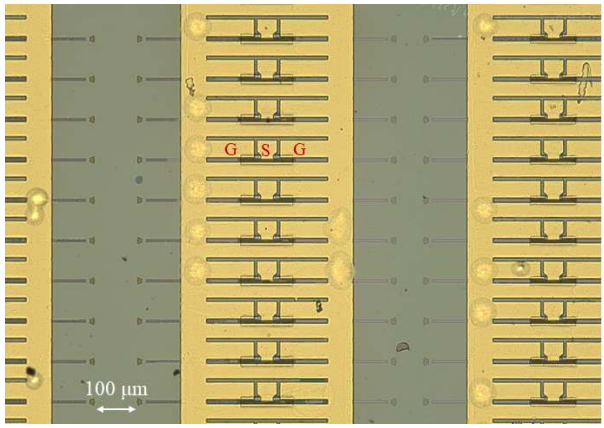

Figure 3.20: Final pad metallization. The metallization is performed in the dedicated tool, using a 200 nm-thick layer of titanium, followed by thermal evaporation of an 800 nm-thick layer of gold.

thermal evaporation of an 800 nm-thick layer of gold. Figure 3.20 depicts the array of lasers on the chip after the lift-off process.

3.4 Conclusion

This chapter discussed the design and process flow of the heterogeneously integrated DFB lasers on the silicon waveguide circuit. First, an overview of the earlier III-V-on-Si DFB lasers developed in the Photonics Research Group was given. Then, we discussed some ideas how to improve the performance of these lasers. It is described that by pushing down the optical mode into the silicon waveguide using a shallow etched DFB grating, the internal loss of the cavity decreases. In addition, due to a high confinement of the fundamental optical mode within the silicon waveguide, the required taper length for converting the hybrid mode to a silicon rib waveguide mode is decreased more than an order of magnitude. Regarding the fabrication of the heterogeneously integrated DFB lasers, the SOI circuit is patterned using e-beam lithography and the bonding process is carried out by means of a Süss Microtec ELAN CB6L wafer bonder. After the completion of the bonding process, the standard process flow of the III-V epitaxial layer is described.

Bibliography

[1] G.-H. Duan, C. Jany, A. Le Liepvre, A. Accard, M. Lamponi, D. Make, P. Kaspar, G. Levaufre, N. Girard, F. Lelarge, *et al.*, "Hybrid III–V on Silicon Lasers for Photonic Integrated Circuits on Silicon," *IEEE Journal of selected topics in quantum electronics*, vol. 20, no. 4, pp. 158–170, 2014.

[2] S. Keyvaninia, S. Verstuyft, L. Van Landschoot, F. Lelarge, G.-H. Duan, S. Messaoudene, J. Fedeli, T. De Vries, B. Smalbrugge, E. Geluk, *et al.*, "Heterogeneously integrated III-V/silicon distributed feedback lasers," *Optics letters*, vol. 38, no. 24, pp. 5434–5437, 2013.

[3] A. R. Adams, M. Asada, Y. Suematsu, and S. Arai, "The temperature dependence of the efficiency and threshold current of $In_{1-x}Ga_xAs_yP_{1-y}$ lasers related to intervalence band absorption," *Japanese Journal of Applied Physics*, vol. 19, no. 10, p. L621, 1980.

[4] I. P. Marko, C. A. Broderick, S. Jin, P. Ludewig, W. Stolz, K. Volz, J. M. Rorison, E. P. O'Reilly, and S. J. Sweeney, "Optical gain in GaAsBi/GaAs quantum well diode lasers," *Scientific reports*, vol. 6, no. 1, pp. 1–10, 2016.

[5] L. Tiemeijer, P. Thijs, J. Binsma, and T. Dongen, "Direct measurement of the transparency current and valence band effective masses in tensile and compressively strained ingaas/inp multiple quantum-well laser amplifiers," *Applied physics letters*, vol. 60, no. 5, pp. 554–556, 1992.

[6] A. Abbasi, *High speed directly modulated III-V-on-silicon DFB lasers*. PhD thesis, Ghent University, 2016.

[7] G. Shtengel, D. Ackerman, P. Morton, E. Flynn, and M. Hybertsen, "Impedance-corrected carrier lifetime measurements in semiconductor lasers," *Applied physics letters*, vol. 67, no. 11, pp. 1506–1508, 1995.

[8] S. Kumari, *GaAs VCSEL integration on SiN waveguide circuits: design, technology and devices*. PhD thesis, Ghent University, 2017.

[9] "https://www.raith.com/ product/voyager/."

4

Static and dynamic characterization of integrated distributed feedback lasers

4.1 Introduction 4-1
4.2 DFB lasers with symmetric output waveguide 4-2
4.2.1 III-V-on-Si DFB lasers with a narrow InGaAlAs MQW active region 4-3
4.2.2 III-V-on-Si DFB lasers with a wide InGaAsP MQW active region 4-6
4.3 III-V-on-Si DFB lasers with a wide InGaAsP MQW active region and a single output waveguide 4-14
4.3.1 Static characteristics 4-16
4.3.2 Noise characteristics 4-20
4.3.3 Dynamic characteristics 4-22
4.4 Conclusion 4-23

4.1 Introduction

In the following sections, the experimental results of the short cavity heterogeneously integrated III-V-on-Silicon DFB lasers will be discussed. Using the short

cavity design as well as the fabrication procedure discussed in the previous chapter, we demonstrate here the results on improving the laser performance in terms of high wall-plug efficiency and low noise operation. A high wall-plug efficiency leads to a low electrical power consumption for the optical transmitter and requires typically also less power consuming cooling. This is especially important where many transmitters are present in a limited area (e.g., in datacenters).
Additionally, low noise semiconductor lasers with high output power are required in many applications such as coherent communications systems and LIDAR remote sensing. Low noise performance is characterised by low frequency-noise (or linewidth) and low relative-intensity noise (RIN). Regarding the coherent communications, the detection of the encoded signal on the phase of the laser light can be disturbed and an error will be detected if there are severe fluctuations in the phase of the laser light. These fluctuations known as phase noise can be described as an intrinsic linewidth of the laser. In a LIDAR system, a narrow intrinsic linewidth increases the coherence length of the laser light which results in boosting the detection range of the LIDAR system and makes the system less vulnerable to the speckle effect.
In the following, we report the experimental results achieved from three different runs. In section 4.2, we investigate DFB lasers with symmetric output power. The first chip in this section has been fabricated using an InGaAlAs MQW active region. In the second part of section 4.2, we study III-V-on-si DFB lasers using a wide InGaAsP MQW active region. After that, in order to increase the single facet output power, we demonstrate another generation of DFB lasers using an HR facet at one side of the cavity in section 4.3. Finally, this chapter ends with a conclusion including a comparison of the state of the art C-band III-V-on-silicon DFB lasers.

4.2 DFB lasers with symmetric output waveguide

In this section, we discuss the experimental results obtained on the characterization of the fabricated DFB lasers with the same output waveguide on each side of the cavity. We first fabricated some lasers with narrow active region configuration using InGaAlAs MQWs, of which the experimental results are discussed below. After that, we demonstrate another generation of III-V-on-Si DFB lasers using InGaAsP MQWs with a high wall-plug efficiency and low threshold current.

4.2.1 III-V-on-Si DFB lasers with a narrow InGaAlAs MQW active region

Fig. 4.1 shows the schematic of a heterogeneously integrated DFB laser on a pre-patterned SOI circuit. The SOI platform consists of a 400 nm thick Si device layer on a 2μm buried oxide (BOX) layer. The 200μm long cavity is determined by a 2μm wide, first order, quarter-wave shifted grating in the silicon with a 60 nm etch depth. The 60 nm etched silicon waveguide is then connected to a 180 nm etched silicon waveguide in which the 180 nm etched grating couplers are incorporated. In the III-V section, the epitaxial layer stack consists of a 200 nm thick highly-doped p-InGaAs contact layer, a 1.5 μm thick p-InP cladding layer, an InGaAlAs multi-quantum well (MQW) active region with 6 quantum wells surrounded by 75 nm thick separate confinement heterostructure (SCH) layers, and a n-InP contact layer with a thickness of 260 nm. The laser mesa is 2μm wide and consists of two short spot-size converters at the ends. More details on the III-V epitaxial structure can be found in Table 3.1.
As we discussed in the previous chapter, the key element in designing a short cavity III-V-on-Si DFB laser is to accurately analyze the optical mode profile in the III-V/Si cross-section. In order to make a short cavity, the mode has to be sufficiently confined to the active region to provide sufficient gain for lasing. On the other hand, as the optical mode is more confined in the silicon waveguide underneath, it will experience lower optical absorption loss since there are no doped layers in the Si device. In addition, the impact of the III-V sidewall scattering loss also decreases.
Figure 4.2(a) depicts the simulated optical mode profile in the middle of the cavity.

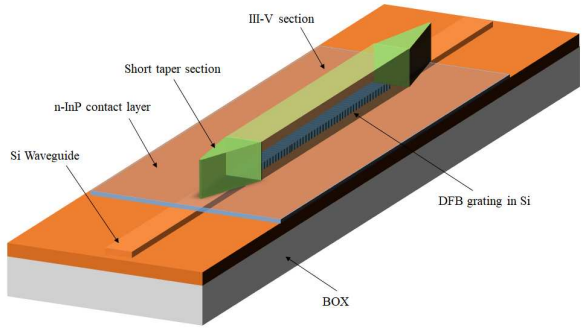

Figure 4.1: Schematic structure of the heterogeneously integrated DFB laser diode on the Si waveguide using a narrow InGaAlAs MQW active region.

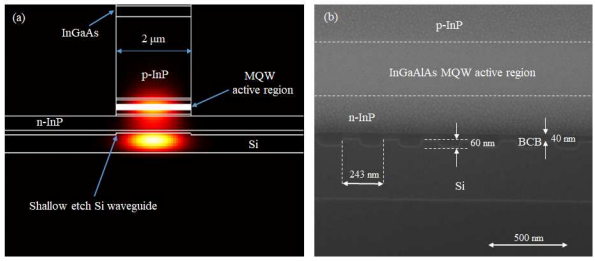

Figure 4.2: Illustration of an III-V-on-si DFB laser with a narrow InGaAlAs MQW active region. a) Optical mode profile in the III-V/Si cross-section. b) FIB longitudinal cross-section of the laser.

The calculated optical confinement is around 3.9 % for a BCB thickness of 40 nm. As represented in Figure 4.2(b), the patterned DFB grating has a etch depth of 60 nm and the BCB thickness is around 40 nm. A quarter-wave shift in the middle of the cavity is incorporated to have a longitudinal mode at the Bragg wavelength λ_B. The DFB grating period Λ is then estimated by:

$$\Lambda = \frac{\lambda_B}{2n_{eff}} \tag{4.1}$$

where λ_B is the Bragg wavelength, and n_{eff} denotes the effective index of the fundamental optical mode in the cavity.

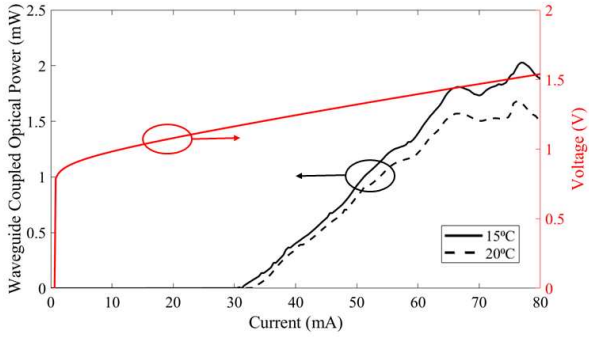

Figure 4.3: Waveguide-coupled optical output power (single-sided) versus DC bias current (left), and I-V curves (right) at two operating temperatures.

The static characterization of the DFB lasers is carried out by placing the fabricated chip on a temperature-controlled stage. The laser is biased with a Keithley 2400 current source and the laser emission is collected through a standard single mode fiber coupled to the on-chip grating coupler structures. The coupling efficiency of the grating couplers is determined by the separate reference structures on the chip. The fiber-to-chip loss is measured to be around 10 dB at the emission wavelength (1555 nm).

Figure 4.3 depicts the L-I curve of a fabricated laser at two operating temperatures. The threshold current is 32 mA at 15 °C and the maximum output power is around 2 mW at a bias current of 77 mA. A differential resistance of 7.5 Ω is achieved for a 200 µm long cavity. The optical spectrum of the laser, lasing at the wavelength of 1555 nm at a bias current of 66 mA, is shown in Figure 4.4. A side mode suppression ratio (SMSR) of larger than 55 dB is achieved and the laser shows a stable operation as a function of bias current.

Although the results obtained from this short cavity laser with a length of 200 µm represent an improvement compared to our previous demonstrations in terms of the device footprint, the high threshold current and relatively low output power are the drawback of these lasers. As we discussed in chapter 3 (section 3.3.3.4), for a narrow active region configuration, the optical mode is in close contact with the sidewall of the active region. This can be an issue due to the large scattering loss of the sidewall roughness, specifically in an Al-containing active region where III-V material can also rapidly oxidize when it is exposed to air. Non-radiative recombination at surface defects can result in a reduction of the carrier lifetime and an increase of the laser threshold. In order to investigate more, we measured

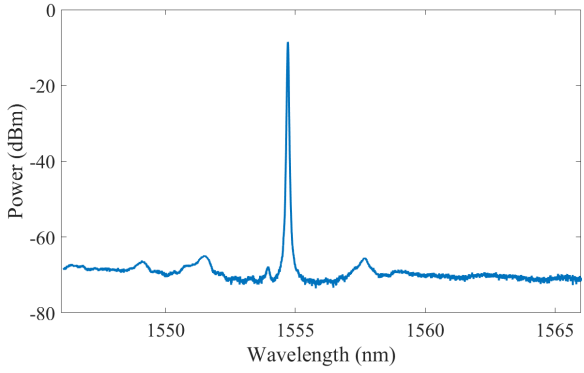

Figure 4.4: Optical spectrum at 20 °C at 66 mA with a SMSR larger than 55 dB.

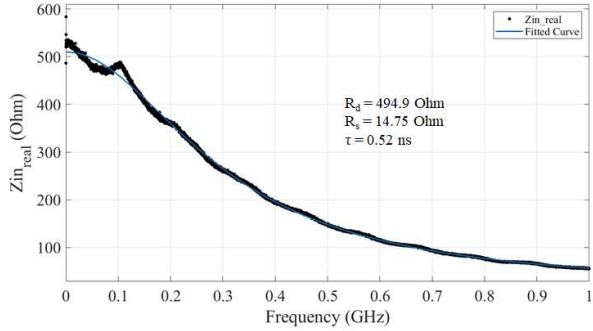

Figure 4.5: The real part of the measured input impedance of the III-V-on-Si DFB laser with a narrow InGaAlAs MQW active region as well as the fitted curve at a bias current of 0.2 mA.

the differential carrier lifetime of the demonstrated device using the technique we discussed in the previous chapter. As shown in Figure 4.5, at a very low bias current (0.2 mA), a differential carrier lifetime of 0.52 ns is achieved. Compared to the measured lifetime of similar devices with an Al-containing MQW active region, given in Figure 3.5, these devices show 3 times smaller carrier lifetime. According to equations (2.31) and (2.36), such a short carrier lifetime results in a high threshold current and low output power. In order to avoid this issue, we choose a wide MQW active region in the next generations of III-V-on-Si DFB lasers as discussed in the following. Unfortunately, due to a lack of InGaAlAs III-V epi stacks, we have not been able to further study the performance of the DFB lasers based on the Al-containig MQW active region. Therefore, the rest of the presented results in this thesis will be based on the InGaAsP MQW epi stack. It should be emphasized that the main objective of this work is independent of the type of the epitaxial structure used in the fabrication.

4.2.2 III-V-on-Si DFB lasers with a wide InGaAsP MQW active region

Figure 4.6 depicts the schematic of a III-V-on-Si DFB laser with a wide MQW active region. The SOI circuit which has been fabricated using the e-beam lithography, consists of a 400 nm thick silicon device layer on a 2 µm BOX layer. The cavity is 200 µm long, determined by a 1 µm wide, first order, quarter-wave shifted grating in the silicon with a 60 nm etch depth. As discussed in chapter 3, the higher

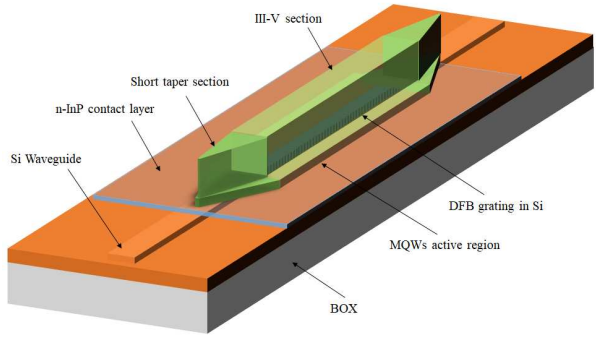

Figure 4.6: Schematic structure of the heterogeneously integrated DFB laser diode on the silicon waveguide.

order mode extends towards the edges of the waveguide. In order to suppress

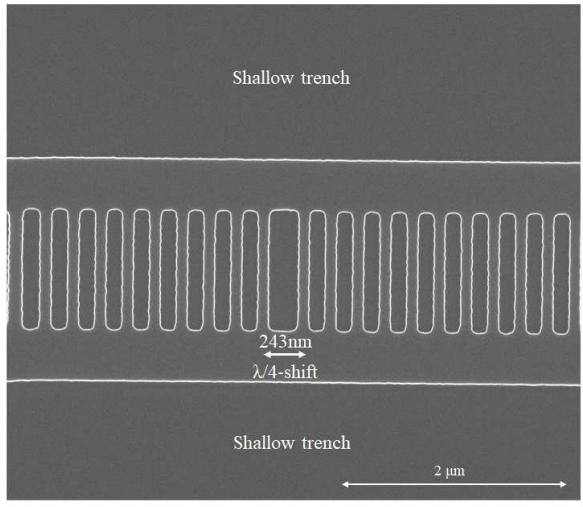

Figure 4.7: SEM image of a first order grating with a λ/4 phase shift.

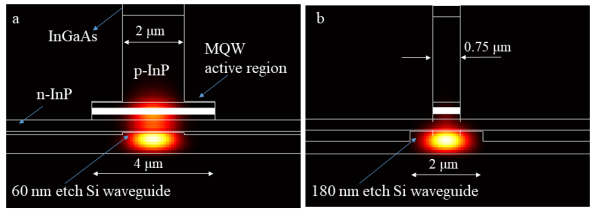

Figure 4.8: Optical mode profile in the III-V/Si cross-section. a) Mode profile in the laser cross-section. b) Mode profile at the III-V taper tip.

the oscillation of higher order transverse modes in the cavity, the DFB grating is patterned only in the center of the silicon waveguide (as shown in Figure 4.7). The alternative approach to have single mode operation is via proton implantation to define a current channel in a wide III-V mesa. Similar to the fabricated device described in the previous section, the 60 nm etched silicon waveguide is connected to a 180 nm etched silicon waveguide in which the grating couplers are incorporated. The laser mesa is 2 µm wide and consists of two short tapers with a length of 10 µm at the ends. The active region of these lasers is made of an InGaAsP MQW stack (6 wells) surrounded by 100 nm thick SCH layers. The details of the InGaAsP epitaxial structure can be found in Table 3.2.

The hybrid optical mode profile is shown in Figure 4.8(a). As can be seen, the optical mode is more confined to the silicon waveguide. The simulated confinement factor in the MQW active region is about 4%. In this structure, we designed the MQW active region to be wider than the III-V mesa in order to reduce the effect of the surface recombination as well as the sidewall scattering loss caused by the

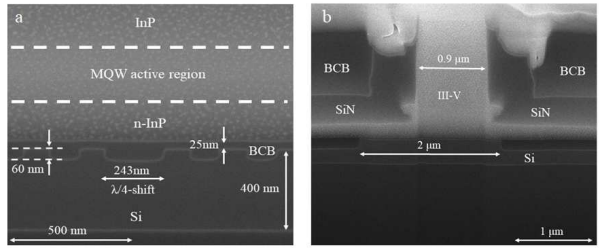

Figure 4.9: FIB cross-section of the fabricated device. a) Longitudinal cross-section of the laser. b) Transversal cross-section close to the taper tip.

etching of the active region. Finally, as Figure 4.8(b) depicts, the optical mode profile at the short taper tip is predominantly in the silicon waveguide. This design enables the efficient coupling of the light from the III-V/Si laser into the silicon waveguide just by incorporating a 10 μm long taper.
Figure 4.9(a) shows the focused ion beam (FIB) longitudinal cross-section image of the fabricated device. The quarter wave shift grating with a grating period of 243 nm is visible beneath the bonded III-V material. The cavity length determined by the 60 nm etch-depth quarter-wave shifted DFB grating section is 200 μm. By optimizing the machine bonding parameters and using a DVS-BCB 3022-35:Mesitylene 1:10 solution the BCB thickness decreases to 25 nm. Figure 4.9(b) depicts the cross-section image of the fabricated device close to the taper section.

4.2.2.1 Static characteristics

The static characterization of the fabricated chip is discussed in this section. The chip is mounted on a stage equipped with a temperature controller and lasers are biased using a Keithley 2400 source meter. The output light is collected through a fiber-to-chip grating coupler with a 10 dB measured coupling loss at the emission wavelength.
DFB lasers with three different lengths have been fabricated on this chip. In Figure 4.10, the L-I curves for the cavity lengths of 100 μm and 150 μm are depicted. Figure 4.10(a) shows the L-I curve of a 100 μm long cavity with the κL value of around 3. Although the DFB laser starts lasing at 14 mA, the output power suddenly clamps and a linear L-I curve is not achieved. We believe the heating in such a short cavity laser is detrimental. As shown in Figure 4.10(b), the 150 μm long cavity DFB laser shows a better performance. The threshold current is around 13 mA and the laser shows a linear L-I characteristics up to 50 mA. However, due to the self heating of the device, a roll-off in the L-I curve is observed at higher bias currents. The L-I curve of the 200 μm long DFB laser is measured at different stage temperatures and the results are depicted in 4.11. The measured threshold current at 20 °C is 10.5 mA and it increases up to 14.5 mA by increasing the operating temperature to 40 °C. A waveguide-coupled optical power up to 6.5 mW is obtained from a single facet. Due to the symmetrical configuration, the same results are obtained from the other output of the laser. In addition, the measured I-V curve in Figure 4.11 shows that the voltage remains below 2 V. As can be seen, there are ripples or kinks in the L-I curves due to the reflections from the grating coupler. The phase of these reflections changes with the current due to the heating of the device.
Figure 4.12 illustrates the optical spectrum for various bias currents at 20 °C. The laser operates at 1560 nm at a bias current of 20 mA and shifts to 1561 nm and 1563 nm as the current increases to 40 mA and 70 mA, respectively. Stable optical

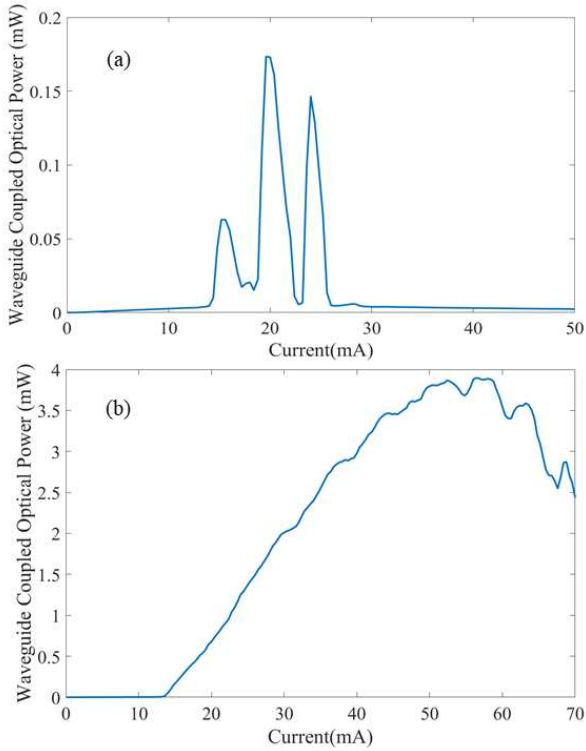

Figure 4.10: Waveguide-coupled optical output power (single-sided) versus DC bias current at 20 °C. a) A 100 μm long DFB laser, b) A 150 μm long DFB laser.

lines with no hopping in the lasing wavelength are observed at 40 mA and 70 mA which are close to the kinks in the L-I curve. A SMSR of about 44 dB is obtained at 70 mA bias current. Assuming a thermal dependence of the effective index of 2×10^{-4}/K, the shift of the laser wavelength with the increased current corresponds with a heating by 30 K when the current is increased from 20 to 70 mA.
The wall-plug efficiency of the laser as a function of the bias current at different operating temperatures is shown in Figure 4.13. As can be seen, more than 12% wall-plug efficiency is achievable at room temperature. For a better understanding

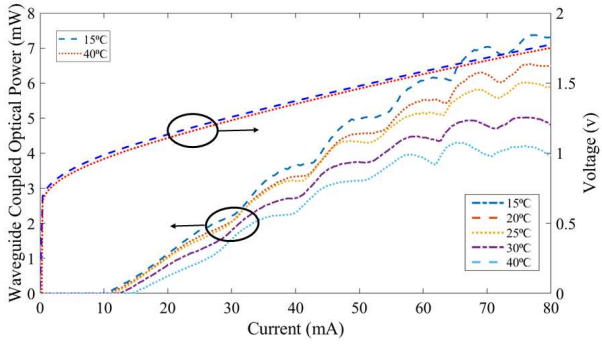

Figure 4.11: Waveguide-coupled optical output power (single-sided) versus DC bias current (left), and I-V curves (right) at various operating temperatures.

of the device performance, we give in Figure 4.13(b) the wall-plug efficiency versus total optical output power collected from both output facets. In semi-cooled operation (40 °C), up to 9% wall-plug efficiency is measured.

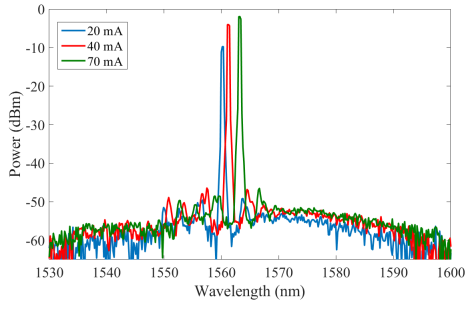

Figure 4.12: Optical spectrum at 20 °C at various bias currents. 3 nm redshift in the lasing mode is observed by increasing the bias current from 20 mA to 70 mA and the corresponding SMSR improves from 39 dB to 44 dB.

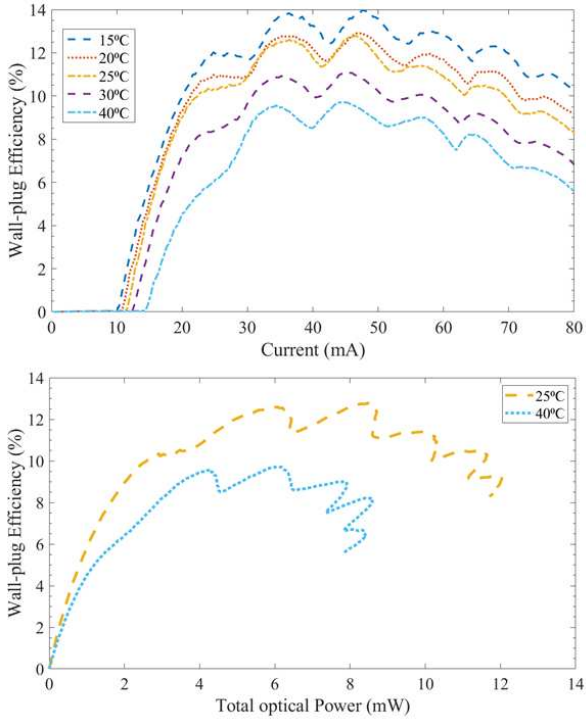

Figure 4.13: Wall- plug efficiency illustration for the 200 µm long cavity DFB laser on SOI. a) Wall-plug efficiency versus bias current at various operating temperatures. b) wall-plug efficiency as a function of total output power at 25 °C and semi-cooled operation (40 °C).

4.2.2.2 Dynamic characteristics

Small-signal measurements were carried out using an Agilent N5247A vector network analyzer (VNA) to provide radio frequency (RF) electrical signals. Using a bias tee, the RF signal is combined with a DC bias current to modulate the laser by means of a Cascade Infinity GSG RF probe with 100 µm pitch. Then, the laser light is sent to a Discovery DSC-10H photodetector (PD) with a bandwidth of 43 GHz and the output electrical signal is sent back to the VNA to measure the small signal S parameters. Figure 4.14 depicts the small signal S_{21} parameter, measured at room

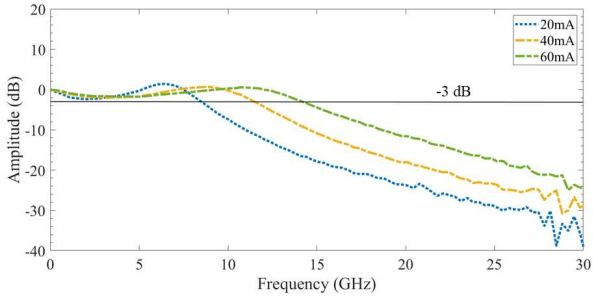

Figure 4.14: Small signal modulation characteristics at various bias currents.

temperature at various bias currents. At a bias current of 60 mA the modulation bandwidth of the device is found to be around 15 GHz. The main limiting factor of the modulation bandwidth in our design (and similar ones) is the confinement factor of the optical mode in the MQW active region. As we mentioned earlier, the optical mode in this design is mostly confined in the silicon waveguide. This can be beneficial in decreasing optical loss and increasing the internal efficiency, whereas the consequence is the degradation of the modulation bandwidth.

The large signal intensity modulation of the laser is investigated by performing a data transmission experiment. Figure 4.15 describes the block diagram of the setup used for this measurement. The modulation signal is generated using a Keysight M8196A arbitrary waveform generator (AWG). An SHF807 RF amplifier is used to amplify the output signal of the AWG. Then, the amplified modulation signal is combined with a DC current via a bias tee and the corresponding output signal

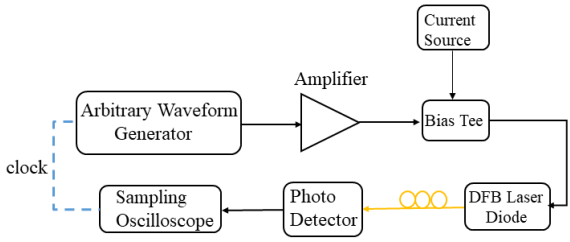

Figure 4.15: Block diagram of the experimental setup for the data transmission.

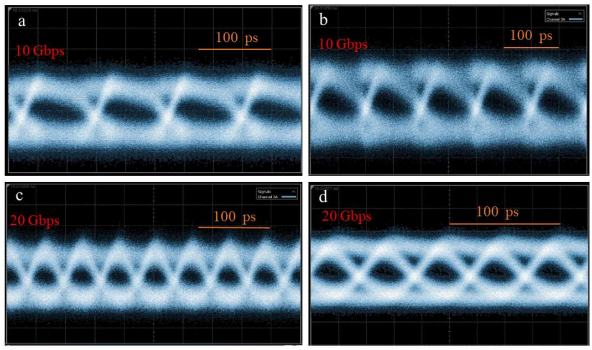

Figure 4.16: Data transmission experiment; (a) and (c) eye diagram for the back to back configuration at 10 Gb/s and 20 Gb/s, respectively. (b) and (d) eye diagram after transmission over a 2 km fiber at 10 Gb/s and 20 Gb/s, respectively.

drives the laser by using the GSG RF probe. The laser optical output signal is directly sent to the photodetector, of which the output is fed to a Keysight 70 GHz sampling oscilloscope without using any RF amplifiers. The large signal characterization results are illustrated as eye diagrams in Figure 4.16. Non-return-to-zero (NRZ) data transmission with a Pseudo-Random-Binary-Sequence (PRBS) pattern length of 2^7-1 is verified. Open eyes can be observed at 10 Gb/s and 20 Gb/s after transmission over a 2 km long non-zero dispersion-shifted-fiber (NZ-DSF). A 4 dB extinction ratio is obtained at 20 Gb/s. These results are achieved at a bias current of 70 mA without using any optical or electrical amplifiers at the receiver, nor equalization.

4.3 III-V-on-Si DFB lasers with a wide InGaAsP MQW active region and a single output waveguide

Figure 4.17 depicts the schematic of the reported devices in this particular run. A 400 nm thick silicon device layer on top of a 2 µm buried oxide layer is used. The cavity, determined by a first order, quarter-wave-shifted grating is 180 µm long. The DFB grating, with a period of 243 nm, is patterned into the SOI using a Voyager electron beam lithography (EBL) system. Figure 4.18 (a) shows the dependence of the fundamental optical mode confinement factor in the MQW active region on the width of the III-V mesa and the silicon waveguide. Decreasing the width of the III-V

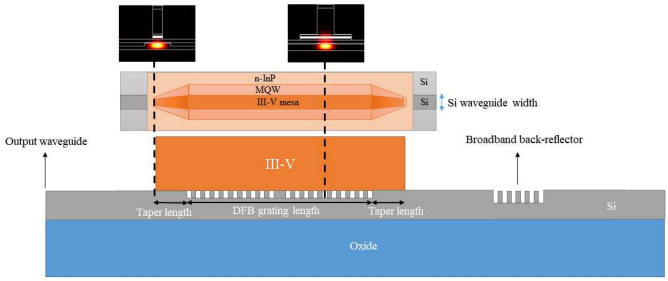

Figure 4.17: The schematic of a fabricated heterogeneously integrated III-V-on-Si C-band DFB laser.

mesa can be useful in pushing the mode down into the silicon leading to a lower internal loss. However, it can also be detrimental for the device series resistance, specifically for short cavity lasers, as well as for the provision of sufficient gain for lasing. While a wider silicon waveguide can be also advantageous in pushing down the optical mode into the silicon waveguide and decreasing the internal loss of the cavity, it can result in excitation of higher order modes and affect the laser performance.

Designing a narrow III-V mesa and silicon waveguide together with a narrower DFB grating in the middle of the silicon waveguide can be beneficial in suppressing the excitation of the higher order mode which extends towards the edges of the waveguide. The width of the grating is chosen to be 1 μm and that of the III-V mesa and the silicon waveguide is chosen to be 2 μm. The 6 μm wide active region consists of six QW layers each 6 nm thick, separated by 10 nm barriers in between. Figures 4.18(b-d) illustrate the effect of the DFB grating etch depth on the confinement factor in the MQW active region, the internal loss of the cavity , and the grating coupling coefficient (κ). In this design the DFB grating and the silicon waveguide are defined with a 40 nm etch. This shallow etch configuration together with a thin (20 nm) layer of BCB allow the optical mode to be predominantly confined to the silicon, which not only facilitates the light coupling from the III-V to the silicon waveguide underneath but is also beneficial in decreasing the internal loss since the III-V cladding layers are highly absorbing.

A 14 μm long linear taper is incorporated to get over 95% of coupling. Then the shallow etched part of the structure is connected to a 180 nm etched, 2 μm wide silicon rib waveguide. In order to increase the single facet output power, a broadband reflector is incorporated in the silicon waveguide at one side of the cavity. The grating period of this external DBR is 252 nm, patterned by 180 nm

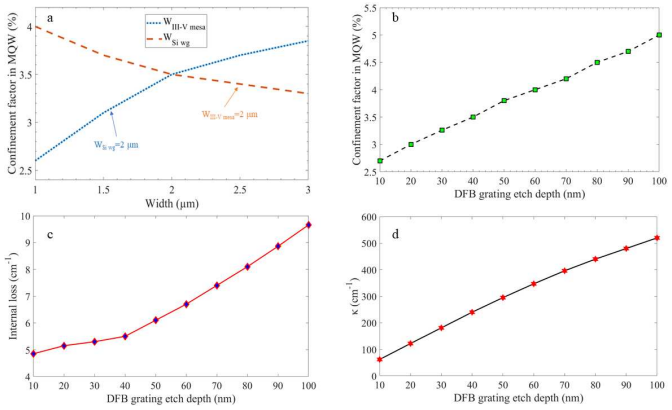

Figure 4.18: Simulation results for the confinement factor in MQW, the internal loss , and the grating coupling coefficient. a) Confinement factor in the MQW active region versus the width of the III-V meas and the silicon waveguide, b) Confinement factor in the MQW active region versus the DFB grating etch depth, c) Internal loss versus the DFB grating etch depth, and d) DFB grating coupling coefficient κ versus the DFB grating etch depth.

surface etched grating. In Figure 4.17, the optical mode profiles in the middle of the cavity and at the taper tip are shown. As reported in Figure 4.18(b), the simulated confinement factor in the MQW active region, consisting of InGaAsP MQW layers, is 3.5%. These devices are realized using adhesive bonding in which the III-V epitaxial layer is bonded onto the pre-patterned SOI. The full description of the fabrication steps can be found in chapter 3.

4.3.1 Static characteristics

In order to perform the static characterization, the chip is mounted on a stage equipped with a temperature controller and is biased with a Keithley 2400 source meter. Figure 4.19 shows the single facet output optical power as a function of the injection current for four identical lasers. The maximum on-chip power (up to 12 mW) is obtained from laser No 4, while laser No 1 has the lowest threshold current (11 mA). Figure 4.19 also indicates that the fabrication process is reproducible. The output light is collected through a fiber-to-chip grating coupler with a 9 dB measured coupling loss. The DFB laser described in the previous section had a symmetric configuration with equal output power from both facets. However, here the laser just has one output facet due to an HR facet at one side of the cavity. In

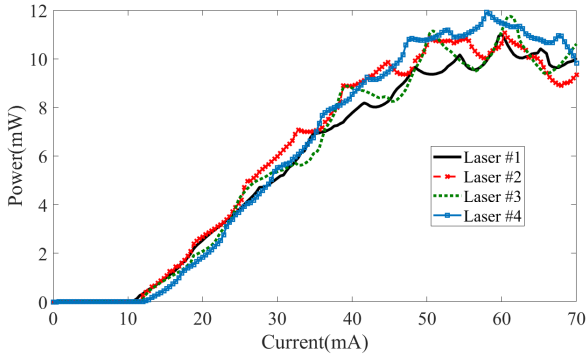

Figure 4.19: Waveguide coupled optical output power as a function of bias current for four identical lasers on the chip at 20 °C.

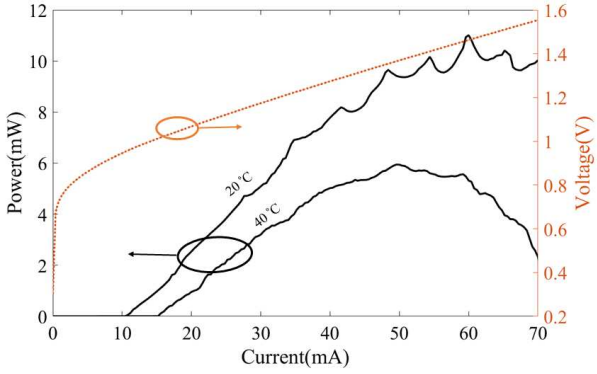

Figure 4.20: Waveguide coupled optical output power as a function of bias current. The I-V curve is measured at 20 °C.

the following, we select laser No.1 to further investigate the characterization of the device. In order to study the laser performance at the semi-cooled operation regime, we present Figure 4.20 in which the I-V curve of the device is also depicted. As mentioned, at 20 °C the laser has a threshold current of 11 mA and an output power of up to 11 mW is coupled to the silicon waveguide. By increasing the stage temperature to 40 °C, the threshold current increases to 15 mA. The measured

series resistance is about 9 Ω for the 180 µm long cavity. As can be derived from Figure 4.21, the lasing wavelength is 1567 nm and the SMSR is around 55 dB at a bias current of 60 mA at 20 °C.
The DFB grating coupling coefficient κ can be extracted from the full stopband visible in the laser spectrum shown in Figure 4.21, using equation (2.23) as follows:

$$\Delta\lambda = \frac{\lambda_B^2}{2\pi n_{eff} L_o}\sqrt{(\kappa L_o)^2 + 4\pi^2} \tag{4.2}$$

where $\Delta\lambda$ is the half width of the full stopband, λ_B denotes the Bragg wavelength, n_{eff} represents the effective index of the lasing mode, and L_o is the effective or optical length of the cavity. Since there is an HR facet at one side of the DFB cavity the L_o is equal to $2L$ where L is the DFB grating length (cavity length) equal to 180 µm in this work. By inserting $\Delta\lambda$= 3.5 nm from the spectrum, a κ value of 233 cm^{-1} is obtained, which is in good agreement with the simulated value of around 240 cm^{-1} reported in Figure 4.18(d). We choose an etch depth of 40 nm as this combines small internal loss and high κL.
In order to investigate the performance of the device in terms of wall-plug efficiency, an intuitive analysis based on experimental results is useful. In Figure 4.20, by considering the slope efficiency at 20 mA at 20 °C, the ratio of the internal loss α_{int} to the mirror loss α_m is found to be 2.2, assuming a 100 % injection efficiency. The simulated internal loss for a DFB grating etch depth of 40 nm is around 5.4 cm^{-1} (Figure 4.18 (c)) from which a mirror loss of 2.45 cm^{-1} can be estimated for this cavity. The DFB laser with one non-reflecting and one 100% reflecting facet

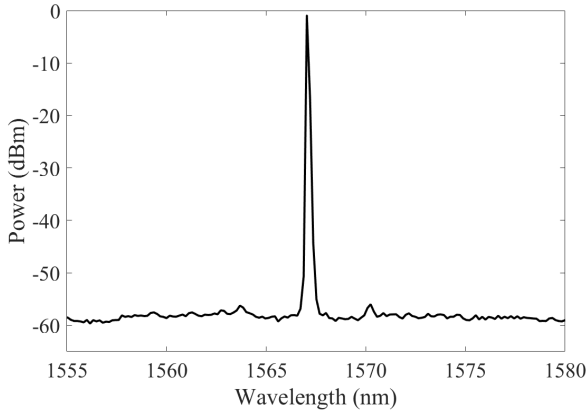

Figure 4.21: The optical spectrum at a bias current of 60 mA at 20 °C.

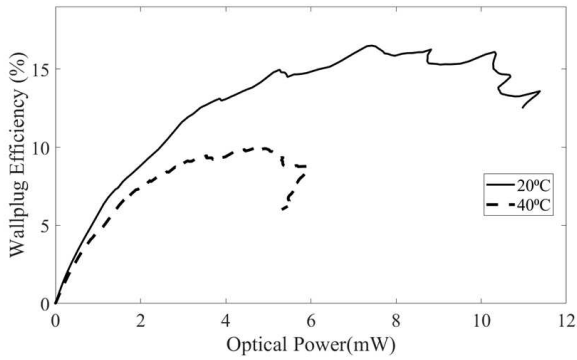

Figure 4.22: Illustration of the measured wall-plug efficiency versus the injected current.

can be considered as a folded version of a twice as long DFB laser with both facets AR-coated. The equivalent phase shift is then determined by the phase shift of the 100% reflection. However, due to the $\lambda/4$-phase shift in the middle of the grating, our DFB laser is basically a folded version of twice as long laser with $\lambda/4$ phase shifts at L/4 and 3L/4 and an unknown phase shift in the middle. Nevertheless, from equations (2.19) and (2.24), we can estimate that the mirror loss will be somewhere between that of a $\lambda/4$-shifted and a non-phase-shifted DFB laser with both facets being AR-coated. Using the κL value of 8.4 (233 cm^{-1} x 0.018 cm $\times$ 2), we find that the mirror loss will be between 0.21 and 7.7 cm^{-1}. However, in the optical spectrum it can be seen that the emission line is not exactly in the middle of the stopband but still very close to it. In order words, it behaves very much as a phase shifted DFB laser with a phase shift very close to $\lambda/4$, and thus the mirror loss will probably be much lower than 7.7 cm^{-1}. This agrees with the mirror loss of 2.45 cm^{-1} estimated from the efficiency. In order to improve the efficiency, the mirror loss can be increased to a value close to the internal loss. This can be achieved by the decreasing the etch depth of the grating or using a narrower grating.

Figure 4.22 gives the wall-plug efficiency versus the injected current for two operating temperatures. In our previous work, the wall-plug efficiency is plotted by adding the output power from both facets. Here, more than 16% wall-plug efficiency is achieved at 20 °C for bias currents below 40 mA which shows an improvement of 4 % compared to the previous work. It also shows the laser performance in a semi-cooled operation regime with a wall-plug efficiency up to 10%.

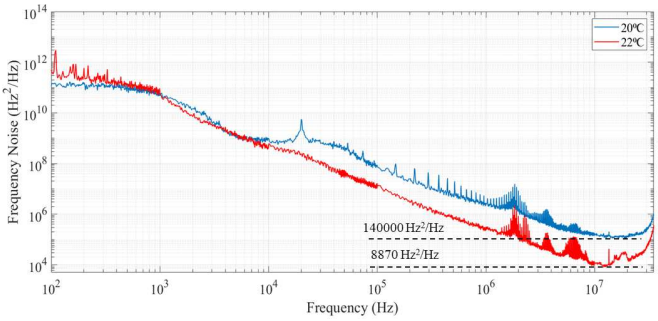

Figure 4.23: The spectral density of the frequency noise versus frequency of the heterogeneously integrated DFB laser. The Lorenzian linewidth is calculated by multiplying the white noise level (the flat part of the spectra) by π.

4.3.2 Noise characteristics

In order to investigate the noise characteristics of these short cavity lasers, we measured the spectral densities of the frequency and relative intensity noise of the laser. The spectrum of the frequency noise of the laser was measured using a OE4000 phase and frequency noise test system without using an optical isolator, while the RIN was measured with an electrical spectrum analyzer. Figure 4.23 depicts the frequency noise spectra at a bias current of 60 mA. The power spectral density (PSD) of the Gaussian white noise is found to be 140×10^3 Hz^2/Hz at 20 °C. An intrinsic (Lorentzian) linewidth of 440 kHz has been calculated by multiplying

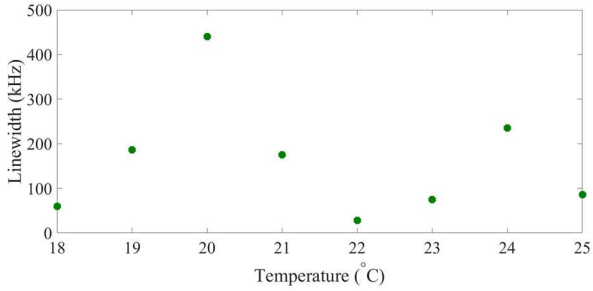

Figure 4.24: The measured intrinsic linewidth versus temperature.

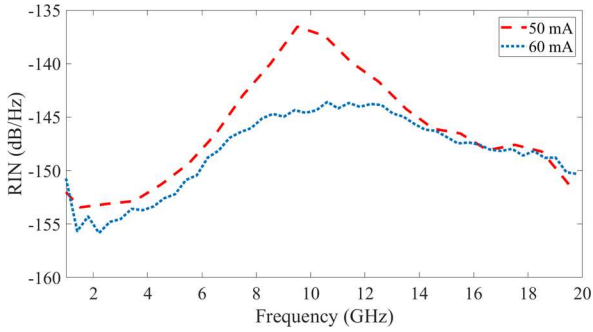

Figure 4.25: RIN measured from the reported III-V-on-Si DFB laser at bias currents of 50 mA and 60 mA at 20 °C.

the white noise PSD value by π. Besides the low loss silicon platform, this reduction in the solitary laser linewidth can also be attributed to the weak feedback effect of the external cavity formed by the grating coupler. In our design, the output grating coupler is placed at the distance of 1350 µm from the nearest laser facet and the broadband reflector is approximately 90 µm away from the other facet which constitutes a compound cavity with the total length of 1620 µm. The variation of the linewidth with the phase of the external reflection has been described in chapter 2 and equation (2.77). We changed this phase by changing the temperature of the stage. The measured intrinsic linewidth versus the temperature is shown in Figure 4.24. This causes sufficient changes in lasing wavelength to change the phase of the reflection over 2π. We found that tuning the operating temperature can lead to a significant decrease in the laser linewidth. The measured frequency noise spectrum at 22 °C plotted in Figure 4.23 shows a white noise PSD of 8870 Hz^2/Hz which corresponds to an intrinsic linewidth of 28 kHz.

The RIN is measured at 20 °C by connecting the fiber coupled optical output of the laser to a high speed DSC-R409 Lab Buddy optical receiver. Then the output electrical signal from the receiver is sent to a low noise SHF S804B amplifier to overcome the limited noise floor of the electrical spectrum analyzer. The noise measurement is performed up to 20 GHz, once after switching the laser off to measure the total thermal noise of the system and then after turning it on to measure the total noise including the contribution from the intensity noise of the laser. The laser RIN is then calculated by subtracting the thermal noise from the total measured noise. The shot noise of the receiver is found to be around -177 dB/Hz which is not a limiting factor in this measurement. In Figure 4.25, the measured RIN at bias currents of 50 mA and 60 mA are depicted. The laser RIN is below -150 dB/Hz up

to 6 GHz.

4.3.3 Dynamic characteristics

In order to investigate the dynamic behavior of the device, a set of small signal modulation and large signal data transmission experiments have been carried out. For the small signal modulation experiment, the laser is biased using an Agilent N5247A vector network analyzer (VNA) to provide radio frequency (RF) electrical signals. The optical signal of the laser is captured by a Discovery DSC-10H photodetector (PD) and the corresponding output electrical signal is connected to the VNA to measure the small signal S parameters. Figure 4.26(a) shows the small signal behavior of the laser at 20 °C and 40 °C with a modulation bandwidth of about 14 GHz and 9 GHz at 50 mA, respectively. The data transmission experiment is performed by using a Keysight M8196A arbitrary waveform generator (AWG). The modulated output of the laser is directly connected to a high-speed PD without using any optical or electrical amplifier nor equalization. Figures 4.26(b,c) show the eye diagrams for NRZ data transmission with a Pseudo-Random-Binary-Sequence (PRBS) pattern length of 2^9-1 at 20 Gbps and 10 Gbps at 20 °C and 40 °C,

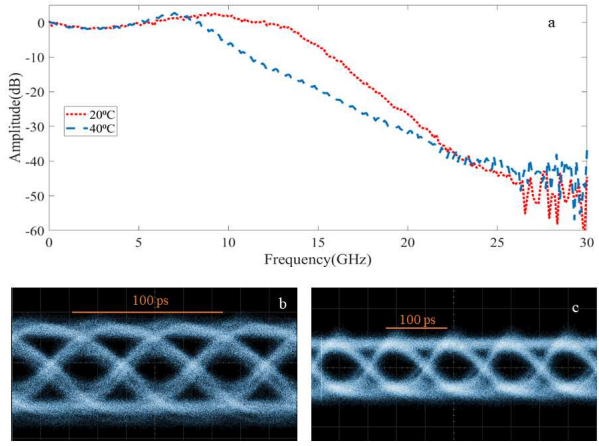

Figure 4.26: Dynamic characterization of the device. a) small signal response at 20 °C and 40 °C, b) eye diagram for the 20 Gbps back to back data transmission at 20 °C, and c) eye diagram for the 10 Gbps back to back data transmission at 40 °C.

respectively.

4.4 Conclusion

In this chapter, we demonstrated compact and high-efficiency integrated DFB lasers realized by adhesive bonding. By using a shallow etched grating in the DFB cavity, the optical mode is predominantly confined to the silicon underneath. This is beneficial in decreasing the laser threshold current and increasing the slope efficiency.

We successfully demonstrated a high wall-plug efficiency and low threshold current for heterogeneously integrated III-V-on-Silicon distributed feedback (DFB) lasers. Above 12% wall plug efficiency is achieved for a 200 μm long DFB laser diode at 25 °C. Due to the symmetrical configuration, up to two times 6 mW of optical power is coupled into the silicon waveguide and more than 40 dB side-mode suppression ratio is obtained. We also discussed the non-return-to-zero on-off keying modulation at 20 Gb/s and the transmission over a 2km long optical fiber.

Based on the experimental results achieved in the first fabrications, we further optimized the III-V-on-Si DFB lasers. To increase the single facet output power, a deeply etched broadband reflector is incorporated in the silicon waveguide at one side of the cavity. In addition, we chose a DFB grating etch depth of 40 nm as this combines small internal loss and high κL. Our measurement results show wall-plug efficiencies up to 16.5% and 10% at temperatures of 20 °C and 40 °C, respectively. For further investigation of the device performance, the frequency and intensity noise of the laser have been measured. A very low frequency noise is obtained by taking advantage of a low loss short external cavity formed by the weak feedback from the grating coupler. It is shown that by a 2 °C increase in the temperature the Lorentzian linewidth can be decreased more than an order of magnitude to a value as low as 28 kHz. In addition, the RIN is measured below -150 dB/Hz up to 6 GHz. Dynamic characterization of the laser has also been carried out and 20 and 10 Gbps directly modulated data transmission have been reported at a bias current of 50 mA at 20 °C and 40 °C, respectively.

Further improvement could still be expected by optimizing the etching of the InP mesa to reduce scattering loss or by increasing the mirror loss by reducing the DFB grating coupling coefficient κ. Using a narrower active layer would improve the confinement factor over volume ratio and thus also the modulation bandwidth. The narrower active layer will most likely also reduce the leakage current and thus result in lower threshold current and still higher efficiency. A comparison of the demonstrated III-V-on-silicon C-band DFB lasers is presented in Table 4.1.

Group	Cavity length (μm)	Threshold Current (mA)	Maximum W.P.E (%)	Maximum on-chip output power (mW)	Slope Efficiency (WA^{-1})	SMSR (dB)	Direct Modulation speed (Gbit/s)
Ghent University-IMEC	680	35	9	14	0.135	50	–
UCSB	200	8.8	>3	>7	≈ 0.1	>55	12.5 @ 62 mA
UCSB	400	7.5	≈ 3	>5	≈ 0.06	>55	–
Ghent University-IMEC	340	32	≈ 3.3	>7	0.072	45	56 @ 110 mA
III-V Lab	600	35	–	–	0.12	>50	32 @ 100 mA
This work	180	11	>16	>11	0.38	>55	20 @ 50 mA

Table 4.1: Static and dynamic characteristics of III-V-on-SOI C-band DFB lasers.

5

Conclusions and outlook

5.1 Conclusions

Integration of photonics and electronics is a prerequisite for the future high-tech products in datacom transceivers, autonomous vehicles, quantum computers etc. Silicon photonics is often preferred as it allows the integration of a large number of optical components on a silicon-on-insulator (SOI) platform. This results in a shrinkage of the footprint of photonic systems as well as in a reduction of the power consumption and cost. Using mature CMOS fabrication processes, high-performance passive components such as optical waveguides and couplers, high-performance silicon optical modulators based on the plasma dispersion effect, and ultrafast germanium photodiodes have been realized on SOI. However, the absence of low cost and efficient integrated light sources remains an obstacle for the development of this technology. This issue leads to the need for integrating III-V materials onto SOI to realize efficient light sources.

In this thesis, a heterogeneous integration technique based on adhesive bonding is used to demonstrate high-efficiency short-cavity III-V-on-Si C-band DFB laser diodes. In the context of datacom, a high wall-plug efficiency is critical since it normally leads to a low electrical power consumption for the optical transmitter and requires typically also less power consuming cooling. This is especially important where many transmitters are present in a limited area (e.g., in datacenters). In

addition, small footprint integrated transmitters are needed to decrease the final package size and cost of the transceivers.

In order to design a short cavity III-V-on-Si DFB laser, the optical mode inside the cavity has to be engineered. Compared to the silicon waveguide, the III-V mesa is highly absorbing due to the intervalence band absorption. Thus, pushing down the hybrid mode into the silicon waveguide can result in a reduction of the internal loss and an increase in internal efficiency. However, the lower optical confinement in the active region can increase the threshold current and degrade the modulation bandwidth. Considering this trade-off, we designed integrated DFB lasers by using a shallow etched grating in the DFB cavity. Due to the shallow etched DFB grating, the optical mode is predominantly confined to the silicon and it is shown how this configuration relaxes the requirement of long taper structures in the earlier demonstrated lasers.

We successfully demonstrated high wall-plug efficiency and low threshold current short cavity III-V-on-Si DFB lasers. Experimental results on integrated DFB lasers with two output waveguides show above 12% wall-plug efficiency at 25 °C. These 200 µm long DFB laser diodes couple up to two times 6 mW of optical power into the silicon waveguide. The static characteristics of the device exhibit a single mode operation with a SMSR up to 44 dB. In addition, the dynamic response is described by measuring the small signal modulation response followed by a data transmission experiment at 20 Gb/s over a 2 km long, single mode fiber.

In order to further optimize the short cavity III-V-on-Si DFB lasers, a configuration with one non-reflecting and one 100% reflecting facet is proposed by designing a deeply etched broadband reflector in the silicon waveguide at one side of the cavity. The DFB grating etch depth is 40 nm which results in a small internal loss and high κL. The static characterization of the fabricated devices show wall-plug efficiencies up to 16.5% and 10% at temperatures of 20 °C and 40 °C, respectively. These devices have been investigated further by performing frequency and intensity noise characterization. Based on the experimental results, a very low frequency noise is obtained by taking advantage of a low loss short external cavity formed by the weak feedback from the grating coupler. It is shown that by a 2 °C increase in the temperature, the Lorentzian linewidth of a solitary III-V-on-Si laser can be decreased more than an order of magnitude to a value as low as 28 kHz. The intensity noise characterization exhibits a RIN level below -150 dB/Hz up to 6 GHz. Dynamic characterization of lasers has also been carried out and 20 and 10 Gbps directly modulated data transmission have been reported at a bias current of 50 mA at 20 °C and 40 °C, respectively.

According to the experimental results achieved in this thesis, the demonstrated III-V-on-silicon short cavity DFB lasers can be a good candidate for datacom applications in a cooled and semi-cooled operation. The narrow linewidth performance may be interesting in future optical interconnects based on coherent communication.

Regarding the data communication applications, these devices can be still applicable specifically when direct modulation is desirable (as was shown in this work). However, for the external modulation technique, the potential applications of these devices depend on the loss of the optical link and preferably DFB lasers with higher output power (more than 10 mW) are required. The narrow linewidth demonstration was originally not a goal, but it was realized during characterization that the fabricated lasers could also give narrow linewidths. This is an advantage of the demonstrated lasers compared to the commercial monolithic InP lasers, which are not so easily integrated with an external cavity.

5.2 Outlook

In this thesis, we have presented a heterogeneous platform for integrating high-efficiency short-cavity III-V-on-Si C-band DFB laser diodes. Nevertheless, substantial effort has to be devoted in two directions in the future. First, by further optimization of the design and fabrication process flow, integrated DFB lasers with wall-plug efficiencies comparable to a commercial level are achievable. Second, the same design concept can also be applied to exploit the potential of micro-transfer printing in wafer level array printing of high performance lasers with multi-post stamps.

5.2.1 Design and fabrication improvements

As we mentioned earlier, the wall-plug efficiency of the III-V-on-Si C-band DFB lasers can be improved further by optimizing the mirror loss of the cavity. According to equations (2.36) and (2.69), the optimum wall-plug efficiency occurs when the mirror loss is close to the internal loss of the cavity. In this work, the internal loss of the cavity is decreased by pushing down the optical mode into the silicon waveguide, which has a lower loss compared to the highly absorbing III-V mesa. In our most recent demonstration, we described a DFB laser with a high κL due to one 100% reflecting facet. This resulted in a mirror loss smaller than the internal loss of the cavity. In order to increase the mirror loss to a value close to the internal loss of the cavity, a shallower etch depth or narrower DFB grating can be beneficial. We also observed that in spite of having a large κL, the threshold current of DFB lasers did not decrease compared to the similar devices fabricated with smaller κL. In order to address this issue the width of the active region has to be designed properly so that on one hand the scattering loss for the optical mode is minimized, and on the other hand the leakage current is reduced.
Further improvement could still be expected by optimizing the etching of the InP

mesa to reduce scattering loss. Special effort has to be devoted to improve the dry etching process by making selective etching recipes for different III-V layers. In this work, the III-V mesa has been patterned by ICP dry etching. However, for patterning of the active region we use ICP dry etching followed by a proper wet etching process. By replacing the wet etching process with a potential dry etching process, the sidewall roughness could be improved specifically at the taper section where the active region gets narrower.

5.2.2 Reliability test

Semiconductor lasers can generally be expected to reach long lifetimes, often tens of thousands of operation hours. In order to reach such high reliability, many tests are required under various circumstances. The next step in improving the quality of the heterogeneously integrated III-v-on-Si DFB lasers is to perform the reliability test on the devices demonstrated in this work. To this end, we prepared some samples with grating couplers (by dicing the chip with arrays of lasers) and some others with edge coupling (by cleaving the chip with array of lasers). Investigating a wide range of performance aspects will be beneficial for the further improvement of the reported devices.

5.2.3 O-band epitaxial structure for high temperature performance

The same design concept can be applied to O-band lasers to serve the datacom market. The O-band laser diodes are known to have a better performance at a high temperature due to the relatively lower Auger recombination mechanism. To this end, we designed an O-band epitaxial structure with the composition given in table 5.1. A 20 nm thick electron blocking layer (EBL) is grown above the MQW region (below the p-type SCH layers) to make a potential barrier for the electrons injected into the MQW region, which results in a better performance specifically at higher operation temperatures. The QW layers have been designed with a compressive strain of 1% while the barrier layers have tensile strain of around 0.1%. There have been some efforts in this PhD research to develop heterogeneously integrated O-band lasers realized by micro-transfer-printing. Figure 5.1 shows a microscope image of SOA coupons at the n-contact metallization step. These coupons are designed for the the next generation of high performance III-V-on-Si O-band lasers. The short structures contain potential coupons for the demonstration of short cavity (< 300 μm) DFB lasers. In addition, longer structures have been also deigned for the purpose of integration on full platform.

Layer	Layer type	Material	Thickness (nm)	Refractive index
1	cap Layer	InP	100	
2	Contact P	$In_{0.53}Ga_{0.47}As$	100	3.4348
3	Contact P	$In_{0.53}Ga_{0.47}As$	100	3.4348
4	Cladding P	InP	1000	3.2034
5	Cladding P	InP	500	3.2034
6	p-SCH 1	$Al_{0.421}Ga_{0.054}In_{0.525}As$ (λ_g=0.9 µm)	50	3.2577
7	p-SCH 2	$Al_{0.3466}Ga_{0.1272}In_{0.5262}As$ (λ_g=1 µm)	70	3.3169
8	EBL	$Al_{0.48}In_{0.52}As$	20	3.2311
9×8	Barrier	$Al_{0.3397}Ga_{0.1484}In_{0.5119}As$ (λ_g=1 µm)	10	3.3169
10×7	Well	$Al_{0.2043}Ga_{0.1208}In_{0.6749}As$ (λ_g=1.4 µm)	6	3.5815
24	n-SCH 1	$Al_{0.3466}Ga_{0.1272}In_{0.5262}As$ (λ_g=1 µm)	70	3.3169
25	n-SCH 2	$Al_{0.421}Ga_{0.054}In_{0.525}As$ (λ_g=0.9 µm)	50	3.2577
26	Cladding N	InP	200	3.2034
27	sacrificial	$In_{0.53}Ga_{0.47}As$	50	
28	sacrificial	$In_{0.53}Ga_{0.47}As$	500	
29	Buffer Layer	InP	150	
	Substrate	InP		

Table 5.1: Description of the InGaAlAs O-band epitaxial structure.

5.2.4 Small foot-print transfer printed DFB lasers

The design concept introduced in this work can be a reliable solution for the lateral misalignment issue in micro-transfer-printing. Since the optical mode is

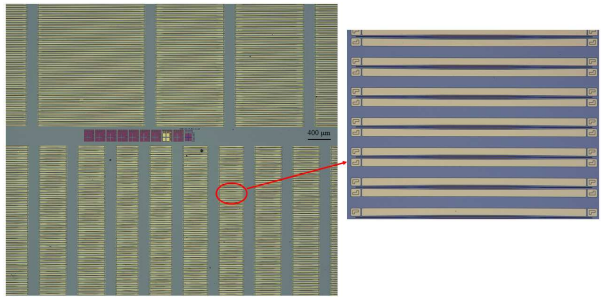

Figure 5.1: Fabrication of the O-band coupons for the next generation of high performance and short cavity integrated DFB lasers. The microscope images shows the fabrication process after the n-contact metallizaion, which the laser mesa and transfer printing alignment markers are visible in the inset.

strongly confined to the silicon waveguide, the light coupling mechanism from the III-V waveguide layer to the silicon waveguide layer is less sensitive to the lateral misalignment. In addition, the micro-transfer-printing technique makes more efficient use of the costly III-V material compared to the machine bonding used in this thesis. It also provides the possibility of wafer level array printing with multi-post stamps.